A textural and mineralogical study of the footwall rocks to the Sudbury Igneous Complex (North and East ranges)

by

Jeffrey Michael Enright

A thesis submitted in partial fulfillment of the requirements for the degree of

Master of Sciences (MSc) in Geology

The Faculty of Graduate Studies

Laurentian University

Sudbury, Ontario, Canada

THESIS DEFENCE COMMITTEE/COMITÉ DE SOUTENANCE DE THÈSE
Laurentian Université/Université Laurentienne
Faculty of Graduate Studies/Faculté des études supérieures

Title of Thesis Titre de la thèse	A textural and mineralogical study of the footwall rocks to the Sudbury Igneous Complex (North and East ranges)
Name of Candidate Nom du candidat	Enright, Jeff
Degree Diplôme	Master of Science
Department/Program Département/Programme	Geology
Date of Defence Date de la soutenance	March 18, 2019

APPROVED/APPROUVÉ

Thesis Examiners/Examinateurs de thèse:

Dr. Dan Kontak
(Co-Supervisor/Co-directeur de thèse)

Dr. Andrew McDonald
(Co-Supervisor/Co-directeur de thèse)

Dr. Lisa Gibson
(Committee member/Membre du comité)

Dr. John Spray
(External Examiner/Examinateur externe)

Approved for the Faculty of Graduate Studies
Approuvé pour la Faculté des études supérieures
Dr. David Lesbarrères
Monsieur David Lesbarrères
Dean, Faculty of Graduate Studies
Doyen, Faculté des études supérieures

ACCESSIBILITY CLAUSE AND PERMISSION TO USE

I, **Jeff Enright**, hereby grant to Laurentian University and/or its agents the non-exclusive license to archive and make accessible my thesis, dissertation, or project report in whole or in part in all forms of media, now or for the duration of my copyright ownership. I retain all other ownership rights to the copyright of the thesis, dissertation or project report. I also reserve the right to use in future works (such as articles or books) all or part of this thesis, dissertation, or project report. I further agree that permission for copying of this thesis in any manner, in whole or in part, for scholarly purposes may be granted by the professor or professors who supervised my thesis work or, in their absence, by the Head of the Department in which my thesis work was done. It is understood that any copying or publication or use of this thesis or parts thereof for financial gain shall not be allowed without my written permission. It is also understood that this copy is being made available in this form by the authority of the copyright owner solely for the purpose of private study and research and may not be copied or reproduced except as permitted by the copyright laws without written authority from the copyright owner.

Thesis Abstract

In the North and East range footwall rocks of the 1.85 Ga Sudbury Igneous Complex (SIC), quartz and plagioclase (An_{20-30}), plastically deformed prior to the emplacement of the SIC, were thermally annealed, resulting in their replacement by aggregates of strain-free grains that coarsen towards the SIC footwall contact due to radiant heat. In the Victor footwall deposit, SIC East Range, granoblastic polygonal quartz was overprinted by dynamically recrystallized quartz, with microstructures indicative of bulging (BLG) recrystallization. Incipient melting at quartz-plagioclase interfaces in Victor footwall rocks is recorded as interstitial plagioclase seams in quartz with quartz-quartz-plagioclase dihedral angles that peak at ~40 º, characteristic of wetting angles. Subsequent fluid-mediated modification of least-altered plagioclase (An_{20-30}) generated porous albite (An_{0-10}) through a coupled dissolution-precipitation (CDP) mechanism, which was likely contemporaneous with the crystallization of secondary epidote-group minerals. In the Victor footwall, textures and mineral chemistry of plagioclase, epidote- and chlorite-group minerals support the notion that a relatively oxidized, acidic, Fe-bearing fluid with a temperature of ~310 – 385 ºC favoured quartz-plagioclase interfaces as grain-scale fluid pathways, preferentially dissolving the anorthite component of plagioclase and creating void space prior to formation of disseminated chalcopyrite proximal to massive Cu-rich sulfide veins in the footwall setting.

Keywords: contact metamorphism, static recrystallization, dynamic recrystallization, annealing neoblast, feldspar twinning, partial melting, coupled dissolution-precipitation, chalcopyrite, epidote, monazite, Sudbury Igneous Complex

Co-authorship statement

The research presented in this thesis was sponsored by Vale and funded through CEMI with the process facilitated by Dr. Damien Duff, formerly with CEMI. The main proposal and project goals were developed by Dr. Peter Lightfoot and Lisa Gibson of Vale. Chapter 1 is written as a manuscript intended for peer-review journal publication and is co-authored by Drs. Daniel Kontak and Andrew McDonald of Laurentian University and Lisa Gibson of Vale. The first draft of the manuscript and initial interpretations were completed by the candidate. The finalized manuscript was edited and improved by scientific input and discussions with the co-authors.

Acknowledgments

I’d like to express gratitude to my supervisors Daniel Kontak and Andrew McDonald for their guidance through this study. I’d like to thank Willard Desjardins for his hard work in preparing thin sections and William Zhe and Remy Poulin for all of their assistance in the SEM and microprobe lab. I’d like to thank Edda and Roxane for always being available to help with any issues I have around the office. Lastly, I’d like to thank my friends and colleagues in the Earth Sciences Department of Laurentian University.

Table of Contents

List of Figures

List of Appendices

Chapter 1: Journal Paper

A textural and mineralogical study of the footwall rocks to the Sudbury Igneous Complex (North and East ranges)

Jeffrey M. Enright[1], Daniel J. Kontak[1], Andrew M. McDonald[1] and Lisa Gibson[2]

1. Harquail School of Earth Sciences, Laurentian University, 935 Ramsey Lake Rd, Sudbury, Ontario, Canada P3E 2C6
2. Vale Exploration, North America, 337 Power St., Copper Cliff, Ontario, Canada P0M 1N0

1.1 Abstract

In the North and East range footwall rocks of the 1.85 Ga Sudbury Igneous Complex (SIC), quartz (Qtz) and plagioclase (Pl) (An_{20-30}), plastically deformed prior to the emplacement of the SIC, underwent processes of recovery and recrystallization resulting in their replacement by aggregates of strain-free grains that coarsen towards the SIC footwall contact. The observed textural features are attributed to radiant heat from the overlying superheated melt sheet. In the Victor footwall deposit of the East Range, a Cu-rich vein-type deposit, the felsic gneiss host rocks reveal dynamic recrystallization of Qtz, recorded as undulatory extinction, flattened grains, and intra-grain bulges that overprint earlier granoblastic polygonal Qtz, indicative of bulging (BLG) recrystallization corresponding to Regime 1 dislocation creep. Incipient melting at Qtz-Pl interfaces occurred at least ~80 m from the inferred SIC contact in the Victor footwall, manifested as interstitial Pl seams in Qtz with Qtz-Qtz-Pl dihedral angles that peak at ~40 º, characteristic of wetting angles. Subsequent fluid-mediated modification of least-altered Pl (An_{20-30}) generated porous albite through a coupled dissolution-precipitation mechanism, occurring preferentially along Qtz-Pl interfaces and Pl neoblast boundaries. The formation of porous albite was likely concurrent with the crystallization of fine-grained, secondary epidote-group minerals, the replacement of annite-phlogopite by chlorite and clinozoisite-epidote, the replacement of ilmenite and rutile by titanite, and the replacement of flame perthite in K-feldspar by porous patch perthite and fine-

grained clinozoisite. In the Victor footwall, textures and mineral chemistry of plagioclase, epidote- and chlorite-group minerals support a model where a relatively oxidized, acidic, Fe-bearing fluid at ~310 – 385 ºC favoured Qtz-Pl interfaces as grain-scale fluid pathways. This fluid preferentially dissolved the anorthite component of plagioclase, thereby creating void space prior to deposition of disseminated chalcopyrite in the felsic wall rock proximal Cu sulfide-rich footwall veins.

1.2 Introduction

The study of both physical and chemical changes in minerals in response to variable PTX conditions provides valuable insights into the nature of geological processes. For example, both during and following the application of stress, mineral grains will undergo processes of recovery and recrystallization, with new strain-free grains forming as a result (Hirth & Tullis 1992; Lafrance *et al.* 1996; Park *et al.* 2001; Passchier & Trouw 2005). Through the application of a heat treatment (*i.e.* annealing), recovery and recrystallization processes are enhanced. Insights into previous processes can be elucidated by observations of the micro-deformational and annealed textures that are retained. In the presence of a fluid, unstable minerals may be replaced by neomorphs having a new, stable composition and crystallographic structure, through which the byproduct may be porosity-permeability (Putnis 2009; Putnis & Austrheim 2010; Norberg *et al.* 2013). Whereas the processes responsible for changes in minerals may involve radically different mechanisms, they are each driven to attain an atomic configuration that achieves a lower free-energy state.

The footwall to the 1.85 Ga Sudbury Igneous Complex (SIC) in Ontario, Canada, offers a unique opportunity to observe the effects of fairly dramatic changes in temperature, stress and hydrothermal activity on common rock forming minerals such as quartz, plagioclase, K-feldspar and biotite. The distinct assemblage of minerals and mineral textures present in the North and East range SIC footwall rocks was generated within an expansive thermal aureole (Dressler 1984b; McCormick *et al.* 2002; Boast & Spray 2006), not unlike the aureoles of intrusive complexes such as the Ballachulish Igneous

Complex in Scotland (Buntebarth & Voll 1991; Pattison & Harte 1997; Clemens & Holness 2000), and the Duluth Igneous Complex in Michigan (Benko *et al.* 2015). In addition to revealing insights into the processes and conditions responsible for changes in minerals, an understanding of how and why the particular minerals and textures developed in the SIC footwall can help to constrain the relative timing and ground preparation conditions that governed the development of significant deposits of Cu-Ni-(PGE) sulfides in the SIC footwall rocks (Ames & Farrow 2007; Ames *et al.* 2008).

The focus of this contribution is on the thermal annealing and subsequent modification of the high-grade gneisses and granitoid rocks that form the North and East range footwalls to the SIC. Changes in textures, mineralogy and mineral chemistry of both major and accessory minerals were documented and quantified in order to reveal information on the geological processes that affected the footwall rocks prior to and following the emplacement of the SIC. The work here demonstrates that the measurement of textures using petrographic and scanning electron microscopes, supported by mineral chemistry, is an appropriate and effective technique. Particular emphasis was placed on measuring mineralogical changes as both a function of distance to the SIC footwall contact, and as a function of proximity to sulfide mineralization. Furthermore, this study explores the role that these changes might have played in facilitating the development of chalcopyrite in the Victor footwall deposit.

1.3 Geological Setting

The 1.85 Ga Sudbury Structure (Fig. 1a), located at the junction of the Superior, Southern and Grenville Provinces in Ontario, Canada, is regarded as being either the eroded remnant of a multi-ring impact crater with an original transient diameter of ~250 km (Dietz 1964; Dressler 1984b; Krogh *et al.* 1984; Grieve *et al.* 1991; Grieve 1994; Stöffler *et al.* 1994) or the result of endogenic processes (Muir

1984). It is defined by three major components: (1) the 60 x 30 km ellipsoidal Sudbury Igneous Complex (SIC), a crystallized melt sheet with an estimated initial temperature of 2000K or more (Ivanov & Deutsch 1999; Prevec & Cawthorn 2002); (2) sedimentary and volcaniclastic rocks of the Whitewater Group which form the crater fill; and (3) brecciated footwall rocks. Underlying the South Range of the Sudbury Structure are Paleoproterozoic metavolcanic and metasedimentary rocks of the Huronian Supergroup, and the intrusive rocks of the Murray and Creighton plutons. Forming a collar 0.5 to 5 km along the North and East ranges of the SIC are rocks of the Levack Gneiss Complex (LGC), consisting of massive to foliated gneissic and migmatitic rocks, and felsic plutonic rocks of the Cartier Batholith. The LGC is considered by Dressler (1984a) to represent a high-grade metamorphosed sequence of clastic sedimentary rocks and mafic to felsic volcanic rocks. Card (1994) defined the major lithological units of the LGC as: (1) tonalite and related diatexite, forming 40% of the complex; (2) intermediate and mafic gneiss; (3) biotite paragneiss and related diatexite; (4) foliated granodiorite; and (5) gabbroic, dioritic and pyroxenitic intrusions and inclusions.

The rocks of the LGC record at least three stages of deformation and metamorphism, with rocks recording peak granulite facies metamorphism locally preserved. The LGC yields primary ages ranging from 2711 ± 7 to 2635 ± 5 Ma (Krogh *et al.* 1984; Ostermann *et al.* 1996; Ames *et al.* 2008). Peak granulite facies metamorphism is constrained between 2647 ± 2 Ma, the age of a leucosome layer (Krogh *et al.* 1984), and 2644 Ma ± 3 Ma, the age of an intermediate to felsic, cross-cutting pluton. James *et al.* (1992) gave minimum *P* and *T* conditions of 750 – 900 ºC and 6 – 8.5 kbars for the highest-grade facies of metamorphism, corresponding to depths of 20 to 30 km. This period was followed by regional amphibolite facies retrograde metamorphism corresponding with uplift to depths of 5 to 11 km (*i.e.* 1.6 – 3.6 kbar), which is thought to have broadly coincided with regional extension (Card 1994; Roussel *et al.* 1997), large-scale partial melting of the LGC, and the emplacement of the Cartier

Batholith (2642 ± 1 Ma, Meldrum *et al.* 1997). The 1.85 Ga Sudbury Event coincided with north- to north-west compression associated with the Penokean Orogeny, which is responsible for producing the characteristic ellipsoidal shape of the Sudbury Structure (Card *et al.* 1984; Zolnai *et al.* 1984; Corfu & Andrews 1986; Bennett *et al.* 1991; Shanks & Schwerdtner 1991*a*, 1991*b*; Lenauer & Riller 2012; Santimano & Riller 2012).

A result of the Sudbury Event was the extensive fracturing of the footwall rocks and the formation of pseudotachylite breccia, known as Sudbury breccia (SUBX), which occurs as veins and dykes up to 100s of metres wide (Fedorowich *et al*. 1999; Roussel *et al*. 2003). A contact metamorphic aureole generated by the heat of the SIC extended ~1 km from the SIC contact, and produced four distinct metamorphic zones that are best preserved along the North Range: (1) an innermost anatectic facies (*i.e.* granite breccia) (≤25 m); (2) a pyroxene hornfels facies (≤180 m); (3) a hornblende hornfels facies (≤180 m); and (4) an albite-epidote hornfels facies (≤1000 m) (Dressler, 1984a; Coats & Snajdr, 1984; Boast & Spray, 2006). Within the aureole, microscopic recrystallization and recovery textures in quartz and plagioclase have been documented, including the development of strain-free grains that replace primary crystals and coarsen towards the SIC footwall contact (Boast & Spray, 2006; Lafrance *et al.* 2008; Kontak *et al.* 2015). Thermobarometric studies of regions of localized, SIC-induced partial melting in the footwall yielded maximum temperatures of 850 – 900 ºC at least 200 m from the footwall contact (Péntek *et al.* 2009) and 650 ºC at 1 km (Prevec & Cawthorn 2002). Dressler (1984b) estimated that the Sudbury Structure has a depth of erosion of 5 km, corresponding with pressures of ~1.6 kbar.

1.4 The Victor Deposit

The Victor Deposit, located on the East Range of the SIC (Fig. 1a), in close proximity to the Capre and Nickel Rim South deposits, is host to contact and footwall-style mineralization (Morrison *et al.* 1994; Ames & Farrow 2007; Lightfoot 2015). Contact mineralization is hosted in sublayer norite and granite breccia units (*i.e.* the footwall breccia or late granite breccia unit; see Lightfoot 2016) and is concentrated in a series of structural embayments along the base of the SIC known as the Victor Trough (Fig. 1c; Jago *et al.* 1994; Lightfoot 2016). Contact mineralization is dominated by lenses of massive pyrrhotite + pentlandite > chalcopyrite, exhibits high Ni/(Ni+Cu) tenor ore relative to footwall-style deposits, and is connected to the underlying footwall-style deposits by a transition zone of chalcopyrite + pentlandite. With increasing depth, the footwall-type deposits grade from chalcopyrite + pentlandite into chalcopyrite + pentlandite + millerite, through bornite + chalcopyrite + millerite, to bornite + chalcopyrite, and veins of native silver (Lightfoot 2016).

While footwall-type sulfides in the North and East ranges are traditionally associated with zones of Sudbury Breccia (Morrison *et al.* 1994; Lafrance *et al.* 2008), they are also hosted in relatively cohesive, unbrecciated country rock lithologies, including the gneissic, migmatitic, granitoid and intermediate to mafic rocks defined by Card (1994). In the Victor footwall, the dominant mineralized, non-brecciated rock type observed is a massive- to foliated granitoid with a variable proportion of quartz, plagioclase and K-feldspar. The overall texture of the rock is controlled by the relative distribution, modal abundance, and grain sizes of three major mineralogical domains: (1) cloudy plagioclase-rich domains composed of fine-grained, interlocking mosaics, intergrown with aggregates of granoblastic quartz (Fig. 2a); (2) medium- to coarse-grained, blocky, pinkish to pale purple-coloured K-feldspar (Fig. 3b); and (3) dark greenish-grey domains, identified petrographically and through SEM-EDS as a variable assemblage of fine-grained chlorite-group minerals + clinozoisite-epidote + titanite + actinolite-tremolite ± annite-

phlogopite ± ilmenite ± apatite ± magnetite. The major mafic domains occur as clots and small interstitial veinlets of variable size and distribution (Fig. 3a), bands that define a compositional layering with alternating quartzo-feldspathic layers (Fig. 2c), and as rafts and enclaves (Fig. 2d).

Common textures of footwall-style sulfide mineralization are disseminations, stringers and veinlets that are interstitial to silicate phases (Fig. 2e, f, g), and massive to semi-massive veins up to several metres wide (Fig. 2h). Lining the margins of sulfide is an assemblage of clinozoisite-epidote + albite + chlorite + actinolite-tremolite ± titanite (Fig. 2b, e, f, g, h).

Lithologies sampled as part of this study are classified on a QAP ternary diagram (Fig. 3), whereas the paragenetic evolution of the minerals of interest to this study is illustrated in Figure 4. The mineral phases that exhibit textural evidence of having existed prior to 1850 Ma are assigned to 'Pre-Sudbury Event'. Mineralogical changes generated following and as a result of the Sudbury Event are assigned to a relatively high-T, contact-metamorphic stage, including the sub-solidus recrystallization of quartz and feldspar, and a low-T, retrograde/hydrothermal stage, corresponding to the dissolution of the footwall rocks and formation of hydrous mineral phases.

1.5 Sampling and Methods

Drill core from two bore holes in the Victor footwall, provided by Vale, was logged and sampled. Both holes were drilled approximately perpendicular to the SIC footwall contact, intercepting both mineralized and unmineralized zones. Grab samples were collected from road cuts at selected intervals along Highway 144, NW of the town of Onaping-Levack. Samples were collected up to 7400 m horizontal from the inferred SIC footwall contact. Forty-seven representative samples from Victor drill core were prepared as polished thin sections, and thirteen polished thin sections were prepared from

the Highway 144 grab samples. Mineral identification and characterization of textural features were carried out in plane-polarized light, cross-polarized light, and reflected light using a research-grade petrographic microscope. Quantification of mineral modal abundances and mineral textural features (*e.g.* grain sizes, aspect ratios, dihedral angles) was facilitated through the analysis of petrographic and back-scattered electron photomicrographs created from the SEM, processed using ImageJ.

Mineral chemistry and additional mineral identification was carried out at the Mineral Analytical Facility at Laurentian University. Selected polished thin sections were carbon coated, and minerals were analyzed semi-quantitatively by scanning electron microscope (SEM-EDS). A solid-state (Oxford-Sight) energy dispersive detector mounted on a JEOL 6400 SEM was utilized with a 15 kV accelerating voltage, a 1 nA beam current, acquisition times between 10 and 30 seconds, and at a working distance of 15 mm. Mineral chemistry of chlorite- and epidote-group minerals was acquired using a Cameca SX-50 Electron Probe Micro Analyzer (EPMA). The instrument operated with a focused beam of 1 um using a WDS routine, a beam current of 20 nA, an accelerating voltage of 20 kV, and a total count time of 30 seconds.

Cathodoluminence (CL) images of quartz from selected carbon-coated polished thin sections was acquired using an SEM-CL detector. The CL system has an HKL Backscatter Diffraction unit and a GatanChromaCL mirror-type cathodoluminescence (CL) detector and a linear array photomultiplier tube with 16 separate photocathodes. The SEM-CL images were collected using an accelerating voltage of 20 kV and a beam current of 1nA.

1.6 SIC North Range Transect

Grab samples were collected from road cuts at selected intervals along Highway 144, which runs along a line roughly perpendicular to the inferred SIC footwall contact (Fig. 1a, b). The purpose of this sampling was to document textural and mineralogical changes within footwall rocks as a function of proximity to the SIC contact. Samples of quartz-, plagioclase- and K-feldspar-rich gneisses and granitoid rocks of the LGC were chosen to facilitate a comparison with mineralized and unmineralized quartzo-feldspathic rocks sampled from the Victor footwall. As it was possible to collect grab samples from outcrops along Highway 144 at much greater distances from the footwall contact than was possible with Victor drill core, this allowed easier identification of precursor textures and mineralogy that were relatively unmodified by the effects of the 1850 Ma Sudbury event.

1.6.1 General geology and macro-textural features

Along Highway 144, quartzo-feldspathic rocks are massive to foliated, with foliation being defined by the compositional layering of alternating felsic and mafic bands with spacings up to 2 cm. The footwall rocks vary in their degree of compositional layering, and the grain sizes of quartz, plagioclase and K-feldspar are variable between samples, but three major domains predominate: (1) white-coloured plagioclase locally stained to a salmon colour and intergrown with anhedral quartz (Fig. 5a); (2) pink- to red-coloured, blocky K-feldspar that is intergrown with anhedral quartz (Fig. 5b); and (3) dark-grey domains of fine- to medium-grained minerals, defined by a least-altered assemblage of annite-phlogopite + actinolite-tremolite (massive-textured) + ilmenite + magnetite + apatite that has been variably replaced by an assemblage of chlorite + clinozoisite-epidote + actinolite-tremolite (acicular-textured) + titanite. Replacement textures and mineralogy are discussed in more detail in subsequent sections. Mafic domains occur as patchy clots and thin discontinuous veinlets that are

interstitial to quartz and plagioclase (Fig. 5a), as layers up to 1 cm that define a compositional layering with alternating leucocratic layers (Fig. 5b, c), and as rafts and enclaves up to 20 cm wide in sharp contact with the surrounding quartzo-feldspathic material (Fig. 5d, e). Leucocratic patches and dykes are present in both felsic and mafic rocks, and are defined by a coarse-grained intergrowth of quartz and feldspar with a low average modal abundance (<5%) of mafic minerals (Fig. 5b, d, f). It cannot be stated with confidence whether these domains represent the leucosome, melanosome or paleosome components generated as a result of partial melting.

1.6.2 Quartz

Parent quartz occurs as anhedral grains with highly variable cuspate-lobate-embayed-straight grain margins in contact with plagioclase (Fig. 5g, h); it has been replaced to varying degrees by newer, smaller grains (*i.e.*neomorphs). Sub-equant inclusions of quartz averaging 0.2 mm occur in trace amounts within plagioclase and K-feldspar, and usually include at least one well-developed crystal face. Photomicrographs of representative deformation, recovery and recrystallization microstructures in quartz from samples collected on the Highway 144 transect are shown in Figure 6. These images emphasize the textural changes observed in quartz within North Range footwall rocks as a function of distance from the SIC footwall contact. The approximate horizontal distance measured from the sample to a 'baseline' is shown on each photomicrograph. As the SIC footwall contact was not directly observed, the baseline is considered to be the closest sample taken from the inferred contact, and was given a value of 0 m. In each sample, parent quartz grains and new quartz grains were assessed quantitatively by measuring the dihedral angles, grain sizes, and aspect ratios of 25 randomly selected new grains in each sample (Figs. 7 and 8). Modal abundances of new quartz grains, normalized to total

quartz, and their crystal morphologies, defined as either anhedral or polygonal for simplicity, were estimated and are given in Figure 8a.

In the most distal samples, taken at distances of approximately 7400 m and 7250 m from the baseline (Fig. 6a, b, c), parent quartz occurs as anhedral grains up to 11 mm in length with median aspect ratios of roughly 2:1. Patchy to sweeping undulatory extinction in quartz is pervasive. In these samples, 50 percent or more of the total parent quartz has been replaced by newer, smaller grains with median aspect ratios of roughly 1.5:1, and variable straight- to interlobate grain boundaries. The distribution and development of the newer grains at the thin section scale is heterogeneous: some parent quartz grains have been almost entirely replaced by newer, smaller grains, while other parent grains show limited replacement by new grains. In the latter case, the new grains are typically concentrated along the grain boundaries of the parent quartz, producing a core-and-mantle structure. Only those new grains with well-developed, straight crystal faces were observed to exhibit straight extinction.

In samples taken at approximately 2300 m from the baseline, subgrains and new grains are relatively poorly developed, and quartz exhibits micro-deformational features that are consistent with the accumulation of lattice strain. Patchy- to sweeping undulatory extinction (Fig. 6d) is pervasive, and deformation lamellae, which appear as linear bands of differing extinction (Trepmann & Stöckhert 2003; Vernooij & Langenhorst 2005), were locally observed (Fig. 6e, f). Where they do occur, new grains are dominantly anhedral with median aspect ratios of over 1.5:1.

At approximately 500 m, there is a pronounced change in the overall texture and style of new quartz grains. Parent quartz grains dominate the samples and exhibit patchy- to sweeping undulatory extinction. Locally, parent quartz grains are replaced by chessboard-type subgrains (Fig. 6g). Poorly developed, anhedral subgrains and new grains with diffuse, interlobate margins occur preferentially along quartz grain boundaries (Fig. 6h). Elongate subgrains and new grains locally cross-cut ribbons of extinction

(Fig. 6i), and their intersection at right angles results in a chessboard-type extinction pattern. Locally, aggregates of new, granoblastic-polygonal quartz with straight grain boundaries, straight extinction and dihedral angles approaching 120 º replace entire parent quartz grains (Fig. 6j). From samples thereon in and approaching the SIC footwall contact, parent quartz is almost entirely replaced by aggregates of strain-free, granoblastic polygonal quartz (Fig. 6k, l and 8a). These aggregates are comprised of grains with dihedral angles approaching 120 º (Fig. 7), which on average coarsen towards the footwall contact (Fig. 8b). The median aspect ratio of the grains is approximately 1.2:1 (Fig. 8c). The development of granoblastic polygonal quartz is responsible for the decreasing trend observed in the median grain size of parent quartz, as parent quartz is progressively replaced by smaller, strain-free grains.

1.6.3 Plagioclase feldspar

Two textural populations of plagioclase were identified in North Range footwall rocks. Medium- to coarse-grained plagioclase up to 8 mm in length, hereafter referred to as Pl1, occurs as anhedral to subhedral grains with aspect ratios rarely exceeding 2:1. Micro-deformational features, including bands of extinction, kink-bands, and micro-offsets, all of which commonly cross-cut well-developed polysynthetic twinning, can also be observed in Pl1 grains (Fig. 9a, b, c). Rarely were glide twins observed.

A second population of plagioclase (Pl2) occurs as: (1) finer-grained and isolated subhedral- to euhedral prismatic neoblasts in Pl1 that commonly exhibit a simple twin parallel to the long axis of the grain (Fig. 9d), and (2) interlocking mosaics of fine-grained, prismatic- to sub-equant neoblasts in Pl1 that are locally granoblastic or log-jam-textured (Fig. 9e, f). In the sample where the Pl2 neoblasts are first observed at ~500 m from the baseline, ~40% of measured neoblasts display a simple twin, whereas in samples taken within ~150 m of the baseline, over 90% of measured neoblasts display a simple twin.

The Pl2 neoblasts are compositionally similar to their parent Pl1 grain, so cannot be distinguished visually using SEM-BSE imaging. In contrast to grains of Pl1, which are largely anhedral, Pl2 neoblasts are relatively well-formed with at least one well-developed crystal face. The Pl2 neoblasts are preferentially localized along Pl1 grain boundaries and along linear features cross-cutting Pl1 (Fig. 9f), possibly representing relict fractures or micro-deformational features as seen in Figure 7a, c.

Plagioclase (Pl1) grain boundaries containing a high concentration of Pl2 neoblasts are highly irregular and exhibit frequent intra-grain bulges. Bulges are both rounded and orthogonal, commonly projecting from a common Pl1 grain into a neighbouring Pl1 grain (Fig. 9d). Patches of extinction occur locally within the interiors of Pl1 grains, at times forming a prismatic to sub-equant silhouette with no discernible change in relative relief (Fig. 9e). A transitional stage exists where certain Pl2 neoblasts are nearly indistinguishable from neighbouring bulges and patches of extinction. Transitional grains have diffuse grain boundaries, low relief relative to the surrounding Pl1, and relatively poorly formed prismatic morphologies (Fig. 9g, h, i). In contrast to intra-grain bulges in Pl1, these poorly-formed, transitional neoblasts go extinct independently from the parent Pl1 grain, thus identifying them as discrete, independent grains or subgrains. They may exhibit an extinction pattern that sweeps across the grain, roughly parallel to the grain's long axis, rather than a well-defined simple twin (Fig. 9g, h, i). As seen in the development of new, strain-free grains in quartz, the modal abundance and average grain size of Pl2 increases when approaching the baseline sample from ~500 m (Fig. 10a, b). The increase in neoblast grain size is typically accompanied by an increase in aspect ratio (Fig. 8b). The positive trend between neoblast grain size and aspect ratio may be a result of the different orientations of the Pl2 neoblasts with respect to the thin section surface, such that some longer grains are simply lying with their *c*-axis parallel to the stage. Conversely, grain-coarsening of Pl2 neoblasts may develop faster along the *c*-axis relative to that along other crystallographic axes.

1.6.4 Fine-grained accessory minerals in plagioclase

A secondary mineral assemblage of fine-grained epidote- and chlorite-group minerals + titanite + K-feldspar + muscovite ± actinolite-tremolite (Fig. 11a, b) occurs preferentially along planar weaknesses in plagioclase, including Pl1–quartz interfaces (Fig. 11c), Pl2–Pl2 grain boundaries (Fig. 11d, e, f, g), cleavage planes, fractures, and kink bands. Where neoblasts are developed in plagioclase, fine-grained epidote-group minerals, chlorite-group minerals, and K-feldspar are present within the neoblast grain interiors, as well as within interstices between the neoblasts. Fine-grained epidote-group minerals (± titanite and actinolite-tremolite) are locally overgrown by fine-grained chlorite-group minerals (Fig. 11a, f). Plagioclase with a relatively high density of fine-grained secondary minerals appears dusty or turbid when viewed under plane-polarized light (Fig. 11c). Semi-quantitative analyses by SEM-EDS of least-altered plagioclase in North Range gneissic and granitoid footwall rocks (*i.e.* tonalite, monzogranite, granodiorite) indicate that it has an average composition of oligoclase (An_{20-30}). An increase in the concentration of fine-grained secondary minerals in plagioclase generally corresponds with a decrease in the anorthite component of plagioclase (Fig. 11h). Furthermore, a positive trend was observed between the concentration of fine-grained epidote-group minerals in plagioclase and concentration of porosity in plagioclase (Fig. 12). The maximum concentration of porosity measured was up to ~4%. The relationship between the concentration of porosity and other accessory phases in plagioclase (*i.e.* chlorite-group minerals + titanite + K-feldspar + muscovite ± actinolite-tremolite) was not measured, as they were commonly observed in only trace amounts. In North Range footwall rocks, the average and maximum diameters of micropores in plagioclase were measured at 2 μm and 4 μm, respectively.

1.6.5 K-feldspar

Four textural populations of K-feldspar were identified in North Range footwall rocks (Fig. 13): (1) medium- to coarse-grained K-feldspar with a distinct perthitic texture (Kfs1); (2) prismatic, Carlsbad-twinned neoblasts (Kfs2); (3) fine-grained, stubby-prismatic to sub-equant neoblasts forming interlocking mosaics (Kfs3); and (4) irregular-shaped, anhedral 'islands' of non-perthitic K-feldspar in plagioclase (Kfs4).

Grains of Kfs1 up to 15 mm (Fig. 5h) occur as anhedral crystals with a blocky, sub-equant crystal habit. Most grains are untwinned and have a turbid appearance. Only the most distal Kfs1 grains (>7000 m) exhibit tartan twinning. Two cleavages intersecting at angles of roughly 90º were rarely observed. In samples within 150 m from the inferred SIC footwall contact, medium- to coarse-grained crystals of Kfs1 are partially replaced by K-feldspar neoblasts that are texturally similar to the fine-grained neoblasts developed in plagioclase (Pl2). In contrast to the uniformly fine-grained Pl2 neoblasts, K-feldspar neoblasts are texturally bi-modal (Kfs2 and Kfs3), forming two populations that are distinguished based on their grain size, crystal habit, and twinning.

The Kfs2 neoblasts occur as subhedral- to euhedral, prismatic, Carlsbad-twinned crystals up to 1 mm in length and with aspect ratios up to 3:1 (Fig. 13a). Crystal faces are commonly straight, particularly those which are parallel to the long axis of the grain, though they may be scalloped and embayed. Grains of Kfs2 occur preferentially adjacent Kfs1 grain boundaries, Kfs1–quartz interfaces, and Kfs1–plagioclase interfaces, commonly with the long axis of the grain oriented sub-perpendicular to the grain boundary or interface. Locally, grains of Kfs2 can only be identified by the presence of weakly developed Carlsbad twins, these showing a diffuse gradational twin-boundary. This effect was also observed with respect to poorly-formed plagioclase (Pl2) neoblasts (Fig. 9g, h, i).

Grains of Kfs3 occur as sub-equant to stubby-prismatic, fine-grained neoblasts averaging 0.1 mm and were observed to be spatially associated with prismatic, Carlsbad-twinned Kfs2 neoblasts (Fig. 13b). Grains of Kfs3 occur proximal to grain boundaries, mineral interfaces and linear features that cross-cut the parent Kfs1. Grains of Kfs3 form granoblastic mosaics that are texturally similar to those formed by Pl2 (Fig. 13c). Intra-grain bulges, as observed in plagioclase (Fig. 9d), were also observed to be spatially associated with Kfs2 and Kfs3 (Fig. 13a). Well-formed Kfs2 and Kfs3 neoblasts have a low- to medium-positive relief relative to their parent Kfs1 grain, though some neoblasts may be barely discernible, appearing as patches of extinction. In such cases, neoblast grain boundaries are diffuse, exhibiting no change in relief with respect to the surrounding Kfs1.

Patch perthite is ubiquitous in grains of Kfs1, Kfs2 and Kfs3 within 2300 m of the SIC footwall contact. Patch perthite occurs as intergrowths of anhedral albite and K-feldspar subgrains, which together pseudomorphously replace a parent K-feldspar grain, and is easily viewed in cross-polarized light and BSE imaging (Parsons & Lee (2009) and references therein). Patch perthite was observed as elongate arrays of parallel to sub-parallel lamellae of albite with irregular margins, up to 15 μm wide, in K-feldspar, and as fine-grained, anhedral blebs and patches of albite without a preferred orientation (Fig. 13d). Patch perthite frequently forms films of albite that contour grains of Kfs2 and Kfs3 (Fig. 13a), and was never observed to cross-cut either population of K-feldspar neoblasts. Further, patch perthite within Kfs2 and Kfs3 neoblasts was observed to be texturally distinct from patch perthite in the surrounding parent Kfs1 grain: (1) the relative concentration and grain sizes of albite blebs and/or lamellae inside and outside of the neoblasts appears to be different (Fig. 13f); and (2) the relative orientations of albite lamellae inside and outside the neoblasts is different. Flame perthite, defined by arrays of albite lamellae with relatively straight, sharp margins, was observed in grains of relatively non-turbid Kfs1 from distal samples (Fig. 13e). Cryptoperthite and microperthite were not observed in any samples.

High-magnification SEM-BSE images show that micropores up to 3 μm occur throughout patch perthite in both K-feldspar and albite domains (Fig. 13g). Fine-grained epidote-group minerals and rare Fe-oxides are disseminated throughout the patch perthite and are preferentially concentrated along the interfaces between the albitic and potassic domains.

A fourth textural population of K-feldspar (Kfs4) occurs as non-perthitic, anhedral islands up to 0.2 mm wide in plagioclase (Fig. 11g, 13h, i). Grain boundaries of Kfs4 are generally ragged. Kfs4 preferentially occurs as thin films along quartz-plagioclase interfaces, as elongate patches sub-parallel to polysynthetic twinning in plagioclase (Fig. 9f), and as irregular patches in plagioclase with no preferred orientation. Grains of Kfs4 also occurs in and around chlorite-group and epidote-group minerals that are pseudomorphs after biotite (Fig. 14i). Locally, Kfs4 occurs interstitially to plagioclase neoblasts (Fig. 11g). Grains of Kfs4 were rarely observed to contain inclusions of fine-grained epidote- and chlorite-group minerals; rather, the epidote- and chlorite-group minerals were observed to concentrate around the margins of Kfs4 patches. Grains of Kfs4 are both non-porous (Fig. 13h) and porous (Fig. 13i). Rocks in which plagioclase is pervasively altered across the entire thin section (*i.e.* abundant micropores and fine-grained epidote- and chlorite-group minerals ± muscovite ± actinolite-tremolite ± titanite) were observed to contain grains of porous Kfs4, whereas rocks in which the alteration of plagioclase was more localized were observed to contain grains of non-porous Kfs4. Further, bands and patches of porous albite were observed to locally intersect grains of Kfs4, with no corresponding increase in the density of micropores in Kfs4 (Fig. 13h).

1.6.6 Accessory minerals

In footwall rocks sampled along the North Range transect, the average modal abundance of minerals other than quartz, plagioclase and K-feldspar is generally less than 10%. The least-altered

mafic domains have a variable assemblage composed of annite-phlogopite + actinolite-tremolite (massive-textured) + ilmenite + magnetite + apatite (Fig. 14a). They occur as patchy, isolated clots and stringers, or may locally define a spaced foliation with alternating quartzo-feldspathic layers. When viewed petrographically, the platy- to prismatic mafic minerals (annite-phlogopite and actinolite-tremolite) are generally deflected around quartz, plagioclase and K-feldspar, whereas magnetite and ilmenite are interstitial to quartz and feldspar. Rounded, subhedral to anhedral apatite occurs as inclusions in annite-phlogopite, actinolite-tremolite, and plagioclase.

Tremolite-actinolite occurs as anhedral, to locally subhedral, prismatic crystals with cuspate-lobate-embayed margins when in contact with plagioclase and quartz, and sharp margins when in contact with annite-phlogopite. In plane-polarized light, it is pleochroic from pale green to pale brown, and in cross-polarized light, it exhibits average and maximum interference colours of first-order yellow-orange and second-order purple, respectively. Locally, massive actinolite-tremolite is in contact with aggregates of fine-grained, bladed to acicular actinolite-tremolite crystals (Fig. 14b). Contacts between the two phases appear ragged. In plane-polarized light, the colours of the acicular-textured crystals appear slightly duller than the massive actinolite-tremolite; they are weakly pleochroic from very pale green to very pale brown. In cross-polarized light, average and maximum interference colours are first-order yellow and second-order purple, respectively. Semi-quantitative mineral chemistry determined by SEM-EDS indicates that the massive actinolite-tremolite has a higher *Fe#* (Fe/(Fe+Mg)) than the acicular actinolite-tremolite (Fig. 15a). An Fe X-ray map of the grain boundary interface reveals a mottled zonation in the Fe content of acicular actinolite-tremolite, and the presence of discrete Fe-oxide phases along the interface (Fig. 14c).

Annite-phlogopite (Ann-Phl) occurs as anhedral, platy crystals up to 1 mm which contain inclusions of titanite that appear to be elongate within the Ann-Phl (001) plane (Fig. 14d). When viewed

down the *c*-axis, Ann-Phl crystals exhibit a sagenitic texture where very fine-grained needles of rutile intersect at angles of roughly 60 º, forming a stellate pattern, and fine-grained titanite lamellae form equilateral triangles with angles of roughly 60 º (Fig. 14g)

Chlorite occurs as a replacement of Ann-Phl (Fig. 14e) and as fine-grained plates and flakes disseminated in plagioclase (Fig. 11c). The interference colours of both replacement type and disseminated chlorite range from a deep *berlin* blue to an anomalous brown, and crystals are pleochroic from pale beige to medium green. At the thin section scale, biotite chloritization was observed in various stages of completion. When sections are viewed parallel to the (001), chlorite and Ann-Phl layers are interfingered, have sharp contacts, and tend to pinch out, as shown in (Fig.14e). When viewed down the *c*-axis, chlorite appears to preferentially replace Ann-Phl inwards from the margins (Fig. 14g). Fine-grained inclusions of quartz are locally present in chlorite, and appear to be elongate within the chlorite (001). Titanite lamellae intersecting at angles of roughly 60 º occur in chlorite as they do in Ann-Phl, and appear coarser-grained when compared to their occurrence in sagenitic Ann-Phl (Fig. 14h). High-magnification reflected light and SEM-BSE images of lamellae in chlorite locally show fine-grained anhedral rutile and ilmenite cores with titanite rims, set in mottled-textured chlorite (Fig. 14j). In Figure 15b, Fe/(Fe+Mg) and Al/(Al+Mg) ratios from spot analyses from a transect across a representative Ann-Phl-chlorite couplet are plotted, indicating a relative depletion in Fe and relatively constant Al during biotite chloritization.

Clinozoisite-epidote is present intergrown with chlorite in chloritized Ann-Phl (Fig. 14f, i) and as fine-grained prisms and laths disseminated in saussuritized plagioclase (Fig. 11a, b). In plane-polarized light, grains of clinozoisite-epidote range from colourless to weakly pleochroic (colourless to pale yellow), and in cross-polarized light interference colours are as high as third-order green. Generally, in samples where clinozoisite-epidote is pleochroic and exhibits third-order maximum interference colours,

the dominant interference colour of chlorite is *berlin* blue rather than an anomalous brown. This likely reflects a higher Fe content in each respective mineral (Deer *et al.* 1992), and may be indicative of a greater bulk-rock Fe concentration. Clinozoisite-epidote occurs as blocky, prismatic grains both parallel and perpendicular to the (001) plane in chlorite (Fig. 14f). The replacement of Ann-Phl and/or chlorite by clinozoisite-epidote and preservation of relict titanite, which may have been inherited from earlier sagenitic Ann-Phl, is demonstrated in Figure 14i. Titanite lamellae are somewhat irregular but do form triangles intersecting at roughly 60 º. Also present are fine-grained Fe-oxide inclusions, porous Kfs4 grains that both extend from and occur within the clinozoisite-epidote grain, and dark holes that may represent porosity. A physical connection was observed between the replacement clinozoisite-epidote and the fine-grained epidote-group crystals that extend into the surrounding plagioclase.

With respect to the minerals constituting the major mafic domains, the transition from Ann-Phl-dominant rocks to clinozoisite- and chlorite-dominant rocks coincides with an overall increase in the intensity of plagioclase alteration, defined by the occurrence of secondary features in plagioclase (*i.e.* porosity and fine-grained epidote- and chlorite-group minerals, muscovite, actinolite-tremolite and titanite). The total concentration of secondary features in plagioclase was evaluated in plane-polarized light based on plagioclase turbidity (Fig. 11c), and in cross-polarized light by identifying minerals by their interference colours. A visual estimate of the overall intensity of plagioclase alteration at the thin section scale was used to assign a relative rating and create a plagioclase alteration index (PAI). The plots of PIA against visual estimates of total modal chlorite and total modal clinozoisite-epidote (Fig. 16), normalized to the sum of modal chlorite, annite-phlogopite, and clinozoisite-epidote, indicate that: (1) least-altered samples are annite-phlogopite-dominated (Fig. 14d, g); (2) most-altered samples are dominated by clinozoisite-epidote and chlorite (Fig. 14f, i); and (3) samples in which the PAI falls

within the range between least-altered and most-altered (PAI = 2 – 3) are chlorite-dominated (Fig. 13e, h)

Magnetite and ilmenite are present as anhedral to subhedral grains up to 0.5 mm in length. They are typically localized to the major mafic domains (*i.e.* intergrown with annite-phlogopite + actinolite-tremolite + chlorite- and epidote-group minerals), but are frequently in contact with quartz and plagioclase, often at the boundary between a quartzo-feldspathic domain and an annite-phlogopite + actinolite-tremolite domain (Fig. 14a, k). While they do occur as individual, isolated grains, ilmenite and magnetite commonly form intergrowths with sharp, straight to slightly undulating contacts (Fig 14k). Titanite and fine-grained, anhedral rutile regularly occur as a partial replacement of ilmenite (Fig. 14l). Titanite is present as rims on ilmenite, along cross-cutting features, and as patchy clots in ilmenite. A thin film of chlorite and clinozoisite-epidote is commonly present along the outer margin of the titanite rim. Where rutile and titanite both occur as replacement products of ilmenite, titanite always surrounds rutile. Micron-sized holes are present in ilmenite grains that have been partially replaced by titanite and rutile. Magnetite grains commonly exhibit both trellis-textured and sandwich-textured ilmenite lamellae, which in turn have also been replaced by titanite.

1.7 Victor Footwall

1.7.1 Quartz

Four main textural varieties of quartz were identified in Victor footwall rocks: (1) aggregates of granoblastic polygonal quartz (Fig. 6k, l); (2) fine-grained, equant to sub-equant grains with interstitial feldspar (Fig. 17a, b, c), (3) graphic-textured quartz and K-feldspar (Fig. 17d); and (4) optically continuous, poikilitic quartz with inclusions of plagioclase laths (Fig. 17e).

Granoblastic polygonal quartz is the dominant textural variety of quartz within the Victor footwall, which is also described from rocks sampled within 150 m of the 'baseline' from the North Range footwall. The aggregates have variable cuspate-lobate-straight outer margins when in contact with plagioclase and K-feldspar, and contain strain-reduced, polygonal grains, with grain sizes averaging 0.3 mm. Aggregates of granoblastic quartz, which are locally deformed, are elongate and flattened with a shape preferred orientation (SPO), and locally occur parallel to ribbons of extinction (Fig. 17f). Undulatory extinction and deformation bands locally cross-cut quartz grain boundaries, and undulating, bulging grain boundaries transition into neomorphs that overprint pre-existing granoblastic polygonal quartz, producing a core-and-mantle structure (Fig. 17g). Under CL, deformation lamellae in quartz coincide with arrays of dark bands that cross-cut the grain boundaries of the granoblastic quartz. The quartz exhibits a blue-coloured CL emission (Fig. 17h). Micro-deformational features in granoblastic quartz are local at the thin section scale, such that other neighbouring aggregates exhibit no obvious signs of deformation.

Isolated, subhedral grains (<0.1 mm) of strain-free quartz with interstitial feldspar (plagioclase and K-feldspar) occur preferentially around the margins of granoblastic polygonal quartz aggregates (Fig. 17a), which in CL show a dark blue core and lighter rim. Interstitial feldspar is ubiquitous to this texture, forming thin seams that locally extend into adjacent polygonal quartz aggregates. Quartz-quartz-plagioclase and quartz-quartz dihedral angles were measured from a representative area and plotted in Figure 18. Dihedral angles between adjacent quartz and interstitial plagioclase grains peak sharply at ~40 º with a right-skewed distribution, starkly contrasting with the normally distributed curve made by dihedral angles within the adjacent granoblastic polygonal quartz aggregates, which peak at ~120 º.

Locally, optically continuous quartz, exhibiting undulose extinction, occurs in a graphic intergrowth with K-feldspar (Fig. 17d). Graphic to granophyric intergrowths of quartz and K-feldspar have been

well-documented in the North and East Range footwall environments (Molnár *et al*. 2001; Péntek *et al*. 2013). Optically continuous, oikocrystic 'flood' quartz, locally exhibiting undulatory extinction, occurs as an intergrowth with euhedral plagioclase laths. This texture was observed to directly transition into both K-feldspar-quartz granophyres (Fig. 17d) and isolated quartz with interstitial plagioclase seams (Fig. 17e). Oikocrystic quartz + lath plagioclase intergrowths were frequently observed in rocks with less than 23% modal quartz (QAP normalized), but were rarely observed in rocks with greater than 23% normalized modal quartz.

1.7.2 Plagioclase

Four major textural varieties of plagioclase are observed in Victor footwall rocks, including (1) patches of anhedral, deformed plagioclase (Pl1) (Fig. 19a); (2) mosaics of interlocking, fine-grained, stubby prismatic plagioclase (Pl2) (Fig. 19b, c); (3) prismatic plagioclase laths intergrown with quartz (Pl3) (Fig. 17e, f); and (4) blocky, subhedral to euhedral plagioclase in contact with sulfide (Pl4) (Fig. 19d).

Fine- to medium-grained, anhedral plagioclase (Pl1) with well-developed polysynthetic twinning occurs rarely. As observed in North Range footwall rocks, polysynthetic twins in Pl1 grains are bent, kinked, and offset, and grains exhibit undulatory extinction. Grains of Pl1 form irregular, relict patches that are replaced preferentially inwards from their outer margins by fine-grained, stubby prismatic to sub-equant neoblasts of plagioclase (Pl2) with aspect ratios up to 3:1. Whereas Pl2 is a relatively minor constituent in the footwall rocks sampled from the North Range, they are the dominant textural variety of plagioclase in Victor footwall rocks, forming equigranular, granoblastic to log-jam-textured mosaics that constitute, on average, over 95% of all the observed plagioclase. As in North Range footwall rocks, Pl2 neoblasts are commonly twinned on the Carlsbad law, though polysynthetic twinning is not

uncommon. Twinning is more prevalent in prismatic Pl2 neoblasts when compared to those which are polygonal to sub-equant in habit. Aggregates of Pl2 commonly mimic the prismatic outline of a precursor Pl1 grain that has since been replaced (Fig. 19b).

When intergrown with quartz, plagioclase (Pl3) forms euhedral laths that are fine- to medium-grained, with aspect ratios up to 10:1 (Fig. 17e). The quartz-Pl3 intergrowths occur as irregular patches and veins in the plagioclase (Pl2) groundmass. The laths are comb-textured from the intergrowth margins, and are increasingly randomly oriented towards the core of the intergrowth. The Pl3 laths are commonly entrained in optically continuous 'flood' quartz that exhibits a patchy undulatory extinction. Quartz-Pl3 intergrowths were observed to locally transition into aggregates of quartz with interstitial plagioclase seams (Fig. 17e).

Plagioclase grains of Pl1, Pl2, and Pl3 have a brownish, dusty appearance when viewed in plane-polarized light due to their pervasive replacement by fine-grained secondary minerals (epidote- and chlorite-group ± muscovite ± actinolite-tremolite ± titanite). When observed using BSE imaging, these secondary minerals occur alongside up to ~4% micropores in plagioclase, a relationship also seen in the more altered domains of plagioclase in North Range footwall rocks. The micropores have an average aspect ratio of 1.5:1 and average and maximum lengths of 2 μm and 6 μm, respectively, which are values similar to those measured from North Range footwall rocks.

Plagioclase (Pl4) in contact with sulfide mineralization occurs as subhedral to euhedral, prismatic grains up to 0.75 mm that are comparatively fresh and inclusion-free. In BSE imaging, these grains lack the development of microporosity that is present in Pl1, Pl2 and Pl3. Rather, grains of Pl4 are commonly intergrown with grains of clinozoisite-epidote and actinolite-tremolite that are comparable in grain size (Fig. 18d). Grains locally exhibit chess-board twinning, characterized by short, discontinuous twins that may appear stepped or terminate abruptly (Fig. 19e). Chess-board twinning has been

associated with metasomatically-generated albite that has subsequently been deformed (Starkey 1959; Callegari & Pieri 1967)

1.7.3 K-feldspar

In Victor footwall rocks, K-feldspar is present in each of the four textural populations described from North Range footwall rocks (Fig. 13). Grains of Kfs1 commonly show one good cleavage and one imperfect cleavage. As observed in North Range footwall rocks, K-feldspar occurs as mosaics of prismatic, Carlsbad-twinned neoblasts (Kfs2) up to 3 mm in length, and fine-grained, sub-equant grains (Kfs3) that locally replace coarser-grained Kfs1 (Fig. 19f). Whereas the vast majority of parent plagioclase (Pl1) has been replaced by Pl2 aggregates, leaving only rare, relict patches of precursor Pl1, the replacement of precursor Kfs1 by neoblasts of Kfs2 and Kfs3 is comparatively incomplete, with Kfs2 and Kfs3 constituting between 15% and 60% of all observed K-feldspar. Patch perthite is pervasive throughout most K-feldspar domains. When viewed in cross-polarized light, the albitic domains in the patch perthite exhibit polysynthetic twinning that is typically parallel to the long axis of the grain. Islands of fine-grained, anhedral Kfs3 in plagioclase are porous, non-perthitic, and do not typically exhibit the same linear morphology (*i.e.* linear arrays that are parallel to polysynthetic twinning in plagioclase) (Fig. 13h) that was observed in North Range footwall rocks. Rather, they occur as patches and thin films that appear to be interstitial to Pl2 neoblasts (Fig. 11g).

1.7.4 Accessory Minerals

Accessory mineralogy is subdivided into four major textural groups: (1) minerals constituting the dominant mafic domains, as defined in Fig. 2; (2) fine-grained secondary silicate minerals in plagioclase; (3) silicates in contact with sulfide minerals (*i.e.* selvage-type); and (4) veins that cross-cut

all lithologies and are filled with chlorite- and epidote-group minerals, quartz and rare carbonate. Trace accessory phases including zircon, monazite and allanite are localized within the fine-grained plagioclase aggregates. As shown in the mineral paragenesis (Fig. 4), Victor footwall rocks and North Range footwall rocks share many of the same textural populations of minerals. Thus, the mineral descriptions presented in this section are relatively short when compared with the earlier mineral descriptions.

The major mafic domains are a variable assemblage of chlorite- and epidote-group minerals + actinolite-tremolite + titanite + ilmenite + apatite ± annite-phlogopite ± magnetite. As observed in North Range footwall rocks, the mafic domains are present as patchy stringers and clots that wrap or are deflected around quartz, plagioclase and K-feldspar, and locally develop a compositional layering with alternating quartzo-feldspathic layers. In rocks that are dioritic to gabbroic in composition, annite-phlogopite and actinolite-tremolite are the dominant mafic minerals, whereas chlorite- and epidote-group minerals are the volumetrically dominant mafic phases in felsic rocks (*e.g.* tonalite, granodiorite and monzogranite).

Chlorite-group minerals are present in four main textural varieties: (1) a replacement product of annite-phlogopite, with up to 50% titanite and ilmenite that has developed in the (001) plane of chlorite (Fig. 14h); (2) medium-grained, anhedral patches with little to no titanite and ilmenite; (3) fine-grained, disseminated flakes in saussuritized plagioclase; and (4) subhedral to euhedral, radiating plates and rosettes in barren quartz-carbonate veins and in contact with sulfides.

Epidote-group minerals are present as: (1) fine- to medium-grained, prismatic grains; (2) crystals intergrown with chlorite, having replaced earlier annite-phlogopite; (3) fine-grained, disseminated prismatic grains in saussuritized plagioclase; and (4) subhedral to euhedral, prismatic grains in contact with sulfide and within sulfide-barren veins.

Actinolite-tremolite is present as: (1) aggregates up to 2 mm of bladed to acicular crystals, as described in North Range footwall rocks; (2) rare, fine-grained prismatic to acicular grains in plagioclase; and (3) subhedral to euhedral, prismatic grains lining the margins of sulfide and as inclusions in sulfide.

Ilmenite is present as: (1) anhedral to subhedral prismatic grains up to 0.5 mm in length and localized to the major mafic domains; and (2) rounded, sub-equant inclusions averaging 0.02 mm but rarely up to 1 mm in chloritized annite-phlogopite, and as acicular crystals that have developed in the (001) plane of chloritized annite-phlogopite. The partial replacement of ilmenite by titanite was observed in all samples where ilmenite is present, with the replacement appearing as a rim of titanite that progresses inwards along linear features towards the ilmenite grain core.

Monazite (Mnz) up to 1 mm is present as colourless to pale brown, anhedral, sub-equant, rounded inclusions in plagioclase, and rarely in annite-phlogopite and chalcopyrite. Grains of Mnz frequently exhibit varying degrees of neoblast development (Fig. 20a, b). These neoblasts have sharp boundaries, and upon rotation of the optical stage in XPL, discrete neoblasts go extinct at different orientations, as observed in the granoblastic polygonal quartz aggregates. Neoblast sizes and dihedral angles were measured from two representative, similarly sized Mnz grains (A and B) from the same sample, and are plotted in frequency diagrams (Fig. 20c, d). The MnzA grain is comprised of over 95% neoblasts, whereas the MnzB grain is comprised of less than 25% neoblasts. From MnzA, the average dihedral angle from a total of 102 measurements, equating to 34 triple junctions, was 119º ± 20.6%. From MnzB, the average dihedral angle for a total of 51 measurements, equating to 17 triple junctions, was 120º ± 26.6%. With respect to MnzA, 36% of total counts were within the range of 110º – 129º, whereas only 24% of MnzB counts were within that same range. Further, MnzA exhibits a more consistent distribution of neoblast sizes, with roughly 51% of measured neoblasts being 10 to 29 um in

length. MnzB exhibits a relatively bimodal distribution of neoblast grain sizes, with 52% of measured neoblasts being 10 to 29 um and 10% of neoblasts being 110 to 119 μm long. Thus, the development of neoblasts in Mnz at the thin section scale is a relatively heterogeneous process. This effect was also observed with respect to the recrystallization of quartz, where at roughly 500 m from the inferred North Range contact, the development of new, strain-free grains in quartz was quite variable.

The partial replacement of Mnz by apatite with a subsequent overgrowth by allanite is ubiquitous in the Victor footwall. Fine-grained, secondary apatite was observed to preferentially replace Mnz grains along their rims, neoblast grain boundaries and along cross-cutting fractures (Fig. 20e-j). Fine-grained, anhedral allanite is generally present as a rim to apatite cores. A Ce*L*α X-ray map demonstrates the apatite is relatively depleted in Ce compared to monazite and allanite. Fine-grained, disseminated epidote-group minerals are present in the surrounding plagioclase (An_{0-10}) groundmass, and a physical connection was observed between the allanite rim and the surrounding fine-grained clinozoisite-epidote grains (Fig. 20h). However, Ce (and other LREEs) are relatively restricted to within the boundaries of the allanite rim, diminishing in concentration over a sharp interval.

1.7.5 Mineral textures related to chalcopyrite mineralization

The main sulfide minerals in the Victor footwall are chalcopyrite (>80%) with lesser pyrrhotite, pentlandite, millerite and pyrite; thus, for the purposes of this section, sulfides will be collectively referred to as chalcopyrite (Ccp). Examples of Ccp macro-textural features were introduced in Figure 2 and three end-member Ccp textures are observed: (1) disseminations (Fig. 2e, g); (2) stringers and veinlets, (Fig. 2b, c, f); and (3) massive to semi-massive veins up to several meters wide that cross-cut the country rock (Fig. 2h).

Disseminations of Ccp occur preferentially in plagioclase (An_{0-10}), vary in size and shape, ranging from micron-size to 7 mm, and occur in isolation rather than occurring as interconnected aggregates. Micron-size Ccp grains are generally sub-equant and are spatially associated with zones of porous albite that contain a high density of fine-grained, disseminated epidote- and chlorite-group minerals ± muscovite ± titanite ± actinolite-tremolite (Fig. 21a, b, c). Locally, Ccp and associated fine-grained secondary minerals appear to occupy pits and depressions, which may represent micropores potentially generated during the coupled dissolution-precipitation (CDP) of plagioclase (Putnis 2002). With increasing grain size of Ccp (*i.e.* mm to cm scales), the disseminations are anhedral in shape, and may exhibit a greater degree of interconnectivity, such that they appear as veinlets.

The Ccp veinlets and disseminations occur interstitially to both quartz and an assemblage of subhedral to euhedral crystals of epidote- and chlorite-group minerals + albite + actinolite-tremolite ± titanite (Fig. 21d - i). The silicate assemblage that is in contact with Ccp forms a selvage (*i.e.* rim) up to 3 mm in thickness, appearing green to dark green in hand sample. Elongate disseminations of Ccp are also present along cleavage planes in albite, actinolite-tremolite, chlorite and annite-phlogopite (Fig. 21j). Where chlorite and clinozoisite-epidote crystals are both present along the margins of Ccp or as inclusions in Ccp, chlorite will form overgrowths of anhedral, platy crystals on subhedral to euhedral grains of clinozoisite-epidote (Fig. 21k, l).

To investigate whether a correlation exists between the mineral species in contact with Ccp (*i.e.* selvage) and the composition of the host rock, the average mineralogy of the selvage was estimated for each mineralized sample. Samples were then grouped into five different bulk rock compositions, and the average selvage mineralogy for each bulk composition was determined (Fig. 22). Bulk rock composition is based on modal quartz (Qtz) and K-feldspar (Kfs), where felsic rocks have a high modal Qtz + Kfs and mafic rocks have a low modal Qtz + Kfs. The two strongest associations exists between Ccp +

plagioclase (Pl) and Ccp + Qtz, which, together, are representative of Qtz + Pl grain boundary interfaces. This is demonstrated visually in Fig. 21d, where disseminated Ccp is present at the contact between granoblastic polygonal quartz and fine-grained, albitic Pl2. The positive association between Ccp and Pl + Qtz is pronounced even in Qtz-poor rocks, where Ccp is commonly localized around rare islands of Qtz in an otherwise mafic rock. At the hand sample scale, the Ccp is often deflected around mafic enclaves and layers that occur in Qtz + Pl-rich rocks (Fig. 2c).

Clinozoisite-epidote and actinolite-tremolite are the two most common hydroxysilicate phases in contact with Ccp. They are present as subhedral to euhedral crystals that are often comb-textured in Ccp, having grown outwards from a Pl-rich margin, or present as discrete inclusions in Ccp. Actinolite-tremolite crystals are zoned, exhibiting relatively Mg-rich rims and Fe-rich cores (Fig. 21i). While clinozoisite-epidote and actinolite-tremolite do texturally coexist in some samples, the prevalence of either phase appears to be related to bulk rock composition, as mafic rocks (1 – 10% Qtz + Kfs) have Ccp selvages that are richer in actinolite-tremolite, and felsic rocks have selvages richer in clinozoisite-epidote.

To investigate whether the grain size of clinozoisite-epidote crystals correlates with the grain size of Ccp, grain sizes of clinozoisite-epidote crystals in contact with Ccp were measured along their long-axes and plotted against the average measured width of the corresponding Ccp veinlet or dissemination (Fig. 23). While grain sizes of clinozoisite-epidote crystals in contact with a given sulfide dissemination or veinlet are quite variable, as shown by the large error bars, there is a broad positive trend between the average grain size of selvage clinozoisite-epidote and the width of the corresponding Ccp dissemination or veinlet.

1.8 Mineral Chemistry

1.8.1 Plagioclase mineral chemistry

Semi-quantitative analyses of plagioclase from Victor footwall rocks and the North Range transect are presented on a feldspar ternary plot (Fig. 24). In sampled Victor footwall rocks, fine-grained plagioclase neoblasts (Pl2), plagioclase laths intergrown with quartz (Pl3), and plagioclase grains in direct contact with Ccp (Pl4), are albitic in composition (An# $\leq$ 10) in rocks of all bulk compositions, including felsic (*i.e.* tonalite, granodiorite, monzogranite) and intermediate to mafic (*i.e.* diorite, quartz diorite, gabbro) rocks. In sampled rocks from the North Range transect, plagioclase ranges in composition from oligoclase (An_{20-30}) to albite.

1.8.2 Clinozoisite-epidote mineral chemistry

Quantitative analyses (n = 199) of major and minor element mineral chemistry for clinozoisite-epidote (Czo-Ep) were grouped based on their different textural populations with mineral formulae calculated based on 12.5 oxygen. Results are presented in a binary plot of Al vs Fe^{3+} (Fig. 25a), which is representative of the clinozoisite-epidote solid solution series, and as a downhole plot of average *Fe#* (*i.e.* Fe^{3+}/Fe^{3+} + Al) of selvage-type Czo-Ep overlain with total modal chalcopyrite (Ccp) (Fig. 25b). Two major groupings are identified from Figure 25a: (1) Czo-Ep in contact with Ccp is relatively Fe-rich (n = 124; 0.27 ± 0.02), regardless of the Ccp texture (*e.g.* disseminated, veinlet-style, and semi- to massive Ccp); and (2) fine-grained, disseminated Czo-Ep associated with plagioclase (*i.e.* saussuritized plagioclase) is relatively Fe-poor (n = 49; 0.199 ± 0.0457).

Clinozoisite-epidote occurring in veins and as intergrowths with chlorite (after annite-phlogopite) varies in composition, but is generally more Fe-rich than disseminated-type Czo-Ep (n = 12; 0.26 ± 0.031). As seen in Figure 25b, there is no obvious relationship between the *Fe#* and total modal Ccp and

style of Ccp, and there is no obvious correlation between the *Fe#* of disseminated-type Ep and the style or abundance of Ccp in the sample. Measurements for Mn are consistently low, averaging 0.007 *apfu.* Analyses of Cl or F are below detection limit.

1.8.3 Chlorite mineral chemistry

Quantitative analyses of major and minor element mineral chemistry for chlorite (n = 178) were grouped based on textural populations and mineral formula were calculated based on 22 oxygen. The average composition of chlorite for each of the textural populations was ripidolite. Results for chlorite are presented in an Al-Fe-Mg ternary diagram (Fig. 26a), which represents the three major octahedrally coordinated cations in the chlorite crystal structure, and as downhole plots of *Fe#* (Fe_{total}/ Fe_{total} + Mg) and Ni overlain with total modal sulfides for each sample (Fig. 26b). Two major groupings are identified: (1) chlorite in samples proximal (< 20 cm) to the massive Ccp vein is relatively Fe-rich (n = 34; *Fe#* = 0.69 ± 0.023) and Ni-rich (n = 27; 0.27 ± 0.022 *apfu*); and (2) chlorite in samples distal (> 20 cm) to a massive Ccp vein are relatively Fe-poor (n = 144; *Fe#* = 0.55 ± 0.043) and Ni-poor (n = 142; 0.13 ± 0.078 *apfu*). Furthermore, chlorite that is in contact with Ccp immediately adjacent the hanging wall and footwall contacts of the massive Ccp vein is distinctly Fe- and Ni-rich in comparison with chlorite that is contact with other textural varieties of Ccp. With increasing depth from ~1993 m (*i.e.* 6540 ft) over an interval of less than 0.5 m, the average *Fe#* of chlorite decreases from 0.70 ± 0.018 to 0.60 ± 0.013, while the average Ni concentration decreases from 0.27 ± 0.016 *apfu* to 0.09 ± 0.08 *apfu* (Fig. 26b, c). Chlorite proximal to the massive Ccp vein is similarly enriched in Mn (n = 34; 0.074 ± 0.005 *apfu*) *versus* chlorite distal to the massive Ccp vein (n = 142; 0.060 ± 0.007 *apfu*) (Fig. 26c). A decrease in *Fe#*, Ni and Mn concentration was also observed when up hole from the hanging wall side of the massive Ccp vein.

The Fe^{3+}/Fe_{total} of the chlorites, calculated assuming full site occupancy, are highly variable. The average Fe^{3+}/Fe_{total} of fine-grained chlorite in plagioclase proximal to the massive Ccp vein is 0.026 ± 0.015 (n = 8; range = 0 – 0.050), and the average Fe^{3+}/Fe_{total} of fine-grained chlorite in plagioclase distal to the massive Ccp vein is 0.021 ± 0.03 (n = 31; range = 0 – 0.135). The average Fe^{3+}/Fe_{total} of chlorite in contact with the massive Ccp vein is 0.004 ± 0.006 (n = 26; range = 0 – 0.019), and the average Fe^{3+}/Fe_{total} of chlorite in contact with Ccp disseminations and veinlets distal to the massive Ccp vein is 0.010 ± 0.010 (n = 52; range = 0 – 0.030).

Crystallization temperatures of chlorite were calculated using the geothermometric method developed by Cathelineau (1988), based on tetrahedral Al content according to the following formula:

$$T\ (^{o}C) = -61.92 + 321.98\ (Al^{IV})$$

Results are presented in Figure 26d as a downhole plot. The shape of the observed trend line in $T_{crystallizaton}$ resembles that shown by *Fe#*, Ni and Mn. Chlorite in contact with Ccp, directly adjacent the hanging wall and footwall contacts of the massive Ccp vein exhibits an average $T_{crystallizaton}$ = 367 ± 9.7 ºC (n = 26; range = 339 – 385 ºC), while chlorite in contact with Ccp disseminations and veinlets distal to the massive Ccp vein exhibit average $T_{crystallizaton}$ = 344 ± 14.5 ºC (n=52; range = 318 – 372 ºC). Fine-grained chlorite in plagioclase exhibits an average $T_{crystallizaton}$ = 342 ± 13.9 ºC (n = 34; range = 311 – 365 ºC).

1.9 Interpretation of Results

1.9.1 Textural development of quartz

Granoblastic polygonal quartz comprises over 90% of all quartz observed in rocks sampled from both the Victor footwall (Fig. 2) and locations proximal to the SIC North Range contact (location given in Figure 1b). Along with aggregates of fine-grained plagioclase neoblasts, granoblastic polygonal

quartz is among the most prominent textures observed at the thin-section scale in SIC contact-proximal rocks. Thus, an understanding of how it developed is essential to elucidating the broader paragenetic evolution of the North and East range footwall environments. The presence of granoblastic polygonal quartz in the footwall rocks of the SIC has long been recognized (Hebel 1978; Dressler 1984b; McCormick *et al.* 2002; Boast & Spray 2006; Péntek *et al.* 2011). Results from measurements of quartz grain sizes and dihedral angles from rocks collected along the North Range transect suggest that the development of polygonal grains in parent quartz was a function of proximity to the SIC footwall contact. Specifically, both the modal abundance of the new polygonal grains (normalized to total quartz) and their media grain size were observed to increase when approaching the contact from ~500 m. In the footwall to the SIC and approaching the contact along the North Range transect from ~500 m, the sequential recovery and recrystallization of strained parent quartz, observed in cross-polarized light as undulatory extinction and deformation lamellae (Fig. 6c, d, e), was observed in the following stages: (1) development of chessboard-type subgrains (Fig. 6e); (2) development of discrete anhedral subgrains and new grains, orthogonal to bands of extinction (Fig. 6f); (3) development of new, strain-reduced grains with polygonal morphologies and average dihedral angles approaching the equilibrium value of 120 º (Kruhl 2001); and (4) coarsening of the strain-reduced, polygonal grains (Fig. 6h,i).

The development and coarsening of polygonal quartz grains at the expense of strained, parent quartz likely reflects an increasing degree of thermally-enhanced recovery and recrystallization (*i.e.* annealing), driven by heat from the cooling SIC. Similar observations have been made from rocks in the contact metamorphic aureoles of the Ballachulish Igneous Complex (BIC) and Skaergaard intrusion. In the Appin Quartzite of the BIC in Scotland, dynamically recrystallized, flattened quartz grains formed during earlier Caledonian regional metamorphism were later replaced by statically recrystallized, polygonal, strain-free grains that coarsen towards the BIC contact (Buntebarth & Voll 1991; Pattison &

Harte 1997). Bufe *et al.* (2014) described the sub-solidus recrystallization of quartz within the contact metamorphic aureole of the Skaergaard intrusion, where strained quartz, defined by undulatory extinction, was replaced by strain-free grains, which preferentially nucleated at quartz-feldspar grain boundaries.

Experiments suggest that the microstructural evolution during static annealing depends on the annealing temperature, annealing time and the initial deformation microstructures (Kruhl 2001; Park *et al.* 2001; Heilbronner & Tullis 2002). For instance, Kruhl (2001) demonstrated a positive correlation between polygonal grain size and annealing temperature and time, using camphor ($C_{10}H_{16}O$) as an analogue material for quartz. Heilbronner & Tullis (2002) described the development of equant, straight-sided polygonal quartz grains at the expense of deformed quartz, characterized by undulatory extinction, during controlled annealing experiments. Transmission electron microscopy (TEM) analyses have shown that undulatory extinction in quartz is associated with a relatively high density of line defects (*i.e.* dislocations) in the quartz crystal lattice, generated during deformation (Hirth and Lothe 1982; Hirth & Tullis 1992; Passchier & Trouw 2005 and references therein). Each dislocation has an associated strain energy, stored within the distorted bonds around the dislocation (Poirier & Guillopé 1979; Hatherly & Humphries 1995). Recovery and recrystallization are driven by a reduction in the total free energy of the system; dislocations are destroyed, shortened and re-ordered into planar arrays (*i.e.* deformation lamellae), which may further reorganize into low-angle (*e.g.* <10 º) subgrain boundaries. Subgrains may become new grains through the development of high-angle grain boundaries (Heilbronner & Tullis 2002; Humphreys & Hatherly 2004; Passchier & Trouw 2005 and references therein). Straightening of quartz grain boundaries and grain coarsening (*i.e.* grain boundary area reduction), observed approaching the contact from ~500 m (Fig. 6j, k, l), was likely driven by a reduction of total interfacial energy, generated due to a lattice misfit across grain boundaries (Evans *et al.* 2001; Humphreys & Hatherly

2004 and references therein). With increasing annealing temperatures approaching the cooling SIC, the formation and coarsening of new, strain-free quartz grains at the expense of plastically deformed parent quartz may have been accommodated by thermally-activated mechanisms such as diffusion creep and dislocation climb (Humphreys & Hatherly 2004; Passchier & Trouw 2005).

The timing of quartz deformation (*i.e.* generation of crystal defects) relative to the 1.85 Ga Sudbury Event can be constrained by comparing the new, strain-free polygonal grains proximal to the SIC contact with quartz from SIC North Range contact distal and medial rocks (Fig. 1b). Quartz crystals in rocks distal to the SIC North Range contact exhibit recovery and recrystallization microstructures that are texturally distinct from those observed in SIC contact proximal rocks. In distal rocks, quartz aggregates are characterized by a greater prevalence of grains with interlobate margins *versus* straight-sided margins (Fig. 6a and Fig. 8a). This suggests that the recrystallization textures observed in distal quartz developed under different conditions than quartz proximal to the contact, and that deformation and recrystallization of distal quartz was unrelated to the Sudbury Event. As the rocks of the Levack Gneiss Complex were subjected to at least two regional high-grade metamorphic events prior to the formation of the SIC (Krogh *et al.* 1984; James *et al.* 1991; Meldrum *et al.* 1996), it is likely that quartz had been subjected to some degree of pre-SIC deformation and recrystallization. As observed in both SIC distal and medial rocks, parent quartz grains that are relatively devoid of polygonal grains have irregular cuspate-lobate margins when in contact with plagioclase, further indicative of recrystallization unrelated to SIC-related thermal annealing. Similar lobate quartz-feldspar grain boundaries, observed in granulite facies rocks of the Sierra de Valle Fértil, Argentina, were interpreted as having resulted from dynamic recrystallization of the grain boundaries (Delpino *et al.* 2008). In a study of upper amphibolite facies gneisses of the Grenville Province, Gower *et al.* (1992) suggested that cuspate phase boundary

microstructures observed along quartz-feldspar grain boundaries resulted from solid-state diffusional creep during dynamic recrystallization.

In Victor footwall rocks, textures indicative of deformation, recovery and recrystallization were observed to locally overprint granoblastic polygonal quartz, suggesting that competing processes of deformation and recrystallization (*i.e.* dynamic recrystallization) were occurring in the Victor footwall environment syn- to post-emplacement of the SIC. Flattened quartz with undulatory extinction and deformation lamellae were observed, coinciding with new, very fine-grained bulging microstructures and subgrains occurring preferentially along the boundaries of pre-existing recrystallized granoblastic quartz grains, producing core-and-mantle structures (Fig. 17f, g, h). These microstructures appear to be consistent with bulging (BLG) recrystallization, which corresponds to Regime 1 dislocation creep in quartz and relatively low temperatures and/or fast strain rates (Hirth & Tullis 1992; Stipp *et al.* 2002; Heilbronner & Tullis 2002; Passchier & Trouw 2005). Textural evidence suggests that the deformation and corresponding BLG recrystallization were relatively localized, short-lived, and may have only developed at a point when the SIC had cooled sufficiently, since: (1) the strained, flattened quartz grains show relatively low degrees of recovery and recrystallization despite being relatively close to the SIC contact (*i.e.* intra-grain bulges dominate over subgrains and new, strain-free grains); and (2) textures indicative of BLG recrystallization occur only locally at the thin-section scale. In addition to temperature, the behavior of quartz deformation is influenced by several other unknown variables, including but not limited to strain rate, the presence of pore fluids, solute and impurity chemistry, chemical fugacity of trace and major elements, pore size and number, and the presence of solid secondary phases (Tullis & Yund 1989; Evans *et al.* 2001). Thus, the range of possible temperatures for the BLG recrystallization is uncertain. However, in a comprehensive review of deformation structures in

quartz, Passchier & Trouw (2005) reported that BLG recrystallization is the dominant recrystallization mechanism in quartz at a *T* range of 300 – 400 ºC.

1.9.2 Textural development of plagioclase

Three genetic origins have been proposed to explain the origin of the plagioclase neoblasts proximal to the SIC North and East range footwall contacts: (1) annealing of strained plagioclase; (2) crystallization from a melt; and (3) recrystallization of a diaplectic plagioclase glass. The existence of fine-grained recrystallized plagioclase aggregates proximal to the SIC footwall contact has been documented by multiple authors (Hebil 1978; Dressler 1984b; McCormick *et al.* 2002; Boast & Spray 2006; Lafrance *et al.* 2008; Kontak *et al.* 2015). In the Strathcona Embayment on the North Range of the SIC, McCormick *et al.* (2002) characterized textural variations of the footwall breccia, a locally melted, contact-metamorphosed, polymict, matrix-supported transitional unit between the SIC and underlying footwall rocks. The authors described the presence of fine-grained, prismatic, tabular and polygonal mosaics of plagioclase feldspar coexisting with polygonal quartz and optically continuous, oikocrystic quartz. The interpretation was that grain coarsening and the transition from polygonal to idiomorphic plagioclase grains towards the contact was driven by thermal metamorphism and a reduction in surface free energy. Deeper into the North Range footwall environment, Dressler (1984b) suggested the possibility that the fine-grained, decussate-textured plagioclase formed following the recrystallization of a diaplectic glass. Boast & Spray (2006) described the presence of feldspar neoblasts within 1 km of the contact, which were interpreted as having replaced shocked feldspar grains, and which coarsen and increase in abundance towards the contact.

In the core of the central uplift of the Vredefort impact structure, Gibson & Reimold (2005) favored the recrystallization of diaplectic feldspar glass to explain the development of both fine-grained

plagioclase crystals and medium-grained, prismatic, Carlsbad-twinned K-feldspar grains enclosed in perthitic, pre-impact K-feldspar. The latter is found with a texture similar to that observed in North and East range SIC footwall rocks (Fig. 13a, f). Aggregates of granoblastic quartz, a texture attributed to post-shock annealing and similar to that observed in the footwall to the SIC, was also documented in the Vredefort rocks.

Results from observations and measurements of plagioclase in rocks collected along the North Range transect suggest that the development of neoblasts in plagioclase is dependent on proximity to the SIC footwall contact. Specifically, both the modal abundance of total plagioclase neoblasts (normalized to total plagioclase) and the average neoblast grain size were observed to increase when approaching the contact from ~500 m (Fig. 10), mirroring trends observed in the modal abundance and grain size of annealed quartz in the same rocks. The positive correlation between the modal abundance and grain size of the plagioclase neoblasts and proximity to the SIC contact supports the interpretation that the plagioclase neoblasts developed as a result of the thermal-annealing of strained, primary Archean plagioclase grains, driven by heat from the cooling SIC. A lower temperature limit for the plastic behavior of plagioclase is 450 – 600 ºC, below which feldspar deforms brittlely (Passchier & Trouw 2005 and references therein). A strong positive correlation between the grain diameter of annealed plagioclase grains and *T* has previously been described by Kruhl (2001).

Textures from photomicrographs demonstrate a strong spatial association between the fine-grained plagioclase neoblasts (Pl2) and the grain boundaries of coarser-grained parent plagioclase grains (Fig. 9e, f), where microstructures indicative of grain boundary bulging and enhanced grain boundary mobility frequently occur (Fig. 9d, g, h, i). These microstructures are most prevalent in SIC contact proximal rocks (Fig. 1). Similar textures were observed in K-feldspar. Neoblasts of K-feldspar, present in Victor footwall and SIC North Range contact-proximal samples but absent in contact-medial and

distal samples, were also observed to develop preferentially along grain boundaries showing evidence for bulging recrystallization (Fig. 13a), and were observed to be spatially associated with aggregates of plagioclase neoblasts (Fig. 13c). In rocks sampled further than ~500 m from the SIC contact, plagioclase neoblasts are rare, and parent plagioclase grains are frequently characterized by microstructures indicative of accumulated strain, including undulatory extinction, bent polysynthetic twins, rare wedge-shaped glide twins, micro-offsets and sharp kink bands that displace polysynthetic twins (Fig. 9a, b, c) (Vernon 1975; Ji & Mainprice 1990; Lafrance *et al.* 1996; Kruse *et al.* 2001). Similar micro-deformational features in K-feldspar were not observed. However, samples containing parent alkali-feldspar grains were scarce, in contrast to the plagioclase- and quartz-rich rocks collected.

As occurs in quartz, the driving force for the development and coarsening of strain-free neoblasts is a reduction in the Gibbs free energy of the system, stored as strain energy in the distorted bonds around dislocations and as interfacial free energy (Poirier & Guillopé 1979; Humphreys & Hatherly 2004). In its earliest stages, annealing of strained plagioclase appears to have been accommodated through grain boundary bulging, involving the nucleation and growth of new strain-free neoblasts along grain boundaries (forming core-and-mantle structures) and along narrow high strain zones, such as kink bands, in the cores of primary plagioclase grains (Fig. 9c, f) (Ji & Mainprice 1990; Lafrance *et al.* 1996; Kruse *et al.* 2001). Intra-grain bulges along a given parent plagioclase grain boundary were consistently observed to replace a common grain (Fig. 9d, i), likely reflecting the preferential replacement of the grain with the higher relative dislocation density (Passchier & Trouw 2005). Approaching the SIC contact, likely coinciding with an increase in heat, progressive subgrain rotation and enhanced grain boundary mobility would be predicted to be enhanced (Lafrance *et al.* 1996). This would be consistent with (1) the observation of an increase in the modal abundance of plagioclase neoblasts with a relatively uniform size and shape approaching the contact (Fig. 10a), and (2) the observation of aggregates of

randomly oriented plagioclase neoblasts which have swept across entire primary grains, often mimicking the parent plagioclase grain margin (Fig. 19b). The lack of a shape preferred orientation (SPO) shown by the neoblasts further suggests that thermally-mediated recrystallization and recovery processes were dominant over the influence of differential stress.

The observation of frequent prismatic, Carlsbad and albite-Carlsbad twinned plagioclase neoblasts in North Range SIC contact-proximal rocks (>90% of measured grains) is inconsistent with observations of plagioclase twins made by Gorai (1951) in a study of plagioclase twin laws in metamorphic and igneous rocks. Gorai (1951) noted that plagioclase grains twinned on the Carlsbad and albite-Carlsbad laws occurred frequently in igneous rocks, but were comparatively rare in metamorphic rocks (*e.g.* amphibolite facies gneisses and hornfels). Carlsbad and albite-Carlsbad twins are examples of growth twins, developing due to an 'accident' during crystal growth, and as a means to satisfy unfulfilled bonds and achieve a lower free energy state. If atoms or atomic groups begin forming a growth layer with a different orientation than the pre-existing crystal, a growth twin may result (Buerger 1945; Smith 1974; Vernon 2003). While growth twins generally occur due to nucleation error in a liquid under conditions of supersaturation (*i.e.* igneous plagioclase), it has been well-documented that growth twins in plagioclase can occur due to nucleation error in a solid medium (Gorai 1951; Turner 1951; Vernon 1965; Vernon 2003). In a study of feldspar twin laws observed in lunar highlands anorthosites collected as part of the Apollo 15, 16 and 17 missions, Dowty *et al.* (1974) described the occurrence of frequent Carlsbad and Carlsbad-albite twins in recrystallized, granoblastic plagioclase, in contrast with the observations of Gorai (1951) and Turner (1951) on terrestrial metamorphic plagioclase. The authors proposed that on the lunar surface, the relatively high rates of recrystallization and temperature change associated with impact events may have increased the probability of fortuitous atomic encounters in a solid medium, thus facilitating the development of growth twins in plagioclase. With respect to the

current study, this may suggest that the high frequency of prismatic, Carlsbad-twinned plagioclase neoblasts reflects a relatively high rate of temperature change. The lower frequency of twins observed in the granoblastic-textured plagioclase neoblasts (*i.e.* grains with polygonal to sub-equant habits and average dihedral angles of ~120 º) (Fig. 19c) relative to the comparatively immature, prismatic neoblasts (Fig. 9d) may reflect a tendency to remove twin boundaries through continued annealing.

As observed in the strain-reduced recrystallized quartz, plagioclase neoblasts were observed to coarsen towards the SIC contact along the North Range transect (Fig. 10b). This is evidence that would suggest that grain boundary area reduction occurred in both plagioclase neoblasts and quartz grains, and was thermally-mediated by heat from the cooling SIC. In previous studies, it has been suggested that chemical potential differences are a possible driving force for recover processes in plagioclase (Vernon 1975; Rosenberg & Stünitz 2003; Mukai *et al.* 2014). This would not be consistent with measurements of plagioclase compositions from parent grains and neoblasts, in which differences in anorthite contents were negligible. Furthermore, neoblasts could not be distinguished visually from their parent grain using BSE imaging, due to similarities in their compositions.

1.9.3 Evidence for partial melting of quartz and feldspar

The potential for the development of partial melts in the footwall rocks to the Victor deposit may be observed in textural intergrowths of quartz-K-feldspar and quartz-plagioclase. Granophyric intergrowths of quartz and K-feldspar (Fig. 17d), referred to as footwall granophyres (FWGR) by Molnar *et al.* (2001) and Péntek *et al.* (2009; 2011), occur locally throughout Victor footwall rocks to distances at least ~80 m from the inferred footwall contact. Patches and veins of optically continuous, oikocrystic quartz intergrown with comb-textured, euhedral plagioclase laths, are similar to those described by McKormick *et al.* (2002) and Péntek *et al.* (2009, 2011) (Fig. 16e, f). Quartz-plagioclase lath

intergrowths are common in relatively quartz-poor rocks (*e.g.* diorites and quartz diorites), but are less common in quartz-rich rocks (*e.g.* tonalites and granodiorites). In quartz-rich rocks, isolated grains of sub-equant quartz with interstitial plagioclase seams locally occur around the margins of granoblastic polygonal quartz aggregates (Fig. 17a, b, c). Quartz-plagioclase lath intergrowths were observed to locally transition into quartz-plagioclase seam intergrowths (Fig. 17e), providing evidence that the two intergrowths are spatially related. In both types of intergrowth, quartz and plagioclase show lower degrees of recovery and recrystallization relative to co-existing granoblastic-polygonal quartz and fine-grained, log-jam-textured to polygonal plagioclase, despite exhibiting evidence of accumulated strain (*e.g*. undulatory extinction in quartz). Therefore, it is possible that the intergrowths either: (1) crystallized pre- to syn-development of the SIC, were relatively un-deformed throughout SIC-related thermal annealing of quartz and plagioclase, and the undulatory extinction exhibited by the oikocrystic quartz was due to later plastic deformation; or (2) crystallized post-peak of SIC-related thermal annealing of quartz and plagioclase, and later plastic deformation produced undulatory extinction in quartz. A lower relative time constraint on the crystallization of the intergrowths coincides with the development of fine-grained secondary features (*e.g*. microporosity + epidote- and chlorite-group minerals) in the seam-textured and lath-textured plagioclase (An_{0-10}). The original anorthite content of plagioclase in both intergrowth types prior to development of the secondary features is unknown.

Results from measurements of quartz-quartz-plagioclase dihedral angles (Fig. 18) suggest that the quartz-plagioclase seam textures may be indicative of crystallization of quartz-plagioclase melts. In a study of melt-solid dihedral angles (*i.e.* wetting angles) between solid quartz and interstitial rhyolite glass as an analogue for a solidified melt, Holness (2006) determined that the median quartz-melt dihedral angle is ~18 ± 9 º. This angle is consistent with dihedral angles of 22-23 º for synthetic quartz-granitic melt determined by Laporte *et al.* (1997). In the present study, randomly measured plagioclase-

quartz-quartz dihedral angles from a representative Victor footwall sample (see inset in Fig. 18) peak at ~40 º with a median value of 65 º. Both of these values are significantly lower than the ideal quartz-quartz-quartz dihedral angle of 120 º observed in many of the granoblastic polygonal quartz aggregates, and the equilibrium plagioclase-quartz-quartz value of 110 ºC measured in high-grade metamorphic rocks from Broken Hill, Australia (Vernon 1968). As such, the angles observed in the Victor sample are more similar to the experimentally determined melt-quartz median values, and would therefore suggest that the interstitial plagioclase originated as a melt. In the Appin Quartzite within the contact aureole of the Ballachulish Igneous Complex, Clemens & Holness (2000) noted similar plagioclase-quartz-quartz dihedral angles (peak at 40-60 º) to those observed in the Victor footwall samples, which they believed to be characteristic of wetting angles. Rossenberg & Riller (2000) documented even lower median feldspar-quartz-quartz dihedral angles (~27 º) from granites of the Murray Pluton along the SIC South Range. In the Victor sample, the median plagioclase-quartz-quartz dihedral angle is low relative to the equilibrium angle of ~110 º (Vernon 1968), but high relative to the quartz-melt dihedral of ~18 ± 9 º of Holness (2006). This might reflect some degree of sub-solidus equilibration of the quartz-plagioclase dihedral angle towards ~110 º, driven by a reduction in interfacial energy and accommodated by relatively slow grain boundary diffusion (Vernon 1968; Holness & Sawyer 2008).

Cathodoluminence (CL) images of the quartz-plagioclase seam intergrowths show that the quartz is characterized by bright blue rims and dark, weakly luminescent cores (Fig. 17). While the specific CL activators are unknown, this texture may suggest that there was a difference in the growth histories of the core and rim. In a CL study of plagioclase-bearing quartzite from within the contact aureole of the Duluth Igneous Complex, Holness (2010) described a similar texture to that observed in the Victor footwall rocks, in which bright, luminescent rims were interpreted as being the quartz component of a melt that crystallized on relatively cool, restitic quartz grains, represented by dark, weakly luminescent

quartz cores. In their study of quartz + interstitial feldspar microstructures of the Murray granite pluton of the SIC South Range footwall, Rossenberg & Riller (2000) likewise argued that the quartz component of a melt likely precipitated on existing quartz grains, and the feldspar melt component nucleated as interstitial grains due to insufficient feldspar nucleation sites.

It is possible that the availability of suitable nucleation sites, influenced by bulk rock composition (*i.e.* % of total quartz), played a role dictating which of the two quartz-plagioclase textures developed in the Victor footwall rocks, given the observed correlation of intergrowth-type to % of total quartz. Intergrowths of anhedral, oikocrystic quartz and euhedral plagioclase laths were rarely observed in rocks with greater than 23% modal quartz (QAP normalized), but were observed as the dominant quartz variety in quartz-poor rocks (*e.g.* diorites and quartz-diorites). This may suggest that in quartz-poor rocks, the relatively greater availability of plagioclase nucleation sites favored the crystallization of euhedral plagioclase crystals and interstitial, oikocrystic quartz. Conversely, in quartz-rich rocks, the greater availability of quartz nucleation sites may have favored the crystallization of the quartz melt component on pre-existing quartz grains, while the plagioclase component crystallized as interstitial grains.

The availability of water during the cotectic melting of quartz and plagioclase can have a strong influence on the $T_{melting}$, as can the anorthite content of plagioclase (Johannes & Holtz 1996). The degree of involvement of water in the melting of quartz and plagioclase in the Victor footwall rocks is unknown. For instance, there is no textural evidence indicating quartz and plagioclase crystals contained pore fluids at the time of melting, nor is there evidence to suggest that the dehydration of coexisting annite-phlogopite had contributed to the melting reactions. Furthermore, the timing of crystallization of the secondary hydrous phases (chlorite- and epidote-group minerals, actinolite-tremolite) relative to the intergrowth textures cannot be established with confidence. Therefore, it is unclear whether dehydration

of hydrous secondary silicate phases contributed to the cotectic melting of quartz + plagioclase. In the water-saturated tonalite system (Qtz + Ab + An + H_2O) at pressures of 2 kbar, which is the best available pressure approximation for the estimated 5 km depth of erosion (~1.67 kbar) of the SIC (Dressler 1984b), the first degree of melting between quartz and plagioclase would be predicted to occur at temperatures of 753-772 ºC for a plagioclase composition of An_{30} (Johannes & Holtz 1996). This composition best approximates the highest anorthite content observed in least-altered plagioclase from North Range footwall rocks (Fig. 24). With decreasing activity of H_2O, the $T_{melting}$ would be expected to be higher (Johannes & Holtz 1996). In an extensive study of partial melting in the SIC North and East range footwall environments, Péntek *et al.* (2011) estimated that temperatures may have reached 850 – 900 ºC for distances up to 200 m from the contact in the Frost Lake area of the SIC East Range.

1.9.4 Temporal and spatial relationships

The following subsections discuss the key temporal and spatial relationships observed between mineral phases in the North and East range footwall rocks, which were used to reconstruct a paragenetic sequence (Fig. 4) and elucidate the geological processes that were active within the North and East range footwall environments.

1.9.4.1 Development of secondary features in plagioclase and K-feldspar

The timing of development of fine-grained secondary mineralogy relative to the development of thermally-mediated recrystallization and recovery microstructures in plagioclase is constrained by several key textural relationships: (1) the preferential replacement of least-altered plagioclase (An_{20-30}) by albite along the grain boundaries of Pl2 neoblasts indicates that the development of albite post-dates

the SIC-related thermal annealing of strained plagioclase (Fig. 11d); and (2) the development of fine-grained epidote- and chlorite-group minerals, K-feldspar (Kfs4), muscovite, titanite, and actinolite-tremolite along the grain boundaries of Pl2 neoblasts indicates that these phases likewise developed post-annealing of strained plagioclase (Fig. 11d, e, f, g). Fine-grained chlorite-group minerals were also observed along grain boundaries and triple junctions in granoblastic polygonal quartz (Fig. 2a), indicating that the chlorite-group minerals developed post-quartz annealing.

The observation of porous albite that has replaced non-porous, least-altered plagioclase (An_{20-30}), suggests that the porosity is a product of the albitization (Fig. 11d, h). Furthermore, the observed positive trend in the total concentrations of porosity in plagioclase and fine-grained epidote-group minerals in plagioclase suggests that the albitization of plagioclase was contemporaneous with the development of fine-grained epidote-group minerals. Together, these relationships suggest that the peak period of plagioclase annealing was followed by the preferential replacement of least-altered plagioclase (An_{20-30}) by porous albite and concomitant crystallization of fine-grained clinozoisite-epidote, which may have been concomitant with the development of fine-grained chlorite, muscovite and titanite in plagioclase. The relationship between porosity in plagioclase and fine-grained chlorite-group minerals, K-feldspar (Kfs4), muscovite, actinolite-tremolite, and titanite is less clear, as these phases were often absent or in smaller concentrations than fine-grained epidote-group minerals.

In K-feldspar, the development of irregularly-shaped, porous domains of albite along the margins of K-feldspar neoblasts indicates that the development of patch perthite post-dates the development of K-feldspar neoblasts. As the development of neoblasts in primary K-feldspar crystals proximal to the SIC contact is interpreted as having likely been influenced by heat from the cooling SIC, this may suggest that the footwall rocks had cooled sufficiently to promote the *T*-driven coarsening of perthitic exsolution lamellae (Smith & Brown 1988). The observation of fine-grained epidote-group ± hematite crystals

localized within the albitic domains of the patch perthite indicates that the Ca, Al, Si, Fe^{3+} and OH^- ions required to form the epidote-group minerals were either released during the breakdown of K-feldspar, or derived from an extrinsic source. The presence of microporosity in patch perthite has previously been interpreted as evidence for a fluid-mediated origin, involving the dissolution of cryptoperthite, precipitation of patch perthite and loss of material to a fluid phase (Walker *et al.* 1995; Lee & Parsons 1997; Parsons and Lee 2009; Norberg *et al.* 2011, 2013). Fine-grained disseminated hematite crystals in porous patch perthite have likewise been argued to have resulted from fluid-rock interaction, rather than as the product of solid-state exsolution of Fe^{3+} from K-feldspar (Putnis *et al.* 2006).

1.9.4.2 Development of accessory mafic phases

Observations and estimates of modal abundances suggest that the development of fine-grained secondary features in plagioclase is positively correlated with the replacement of annite-phlogopite (Ann-Phl) by chlorite- and epidote-group minerals (Fig. 16). Annite-phlogopite crystals in both North and East range footwall rocks commonly exhibit a sagenitic texture, where crystals of rutile + ilmenite + titanite are elongate within the (001) plane of Ann-Phl, and which conform to the pseudohexagonal symmetry of the biotite-group minerals (Shau *et al.* 1991). The observation of titanite lamellae forming the same triangular patterns in chlorite and clinozoisite-epidote as observed in sagenitic Ann-Phl suggests that Ann-Phl was indeed replaced to varying degrees by chlorite and clinozoisite-epidote (Fig. 14g-i), and that the titanite crystals likely reflect an alteration product of the rutile and ilmenite (Fig. 14j). Along the North Range transect, samples in which the replacement of an Ann-Phl by chlorite and clinozoisite-epidote was observed to be well-developed, were also observed to exhibit relatively high degrees of plagioclase alteration, defined as the modal abundance of fine-grained epidote- and chlorite-group minerals ± muscovite ± titanite ± actinolite-tremolite in plagioclase. Grains of clinozoisite-epidote

after Ann-Phl were also observed to be physically connected to fine-grained clinozoisite-epidote crystals in the surrounding plagioclase (An_{0-10}), suggesting that the two populations of epidote-group minerals are coeval (Fig. 14i). A physical connection between two textural populations of epidote-group minerals was also observed with respect to monazite, where fine-grained epidote-group minerals in the surrounding plagioclase (An_{0-10}) are physically connected to the allanite overgrowths of monazite and apatite.

The timing of Ti exsolution in Ann-Phl and development of rutile needles relative to the formation of the SIC cannot be inferred from mineralogical relationships. Octahedral Ti solubility in biotite is considered to be a function of temperature, pressure, biotite crystal chemistry and coexisting mineral assemblages (Henry & Guidotti 2002 and references therein). For instance, Patiño Douce (1993) noted a non-linear positive relationship between increasing temperature and Ti solubility, and a negative relationship between increasing pressure and Ti solubility. As sagenitic Ann-Phl was observed in samples distal to the SIC contact, as well as proximal to the SIC contact, it is possible that Ti exsolution in Ann-Phl occurred prior to the development of the SIC during retrograde amphibolite metamorphism (James *et al.* 1992; Roussel *et al.* 1997).

The presence of titanite rims on ilmenite + rutile cores is ubiquitous within Victor footwall rocks and was observed in varying degrees in North Range footwall rocks. This replacement was observed where ilmenite occurs as isolated grains, as sagenitic-textured lamellae in Ann-Phl, chlorite and clinozoisite-epidote, and as trellis-lamellae in magnetite. While precise chemical compositions of the coexisting titanite and ilmenite were not ascertained, the primary chemical changes in the replacement of ilmenite by titanite can be assumed to be the addition of Ca + Si, and a loss of Fe. The replacement is favored by conditions of increasing fO_2 and fH_2O, and decreasing pressure and temperature (Xirouchakis & Lindsley 1998; Xirouchakis *et al.* 2001; Harlov *et al*. 2006; Pearce & Wheeler 2014; Angiboust &

Harlov 2017). Xirouchakis *et al.* (2001b) determined that at temperatures less than 650 ºC and at relatively oxidizing conditions (*i.e.* <3 log fO_2 units above FMQ), titanite and actinolite can coexist with two oxides and pyroxene, while increasing the fH_2O with constant fO_2 would also stabilize titanite + actinolite. Titanite and actinolite-tremolite were observed to coexist in both North Range and Victor footwall rocks. The relative timing of the formation of titanite at the expense of ilmenite ± rutile is uncertain. The formation of titanite at the expense of ilmenite has been shown to occur at relatively high pressures and temperatures associated with retrogress or exhumation of high-grade metamorphic rocks (P < 16 kbar and T < 750ºC, Mohammad & Maekawa 2008; P < 10 kbar and T < 630ºC, Pearce & Wheeler 2014; P = 7 – 16 kbar and T = 450 – 650ºC, Angiboust & Harlov 2017). Therefore, it is possible that the titanite formed during pre-SIC retrograde amphibolite facies metamorphism (James *et al.* 1992; Roussel *et al.* 1997). Alternatively, the development of titanite may have been concurrent with the replacement of least-altered plagioclase (An_{20-30}) by albite, as titanite rims on ilmenite cores were observed to be relatively coarser-grained when surrounded by albite than when surrounded by relatively least-altered plagioclase (An_{20-30}). The breakdown of the anorthite component of plagioclase (An_{20-30}) may have contributed some of the Ca + Si necessary for the development of titanite. The release of Fe during ilmenite breakdown may have facilitated the development of chlorite + clinozoisite-epidote films along the interface between the titanite rim and the surrounding plagioclase groundmass.

1.9.4.3 Temporal and spatial relationships related to chalcopyrite mineralization

A distinct textural assemblage of albite + epidote-group + chlorite-group + actinolite-tremolite ± titanite occurs directly in contact with or adjacent to chalcopyrite (± pyrrhotite, pentlandite, millerite and pyrite) in Victor footwall rocks. This assemblage of secondary silicates was observed along the margins of or as inclusions in all textural varieties of chalcopyrite (*e.g.* disseminated, veinlet and massive vein).

The following textural evidence suggests that the secondary silicate assemblage in contact with chalcopyrite likely developed pre-chalcopyrite emplacement: (1) subhedral to euhedral silicate crystals with straight, sharp crystal faces are entrained in or surrounded by interstitial chalcopyrite (Figs. 2f, 21d, g, h, i, l); (2) silicate crystals in chalcopyrite are commonly comb-textured, evidence of open-spaced growth (Figs. 2f, 21g, i); (3) lamellae of chalcopyrite ± pyrrhotite were observed parallel to the cleavage planes of actinolite-tremolite, chlorite and albite, suggesting infiltration of a sulfide-rich fluid or melt occurred along the cleavage planes of pre-existing silicate crystals (Figs.19d, 21h, j); (4) silicate crystals are locally embayed along their contacts with chalcopyrite, suggesting the crystals were either modified prior to sulfide emplacement or during sulfide emplacement (Fig. 21l); (5) euhedral actinolite-tremolite crystals lining the margins of chalcopyrite were observed to be bent and/or rotated, which may be indicative of modification upon emplacement of a chalcopyrite melt or fluid (Figs. 2f, 21i). Kontak *et al.* (2012) described a similar texture, where rotated actinolite crystals were observed along the margin of a chalcopyrite vein; and (6) grain sizes of epidote-group minerals are positively correlated with the size of the corresponding chalcopyrite vein or dissemination, suggesting that at least part of the volume occupied by chalcopyrite was previously open space in which epidote-group crystals grew (Fig. 23).

The temporal relationship between chalcopyrite and chlorite-group minerals is less clear. Chlorite-group minerals were observed as both anhedral to subhedral grains when in contact chalcopyrite and as inclusions in chalcopyrite. The latter texture suggests that chlorite had already crystallized prior to becoming entrained in chalcopyrite. Chlorite-group minerals were frequently observed as anhedral overgrowths on sub- to euhedral grains of clinozoisite-epidote (Fig. 21k, l), indicating that the chlorite is likely paragenetically later than the clinozoisite-epidote.

Chalcopyrite and its associated silicate-selvage were observed to occur preferentially along the interfaces between aggregates of granoblastic polygonal quartz and aggregates of fine-grained

plagioclase neoblasts, in both quartz-rich (*e.g.* tonalites, monzogranites) and quartz-poor (*e.g.* quartz-diorites) rocks (Figs. 21d, 22). The replacement of plagioclase (An_{20-30}) by porous albite and concomitant development of fine-grained epidote-group minerals was also observed to occur preferentially along quartz-plagioclase interfaces (Fig. 11c). In isolation, this does not necessarily imply that that development of chalcopyrite was spatially related to the replacement of plagioclase by porous albite and epidote-group minerals. However, this does suggest that the quartz-plagioclase interfaces represented pre-existing grain-scale structural weaknesses that facilitated the development of both chalcopyrite and the secondary silicate assemblage that preceded it.

No textural evidence was observed to indicate that the chalcopyrite was subjected to the same stress(es) responsible for the generation of micro-deformational features observed in quartz (Fig. 17f, g). For instance, in samples where chalcopyrite and strained, flattened quartz grains coexist, chalcopyrite was not observed to be elongated parallel to the shape preferred orientation (SPO) of the flattened quartz. Rather, chalcopyrite veinlets were observed to be oriented at oblique angles to the flattened quartz grains.

1.9.4.4 Modification of monazite

Crystals of monazite in the Victor footwall were observed to exhibit varying degrees of neoblast development, similar to the development of recrystallized grains observed in quartz. The replacement of monazite by apatite along monazite neoblast boundaries and subsequent overgrowth by allanite indicates that monazite recrystallization pre-dates apatite and allanite development (Fig.20). Allanite grains rimming monazite and apatite were observed to be physically connected with REE-depleted epidote-group minerals in the surrounding plagioclase (An_{0-10}) aggregates (Fig. 20), suggesting that the allanite and fine-grained epidote-group minerals in plagioclase (An_{0-10}) may be coeval. Apatite which has

replaced monazite within the interior of the monazite grain was observed to occupy less volume than was likely occupied by parent monazite. This additional space was subsequently filled by allanite, producing an allanite overgrowth of apatite (Fig. 20i). The difference in space occupied by parent monazite and product apatite is inconsistent with the expected change in molar volume during the replacement of hypothetical monazite-(Ce) by apatite, calculated using the following formula:

$$\%\Delta V_m = \frac{\frac{M_{Ap}}{\rho_{Ap}} - \frac{M_{Mnz}}{\rho_{Mnz}}}{\frac{M_{Mnz}}{\rho_{Mnz}}} \times 100$$

Where M is the molecular weight and ρ is the density of each respective phase. Using average values of M = 240.21 g/mol and ρ = 5.15 g/cm^3 for monazite-(Ce) and M = 509.12 g/mol and ρ = 3.19 g/cm^3 for apatite, as the precise chemistries of the monazite and apatite are unknown, a molar volume gain of ~242% is predicted following the replacement of monazite-(Ce) by apatite. The increase in molar volume would be expected to fill the available space in the monazite grain. This suggests that there was a mass loss, coinciding with an inflow in Ca ions during the replacement of monazite by apatite. A similar process has been described with respect to the replacement of leucite by analcime (Putnis *et al.* 2007). The authors observed the development of porosity in product analcime, despite analcime having a ~10% greater molar volume than leucite. The interpretation was that the replacement occurred through a fluid-mediated, interface coupled dissolution-precipitation process, during which more material was dissolved than was precipitated. The ubiquitous presence of allanite as an overgrowth of apatite within the interior of the monazite grain indicates that there was a preferential inflow of Ca, Si, Al, Fe^{3+} and OH^- ions along monazite neoblast boundaries, and is evidence for fluid-mediated mass transport or solid-state diffusion.

In the current study, an inverse trend was observed between the percentage of neoblasts in monazite and the standard deviations of the average dihedral angle between neoblasts and the average neoblast size (Fig. 20c, d). The development of uniform neoblasts with dihedral angles approaching 120 º may reflect a greater degree of recrystallization and recovery. The development of new grains (*i.e.* neoblasts) in monazite has been documented in the rocks of Sandmata Granulite Complex, India (Erickson *et al.* 2015). The authors interpreted the neoblast textures as having resulted from the replacement of high-strain domains, generated during tectonic deformation, by new, strain-free grains through grain boundary migration, driven by a reduction in accumulated strain energy. If the recrystallization of monazite was concomitant with the development of new grains in quartz, plagioclase and K-feldspar, this may provide further evidence that the development of fine-grained epidote-group minerals post-dates SIC-related thermal annealing. However, sampling of additional monazites farther from the SIC contact would be needed to compare and contrast with the neoblast-rich SIC contact-proximal monazites. This might enable the identification of micro-deformational features and help to determine whether the monazite recrystallization was indeed a function of proximity to the SIC contact

1.9.5 The role of plagioclase dissolution in the development of chalcopyrite mineralization

The following evidence supports the interpretation that the replacement of plagioclase (An_{20-30}) by albite in rocks from the Victor footwall and the North Range transect was fluid-mediated: (1) the replacement is observed to be concomitant with the development of porosity in product albite, in excess of the amount of porosity predicted to be generated due to a pure molar volume loss (Fig. 11d, h); and (2) the replacement was observed to be concomitant with the development of hydrous secondary phase, including epidote- and chlorite-group minerals, actinolite-tremolite, muscovite, and titanite (Fig. 11a, b, h), suggesting that water was present. The total concentration of porosity in albite within both North and

East range footwall rocks was frequently 2% and up to 4% (Fig. 12). This value is inconsistent with the expected percentage change in molar volume from parent oligoclase to product albite. Using average values of M = 265.42 g/mol and ρ = 2.65 g/cm^3 for oligoclase and M = 263.02 g/mol and ρ = 2.62 g/cm^3 for albite, as measured values for M and ρ for each phase are unknown, a molar volume gain ~1% is predicted following the replacement of oligoclase by albite. During the experimental replacement of oligoclase by albite in the presence of an aqueous sodium silicate solution, Hovelmann *et al.* (2009) predicted a molar volume loss of ~1% following the replacement, which was inconsistent with the observed concentration of porosity in product albite. A possible explanation for the excess porosity over the predicted amount is that material was transferred to a different phase or removed by a fluid. This assertion was shared by Hovelmann *et al* (2009), who concluded that the amount of dissolving oligoclase exceeded the amount of precipitating albite, as the anorthite component was more soluble than the albite component in the presence of an aqueous sodium silicate solution. In the current study, the replacement of non-porous, least-altered plagioclase (An_{20-30}) by porous albite was observed to preserve the external morphology of the parent plagioclase neoblast, indicating that the replacement was likely pseudomorphic. The observation of pseudomorphism during fluid-mediated replacement reactions has been interpreted as being evidence for an interface coupled dissolution-precipitation reaction, during which: (1) the rate of dissolution of the parent phase is closely coupled to the rate of precipitation of the product phase (Putnis 2002); and (2) interconnected porosity is developed in the product phase, which in turn facilitates the movement of fluids to the reaction interface (Engvik *et al.* 2008; Hovelmann *et al.* 2009).

The preferential dissolution of the anorthite (2Al:2Si) component relative to the albite (2Al:2Si) component in plagioclase was demonstrated experimentally by Gudbrandsson *et al.* (2014) to occur at room temperature (22 ± 2 ºC) at acid conditions, where the dissolution rate increases with increasing

anorthite content. The process has been explained as being due to the weaker bonding in the $(AlO_4)^{5-}$ tetrahedra (*i.e.* 3/4 ev) relative to the $(SiO_4)^{4-}$ tetrahedra (*i.e.* 1 ev), and the relatively higher Al content in anorthite relative to albite. In general, the higher SiO_2 would be expected to enhance the stabilization of albite *versus* anorthite. As such, a higher anorthite content in a given plagioclase would lead to it being relatively unstable. In the current study, the interpretation that the replacement of plagioclase (An_{20-30}) by albite was concomitant with the development of fine-grained clinozoisite-epidote crystals suggests that Ca^{2+}, Al^{3+}, and Si^{4+} ions, transferred to the fluid phase during the preferential dissolution of the anorthite component of least-altered plagioclase (An_{20-30}), were subsequently precipitated as clinozoisite-epidote.

Of interest to this study is whether the porosity observed in albite played a role in facilitating the emplacement of chalcopyrite in the Victor footwall rocks. At the micron-scale, chalcopyrite grains are preferentially hosted in porous albite, and were observed to exhibit a close spatial association with fine-grained secondary epidote-group minerals (± chlorite, titanite and actinolite-tremolite) and micropores that have developed in the albite (Fig. 21a-c). Furthermore, micron-scale grains of chalcopyrite were observed to locally occur directly within the micropores in albite. This suggests that the porosity in plagioclase (An_{0-10}) developed pre- to syn-chalcopyrite formation. It is possible that at the micron-scale, the movement of a chalcopyrite fluid or melt was enhanced by the interconnected porosity generated as a result of the replacement of least-altered plagioclase by albite through an interface coupled dissolution-precipitation mechanism. However, chalcopyrite disseminations were frequently measured in excess of 6000 µm along their long axes, which is a thousandfold increase over the largest observed pore in albite (~6 µm measured along its long axis). Thus, many chalcopyrite disseminations are too large to have been directly accommodated by the observed pore space in albite.

The assemblage of silicates observed to line the margins of chalcopyrite grains (albite + epidote- and chlorite-group minerals + actinolite-tremolite ± titanite) is relatively consistent in terms of mineral species, regardless of the grain size of chalcopyrite. However, textural evidence suggests that the process(es) responsible for the generation of porosity at the micron-scale and at the millimeter and greater scale may have differed. In comparison to the fine-grained plagioclase (An_{0-10}) neoblasts that are host to micron-scale chalcopyrite, selvage-type albite: (1) is often coarser-grained; (2) lacks inclusions of fine-grained epidote-group minerals; (3) lacks the distinct simple twin that frequently occurs in the plagioclase neoblast; and (4) is non-porous; thus, the selvage-type albite is texturally distinct and is unlikely to have directly pseudomorphed a parent plagioclase neoblast. While the Si, Al and Na required to precipitate the selvage-type albite may have been sourced from the dissolution of pre-existing plagioclase neoblasts, the dissolution-precipitation could not have been coupled. Several reasons are proposed to explain the texturally-distinct selvage-type albite: (1) a pre-existing dilational opening or structural weakness was exploited by a relatively higher fluid flux, resulting in relatively more material being removed by the fluid; (2) the fluid chemistries responsible for the formation of selvage-type albite and the pseudomorphic replacement plagioclase (An_{20-30}) neoblasts by albite were different; (3) there was a delay between the dissolution event that generated the open space and the precipitation of new albite (Putnis 2009); and (4) the rate of dissolution was fast compared to the rate of nucleation.

1.9.6 Mineral chemistry

As demonstrated in the plot of Fe^{3+} *versus* Al (Fig. 25a), representing the clinozoisite-epidote solid solution, fine-grained clinozoisite-epidote (Czo-Ep) in saussuritized plagioclase is Fe-poor relative to replacement-type Czo-Ep (after annite-phlogopite) and selvage-type Czo-Ep. Fine-grained Czo-Ep in plagioclase was observed to be contemporaneous with the replacement of least-altered plagioclase (An_{20-}

$_{30}$) by porous albite, which likely occurred through an interface coupled dissolution-precipitation mechanism. Thus, it is probable that some of the Ca, Si, and Al liberated during the preferential dissolution of the anorthite component of plagioclase (An_{20-30}) was reprecipitated as Czo-Ep. Possible sources of Fe in Czo-Ep include tetrahedrally-coordinated Fe released during the breakdown of plagioclase, Fe released during the replacement of co-existing annite-phlogopite and ilmenite to chlorite and titanite, respectively (Fig. 14g, k), and Fe derived from an extrinsic source. The relative enrichment in the Fe:Al ratio of Czo-Ep after annite-phlogopite, relative to fine-grained Czo-Ep in plagioclase, likely reflects the comparative Fe-enrichment in annite-phlogopite *versus* plagioclase. Iron released during the breakdown and replacement of a Fe-rich biotite-group mineral by Czo-Ep would be expected to partition into the replacement Czo-Ep (Fig. 14i).

Clinozoisite-epidote in contact with both disseminated and massive vein-type chalcopyrite (Ccp) exhibits a pronounced Fe:Al enrichment *versus* fine-grained Czo-Ep in plagioclase. The $Fe^{3+}/(Fe^{3+}+Al)$ ratio of Czo-Ep has been demonstrated experimentally to increase with increasing fO_2, and decrease with increasing temperature (Liou *et al.* 1983). In the Epidote Zone of the Fraser Mine, SIC North Range, Farrow & Watkinson (1992) described a positive correlation between the Fe:Al ratio in epidote-group minerals and alteration intensity, which the authors interpreted as reflecting an evolution to more oxidizing fluids. The observed Fe:Al enrichment in Czo-Ep grains directly in contact with Ccp in Victor footwall rocks suggests that these were domains subjected to relatively high fO_2 (or decreasing temperatures), or that these domains were proximal to an Fe^{3+}-rich source. As previously discussed, textural evidence indicates that selvage-type Czo-Ep is paragenetically earlier than Ccp. Therefore, it is suggested that prior to Ccp emplacement, selvage-type Czo-Ep developed as a result of the preferential infiltration of a relatively acidic, oxidized Fe-bearing fluid along relatively weak, permeable planes (*e.g.* quartz-plagioclase interfaces, plagioclase neoblast boundaries, fractures), resulting in the preferential

dissolution of the anorthite component of plagioclase and precipitation of albite + Czo-Ep into open space. A possible source of Fe^{3+} may have been Ccp via leaching or diffusion. Iron X-ray maps of Czo-Ep in contact with Ccp were homogeneous, showing no evidence of zonation in Fe:Al content, suggesting that diffusion of Fe^{3+} between Ccp and Czo-Ep did not occur.

In chlorite-group minerals, the concentrations of Fe, Ni and Mn were observed to increase with proximity to a massive Ccp vein. In contrast, the Fe-content of Czo-Ep was not observed to change depending on the textural-style of Ccp. Two major compositional populations of chlorite are identified (Fig. 26a): (1) a population proximal (*i.e.* <1 m) to massive vein-style Ccp is relatively high in Fe/(Fe+Mg) and slightly enriched in Al_{tot}; and (2) a population distal (*i.e.* >1 m) to massive vein-style Ccp is relatively low in Fe/(Fe+Mg) and slightly depleted in Al_{tot}. Furthermore, chlorite proximal to the massive Ccp is relatively enriched in Ni and Mn. In the SIC footwall environment, Fe- and Ni-enriched chlorites proximal to sulfide mineralization have previously been documented (Farrow & Watkinson 1992; Tuba & Ames 2015; O'Callaghan *et al.* 2017).

The Fe-Ni-Mn-enriched chlorites identified proximal a sulfide vein may reflect the influence of a relatively Fe-Ni-Mn-rich fluid prior to sulfide emplacement. Following crystallization of Czo-Ep, the fluid may have evolved to a chemistry that favored the crystallization of chlorite, resulting in the observed chlorite overgrowths of Czo-Ep. It has previously been suggested that metal-poor fluids in the SIC footwall may have become metal-enriched upon interaction with pre-existing sulfides of magmatic origin (Hanley & Bray 2009; Hanley *et al.* 2011). Therefore, it is possible that the source of the Fe + Ni + Mn may have been the massive chalcopyrite ± millerite ± pentlandite vein. As no obvious trend was observed between calculated Fe^{3+}/Fe_{tot} ratios in chlorite and proximity to Ccp mineralization, it is unclear what influence fO_2 may have had on the relative distributions of Fe between coexisting chlorite and Czo-Ep.

The observed enrichment of Mn in chlorite relative to Czo-Ep suggests that Mn preferentially partitioned into chlorite over Czo-Ep. In the epidote crystal structure, Mn exists preferentially in the oxidized Mn^{3+} state, substituting for Al^{3+} and Fe^{3+} in to the M1 site. As Mn in chlorite appears to be sensitive to proximity to the massive Ccp vein, while no such sensitivity was observed with respect to Czo-Ep, fO_2 may have been too low to stabilize Mn^{3+}. In biotite-group minerals, the substitution of relatively large octahedrally-coordinated Fe^{2+} and Mn^{2+} cations for smaller octahedrally-coordinated Mg^{2+} cations has been shown to distort the cell parameters of the biotite structure, producing a lattice misfit between the octahedral and tetrahedral sheets, which can be offset by substituting smaller octahedral Ni^{2+} and Al_{IV} (Guidotti *et al.* 1977; Henry & Guidotti 2002). A similar relationship may have enhanced the substitutions of Fe^{2+} + Mg + Ni into the chlorite crystal lattice in grains proximal to the massive Ccp vein.

The positive correlation between Fe-Ni-Mn-content and proximity to the massive chalcopyrite vein was observed in both selvage-type chlorite and disseminated fine-grained chlorite in plagioclase. This may suggest that the same fluid was involved in the crystallization of both textural populations of chlorite.

1.10 Conclusions

The chief purpose of this study was to develop a quantifiable method of evaluating the mineralogical and textural changes reflected in the footwall rocks of the North and East ranges when approaching the SIC contact, as well as the container rocks to footwall-hosted vein-type sulfide mineralization at the Victor deposit. These changes reveal important insights into the geological processes that affected the footwall rocks prior to and following the emplacement of the SIC, as summarized in the following

temporal sequence which suggests dissolution of the felsic wall rocks to footwall veins preceded formation of disseminated chalcopyrite.

1. In the Levack Gneiss Complex, the footwall to the North and East ranges of the SIC, quartz and plagioclase retain textures indicative of plastic deformation prior to the 1.85 Ga Sudbury Event, as recorded by accumulated strain (*i.e.* an increase in dislocation density) seen as micro-deformational features.
2. Following the Sudbury Event, recovery and recrystallization of the strained quartzo-feldspathic phases occurred, promoted by heat from the cooling SIC. The newly formed strain-free neoblastic grains, formed at least 500 m from the inferred SIC footwall contact, are seen to coarsen and develop dihedral angles approaching 120 º, likely driven by a reduction in interfacial energy. Further, prevalence of Carlsbad twins in annealed feldspar neoblasts suggests that the footwall rocks were subjected to relatively rapid increases in temperature.
3. Later, localized plastic deformation and continued recovery and recrystallization is recorded by a variety of textures in quartz (*e.g.* undulatory extinction, deformation bands, flattened grains, intra-grain bulges) that overprint earlier annealed, granoblastic quartz. These micro-structures are associated with relatively low temperatures (300 – 400 ºC) and/or fast strain rates. There is no textural evidence to suggest chalcopyrite was subjected to this episode(s) of strain.
4. Quartz-plagioclase intergrowth textures consistent with incipient melting occur at least ~80 m from the inferred SIC contact in the Victor footwall. The intergrowths retain evidence of accumulated strain (*e.g.* undulatory extinction in quartz), and show limited degrees of recovery & recrystallization relative to coexisting granoblastic quartz and plagioclase. This suggests crystallization was post the peak of SIC-related thermal annealing of quartz and plagioclase.

5. An acidic, oxidized fluid reacted with the least-altered plagioclase (An_{20-30}), promoting dissolution and formation of porous albite and epidote-group minerals. The newly generated porosity and permeability likely enhanced further fluid ingress, alteration and replacement of coexisting mineral phases.
6. The breakdown of annite-phlogopite and ilmenite provided a source of Fe necessary to form epidote- and chlorite-group minerals. The population of clinozoisite-epidote in contact with chalcopyrite is enriched in Fe^{3+}:Al, indicating increasing conditions of fO_2 and/or greater proximity to an Fe source. The increase in Fe, Ni and Mn content of chlorite proximal to the massive chalcopyrite vein may indicate that this was a site of higher metal-rich fluid flux. Chlorite geothermometry constrains *T* to ~310 – 385 ºC, with no statistically significant differences between the different textural populations of chlorite.
7. Crystals of secondary albite, clinozoisite-epidote, actinolite-tremolite and chlorite in contact with chalcopyrite exhibit textures indicative of open-spaced growth, implying that they crystallized pre-chalcopyrite emplacement. Thus, domains of enhanced porosity-permeability in plagioclase (An_{0-10}) likely favoured entry of a Cu(-Ni)-bearing fluid or melt marginal to the massive chalcopyrite veins.

1.11 References

Ames, D.E., Farrow, C.E.G., (2007). Metallogeny of the Sudbury mining camp. Mineral Deposits of Canada, Geological Association of Canada, Mineral Deposits Division, Special Publication, vol. 5, pp. 329–350.

Ames, D.E., Davidson, A., Wodicka, N., (2008). Geology of the Giant Sudbury Polymetallic Mining Camp, Ontario. Can. Econ. Geol. 103, 1067–1077.

Angiboust, S., & Harlov, D. (2017). Ilmenite breakdown and rutile-titanite stability in metagranitoids: Natural observations and experimental results. American Mineralogist, 102, 1696–1708.

Benkó, Z., Mogessie, A., Molnár, F., Severson, M. J., Hauck, S. A., & Raic, S. (2015). Partial Melting Processes and Cu-Ni-PGE Mineralization in the Footwall of the South Kawishiwi Intrusion at the Spruce Road Deposit, Duluth Complex , Minnesota. Economic Geology, 110, 1269–1293. https://doi.org/10.2113/econgeo.110.5.1269

Bennett, G., Dressler, B.O., Robertson, J.A., (1991). The Huronian Supergroup and associated intrusive rocks. Geology of Ontario, Ontario Geological Survey, Special Volume 4, pp. 549–591

Boast, M. S., & Spray, J. G. (2006). Superimposition of a Thrust-Transfer Fault System on a Large Impact Structure : Implications for Ni-Cu-PGE Exploration at Sudbury. Economic Geology, 101, 1583–1594.

Bonazzi, P., & Menchetti, S. (2004). Manganese in Monoclinic Members of the Epidote Group: Piemontite and Related Minerals. Reviews in Mineralogy and Geochemistry, 56, 495–552.

Buerger, M. J. (1945). The genesis of twin crystals. American Mineralogist, 30, 469–482.

Bufe, N. A., Holness, M. B., & Humphreys, M. C. S. (2014). Contact Metamorphism of Precambrian Gneiss by the Skaergaard Intrusion. Journal of Petrology, 55(8), 1595–1617. https://doi.org/10.1093/petrology/egu035

Buntebarth, G., & Voll, G. (1991). Quartz Grain Coarsening by Collective Crystallization in Contact Quartzites. In *Equilibrium and Kinetics in Contact Metamorphism: The Ballachulish Igneous Complex and Its Aureole* (pp. 251–265).

Callegari, E., & Pieri, R. (1967). Crystallographic observations on some chess-board albites. Swiss Bulletin of Mineralogy and Petrology, 47, 99–110.

Card, K.D., Gupta, V.K., McGrath, P.H., Grant, F.S., (1984). The Sudbury Structure, its regional geological and geophysical setting. In: Pye, E.G., Naldrett, A.J., Giblin, P.E. (Eds.), The Geology and Ore Deposits of the Sudbury Structure. Ontario Geological Survey Special Volume 1, pp. 25–43.

Card, K.D., (1994). Geology of the Levack Gneiss Complex, the northern footwall of the Sudbury Structure. Current Research 1994-C. Geological Survey of Canada, pp. 269–278.

Cathelineau, M. (1988). Cation site occupancy in chlorites and illites as a function of temperature. Clay Minerals, 23, 471–485.

Clemens, J. D., & Holness, M. B. (2000). Textural evolution and partial melting of arkose in a contact aureole: A case study and implications. *Virtual Geosciences*, *5*(4), 1–14. https://doi.org/10.1007/s10069-000-0004-1

Coats, C.J.A., Snajdr, P., (1984). Ore deposits of the North Range, Onaping-Levack area, Sudbury. In: Pye, E.G., Naldrett, A.J., Giblin, P.E. (Eds.), The Geology and Ore Deposits of the Sudbury Structure. Ontario Geological Survey Special Volume 1, pp. 327–346.

Cooke, H.C., (1946). Problems of Sudbury geology. Geol. Surv. Can. Bull. 3, 77.

Corfu, F., Andrews, A.J., (1986). A U-Pb age for mineralized Nipissing diabase. Gowganda, Ontario. Can. J. Earth Sci. 27, 107–109.

Delpino, S., Bjerg, E., Mogessie, A., Schneider, I., Gallien, F., Castro de Machuca, B., … Kostadinoff, J. (2008). Mineral deformation mechanisms in granulite facies, Sierra de Valle Fértil, San Juan

province: Development conditions constrained by the P-T metamorphic path. *Revista de La Asociacion Geologica Argentina*, *63*(2), 181–195.

Dietz, R.S., (1964). Sudbury Structure as an astrobleme. J. Geol. 72, 412–434.

Douce, A. E. P. (1993). Titanium substitution in biotite: an empirical model with applications to thermometry, 0_2 and H_2O barometries, and consequences for biotite stability. Chemical Geology, 108, 133–162.

Drake, H., Tullborg, E.-L., & Annersten, H. (2008). Red-staining of the wall rock and its influence on the reducing capacity around water conducting fractures. Applied Geochemistry, 23, 1898–1920. https://doi.org/10.1016/j.apgeochem.2008.02.017

Dressler, B.O., (1984a). Sudbury Geological Compilation; Ontario Geological Survey Map 2491, Precambrian Geology Series,scale 150,000 geological compilation 1982–1983.

Dressler, B.O., (1984b). General geology of the Sudbury area. In: Pye, E.G., Naldrett, A.J., Giblin, P.E. (Eds.), The Geology and Ore Deposits of the Sudbury Structure. Ontario Geological Survey Special Volume 1, pp. 57–82.

Dressler, B.O., (1984c). The effects of the Sudbury Event and the intrusion of the Sudbury Igneous Complex on the footwall rocks of the Sudbury Structure. In: Pye, E.G., Naldrett, A.J., Giblin, P.E. (Eds.), The Geology and Ore Deposits of the Sudbury Structure. Ontario Geological Survey Special Volume 1, pp. 97–136.

Eggleton, R. A., & Banfield, J. F. (1985). The alteration of granitic biotite to chlorite. American Mineralogist, 70, 902–910.

Engvik, A. K., Putnis, A., Fitz Gerald, J. D., & Austrheim, H. (2008). Albitization of granitic rocks: the mechanism of replacement of oligoclase by albite. The C, 46, 1401–1415.

Erickson, T. M., Pearce, M. A., Taylor, R. J. M., Timms, N. E., Clark, C., Reddy, S. M., & Buick, I. S. (2015). Deformed monazite yields high-temperature tectonic ages. *Geology*, *43*(5), 383–386. https://doi.org/10.1130/G36533.1

Evans, B., Renner, J., & Hirth, G. (2001). A few remarks on the kinetics of static grain growth in rocks. *International Journal of Earth Sciences*, *90*(1), 88–103. https://doi.org/10.1007/s005310000150

Farrow, C. E. G., & Watkinson, D. H. (1992). Alteration and the Role of Fluids in Ni, Cu and Platinum-Group Element Deposition, Sudbury Igneous Complex Contact, Onaping-Levack area, Ontario. Mineralogy and Petrology, 46, 67–83.

Farrow, C.E.G., (1995). Geology, alteration, and the role of fluids in Cu-Ni-PGE mineralization of the footwall rocks to the Sudbury Igneous Complex, Levack and Morgan townships, Sudbury District, Ontario. PhD Thesis. Carleton University, Ottawa, ON, Canada. 407 pp.

Fedorowich, J.S., Roussel, D.H., Peredery, W.V., (1999). Sudbury breccia distribution and orientation in an embayment environment. Large Meteorite Impacts and Planetary Evolution II, Geological Society of America, Special Paper 339, pp. 305–315.

Ferrow, E. A., & Bagiński, B. W. (1998). Chloritisation of hornblende and biotite: a HRTEM study. Acta Geologica Polonica, 48(1), 107–113.

Ferry, J. M. (1979). Reaction Mechanisms, Physical Conditions, and Mass Transfer During Hydrothermal Alteration of Mica and Feldspar in Granitic Rocks From South-Central Maine, USA. Contributions to Mineralogy and Petrology, 68, 125–139.

Fitz Gerald, J. D., & Stünitz, H. (1993). Deformation of granitoids at low metamorphic grade. I : Reactions and grain size reduction. Tectonophysics, 221(3–4), 269–297.

Franz, G., & Liebscher, A. (2004). Physical and Chemical Properties of the Epidote Minerals - An Introduction -. Reviews in Mineralogy and Geochemistry, 56, 1–82.

Gibson, R. L., & Reimold, W. U. (2005). Shock pressure distribution in the Vredefort impact structure, South Africa. Geological Society of America Special Paper, 384, 329–349.

Gleason, G. C., & DeSisto, S. (2008). A natural example of crystal-plastic deformation enhancing the incorporation of water into quartz. Tectonophysics, 446, 16–30. https://doi.org/10.1016/j.tecto.2007.09.006

Gower, R. J. W., & Simpson, C. (1992). Phase boundary mobility in naturally deformed, high-grade quartzofeldspathic rocks: evidence for diffusional creep. *Journal of Structural Geology*, *14*(3), 301–313. https://doi.org/10.1016/0191-8141(92)90088-E

Gratz, A. J., Tyburczy, J., Christie, J., Ahrens, T., & Pongratz, P. (1988). Shock metamorphism of deformed quartz. Physics and Chemistry of Minerals, 16, 221–233.

Griggs, D. (1967). Hydrolytic Weakening of Quartz and Other Silicates. Geophysical Journal International, 14(1–4), 19–31.

Gudbrandsson, S., Wolff-Boenisch, D., & Gislason, S. R. (2014). Experimental determination of plagioclase dissolution rates as a function of its composition and pH at 22 °C. Geochimica et Cosmochimica Acta, 139, 154–172. https://doi.org/10.1016/j.gca.2014.04.028

Guidotti, C. V., Cheney, J. T., & Guggenheim, S. (1977). Distribution of titanium between coexisting muscovite and biotite in pelitic schists from northwestern Maine. American Mineralogist, 62, 438–448.

Guidotti, C. V., & Dyar, M. D. (1991). Ferric iron in metamorphic biotite and its petrologic and crystallochemical implications. American Mineralogist, 76, 161–175.

Guillope, M., & Poirier, J. P. (1979). Dynamic recrystallization during creep of single-crystalline halite: An experimental study. Journal of Geophysical Research, 84(2), 5557–5567.

Hanley, J. J., Mungall, J. E., Pettke, T., Spooner, E. T. C., & Bray, C. J. (2005). Ore metal redistribution by hydrocarbon–brine and hydrocarbon-halide melt phases, North Range footwall of the Sudbury Igneous Complex, Ontario, Canada. Mineralium Deposita, 40, 237–256. https://doi.org/10.1007/s00126-005-0004-z

Hanley, J. J., & Mungall, J. E. (2003). Chlorine enrichment and hydrous alteration of the Sudbury Breccia hosting footwall Cu-Ni-PGE mineralization at the Fraser mine, Sudbury, Ontario, Canada. The Canadian Mineralogist, 41, 857–881. https://doi.org/10.2113/gscanmin.41.4.857

Hanley, J., & Bray, C. (2009). The trace metal content of amphibole as a proximity indicator for Cu-Ni-PGE mineralization in the footwall of the Sudbury Igneous Complex, Ontario, Canada. *Economic Geology*, *104*(1), 113. https://doi.org/10.2113/gsecongeo.104.1.113

Hanley, J., Ames, D., Barnes, J., Sharp, Z., & Guillong, M. (2011). Interaction of magmatic fluids and silicate melt residues with saline groundwater in the footwall of the Sudbury Igneous Complex, Ontario, Canada: New evidence from bulk rock geochemistry, fluid inclusions and stable isotopes. *Chemical Geology*, *281*(1–2), 1–25. https://doi.org/10.1016/j.chemgeo.2010.11.009

Harlov, D., Tropper, P., Seifert, W., Nijland, T., & Forster, H.-J. (2006). Formation of Al-rich titanite (CaTiSiO4 O – CaAlSiO4OH) reaction rims on ilmenite in metamorphic rocks as a function of f H 2 O and f O 2. Lithos, 88, 72–84. https://doi.org/10.1016/j.lithos.2005.08.005

Hebil, K. E. (1978). A petrographic study of the granite breccia, Levack Mine, Sudbury, Ontario. Unpublished Masters Thesis.

Heilbronner, R., & Tullis, J. (2002). The effect of static annealing on microstructures and crystallographic preferred orientations of quartzites experimentally deformed in axial compression and shear. Geological Society, London, Special Publications, 200(1), 191–218.

Henry, D. J., & Guidotti, C. V. (2002). Titanium in biotite from metapelitic rocks : Temperature effects, crystal-chemical controls, and petrologic applications. American Mineralogist, 87, 375–382.

Hirth, G., & Tullis, J. (1992). Dislocation creep regimes in quartz aggregates. Journal of Structural Geology, 14(2), 145–159.

Hirth, J. P., & Lothe, J. (1982). *Theory of Dislocations* (2nd ed.). Krieger Publishing Company.

Holness, M. B. (2006). Melt – Solid Dihedral Angles of Common Minerals in Natural Rocks. Journal of Petrology, 47(4), 791–800. https://doi.org/10.1093/petrology/egi094

Holness, M. B., Eds, I., Forster, M. A., Gerald, J. D. F., & Lister, G. S. (2010). Decoding dihedral angles in melt-bearing and solidified rocks. Journal of the Virtual Explorer, 35(3), 3–42. https://doi.org/10.3809/jvirtex.2010.00265

Holness, M. B., & Sawyer, E. W. (2008). On the Pseudomorphing of Melt-filled Pores During the Crystallization of Migmatites. Journal of Petrology, 49(7), 1343–1363. https://doi.org/10.1093/petrology/egn028

Hövelmann, J., Putnis, A., Geisler, T., Schmidt, B. C., & Golla-Schindler, U. (2010). The replacement of plagioclase feldspars by albite: Observations from hydrothermal experiments. Contributions to Mineralogy and Petrology, 159, 43–59. https://doi.org/10.1007/s00410-009-0415-4

Humphreys, F. J., & Hatherly, M. (2004). *Recrystallization and Related Annealing Phenomena* (2nd ed.).

Ivanov, B.A., Deutsch, A., (1999). Sudbury impact event: cratering mechanics and thermal history. Geological Society of America Special Paper 339, p. 389–397.

Jago, B.C., Morrison, G.G., Little, T.L., (1994). Metal zonation patterns and microtextural and micromineralogical evidence for Alkali- and Halogen-rich fluids in the genesis of the Victor Deep and McCreedy East footwall copper orebodies, Sudbury Igneous Complex. In: Lightfoot, P.C., Naldrett, A.J. (Eds.), Proceedings of the Sudbury–Noril'sk Symposium. Ontario Geological Survey Special Volume 5, pp. 65–75.

James, R.S., Dressler, B.O., 1992. Nature and significance of the Levack Gneiss Complex—Footwall rocks of the north and east ranges of the Sudbury Igneous Complex. Can. Mineral. 30, 487–488.

James, R.S., Peredery, W., Sweeny, J.M., 1992a. Thermobarometric studies on the Levack Gneisses, footwall rocks to the Sudbury Igneous Complex. In: Dressler, B.O., Sharpton, V.L. (Eds.), Papers Presented to the International Conference on Large Meteorite Impacts and Planetary Evolution. LPI Contribution 790, 41. References and Sudbury Bibliography **619**

James, R.S., Sweeney, J.M., Peredery, W.V., 1992b. Thermobarometry of the Levack gneisses—Footwall rocks to the Sudbury Igneous Complex. Lithoprobe Report No. 25, Abitibi-Grenville Transect, pp. 179–182.

James, R.S., Peredery, W.V., Sweeney, J.M., 1994. Thermobarometric studies of the Levack Gneisses, footwall rocks to the Sudbury Igneous Complex. GAC/AGC-MAC/AMC Joint Annual Meeting (abstract), vol. 19, p. 54.

Jin, Y., Bernacki, M., Rohrer, G. S., Rollett, A. D., Lin, B., & Bozzolo, N. (2013). Formation of annealing twins during recrystallization and grain growth in 304L austenitic stainless steel. Materials Science Forum, 753, 113–116.

Johannes, W., and Holtz, F., (1996), Petrogenesis and experimental petrology of granitic rocks: Berlin: Springer-Verlag, p. 335

Keskinen, M., & Liou. (1987). Stability relations of Mn-Fe-Al piemontite. Journal of Metamorphic Geology, 5, 495–507.

Kontak, D. J., & Clark, A. H. (2002). Genesis of the Giant, Bonanza San Rafael Lode Tin Deposit, Peru: Origin and Significance of Pervasive Alteration. Economic Geology, 97, 1741–1777.

Kontak, D.J., MacInnis, L.M., Ames, D.E., Rayner, N.M., Joyce, N., (2015). A geological, petrological, and geochronological study of the Grey Gabbro unit of the Podolsky Cu-(Ni)-PGE deposit, Sudbury, Ontario, with a focus on the alteration related to the formation of sharp-walled chalcopyrite veins. In: Ames, D.E., Houlé, M.G. (Eds.), Targetted Geoscience Initiative 4 Canadian Nickel-Copper-Platinum Group Elements-Chromium Ore Systems – Fertility, Pathfnders, New, Revised Models. Geological Survey of Canada, Open File 7856, pp. 287–301.

Kontonikas-charos, A., Ciobanu, C. L., Cook, N. J., Ehrig, K., Krneta, S., & Kamenetsky, V. S. (2017). Feldspar evolution in the Roxby Downs Granite , host to Fe-oxide Cu-Au- (U) mineralisation at Olympic Dam , South Australia. Ore Geology Reviews, 80, 838–859. https://doi.org/10.1016/j.oregeorev.2016.08.019

Krogh, T.E., Davis, D.W., Corfu, F., (1984). Precise U-Pb zircon and baddeleyite ages for the Sudbury area. In: Pye, E.G., Naldrett, A.J., Giblin, P.E. (Eds.), The Geology and Ore Deposits of the Sudbury Structure. Ontario Geological Survey Special Volume 1, pp. 431–446.

Kruhl, J. H. (2001). Crystallographic control on the development of foam textures in quartz, plagioclase and analogue material. International Journal of Earth Sciences, 90, 104–117. https://doi.org/10.1007/s005310000170

Kruhl, J. H., Wirth, R., & Morales, L. F. G. (2013). Quartz grain boundaries as fluid pathways in metamorphic rocks. Journal of Geophysical Research, 118, 1–11. https://doi.org/10.1002/jgrb.50099

Lafrance, B., John, B. E., & Scoates, J. S. (1996). Syn-emplacement recrystallization and deformation microstructures in the Poe Mountain anorthosite, Wyoming. Contributions to Mineralogy and Petrology, 122(4), 431–440.

Lafrance, B., John, B. E., & Frost, B. R. (1998). Ultra high-temperature and subsolidus shear zones: examples from the Poe Mountain anorthosite, Wyoming. *Journal of Structural Geology*, *20*(7), 945–955. https://doi.org/10.1016/S0191-8141(98)00021-2

Laporte, D., Rapaille, C., & Provost, A. (1997). Wetting angles, equilibrium melt geometry, and the permeability threshold of partially molten crustal protoliths. In Granite: From Segregation of Melt to Emplacement Fabrics (pp. 31–54).

Lenauer, I., Riller, U., (2012a). Geometric consequences of ductile fabric development from brittle shear faults in mafic melt sheets: Evidence from the Sudbury Igneous Complex, Canada. J. Struct. Geol. 35, 40–50.

Lenauer, I., Riller, U., (2012b). Strain fabric geometry within and near deformed igneous sheets: the Sudbury Igneous Complex, Canada. Tectonophysics 558–559, 45–57.

Levine, J. S. F., Mosher, S., & Rahl, J. M. (2016). The role of subgrain boundaries in partial melting. Journal of Structural Geology, 89, 181–196. https://doi.org/10.1016/j.jsg.2016.06.006

Liang, H., Yongsheng, Z., & ChangRong, H. (2013). Water-enhanced plastic deformation in felsic rocks. Science China, 56(2), 203–216. https://doi.org/10.1007/s11430-012-4367-6

Lightfoot, P. C. (2016). Nickel Sulfide Ores and Impact Melts: Origin of the Sudbury Igneous Complex. Elsevier.

Liou, J. G., Kim, H. S., & Maruyamaf, S. (1983). Prehnite - Epidote Equilibria and their Petrologic Applications. Journal of Petrology, 24(4), 321–342.

Marshall, B., & Gilligan, L. B. (1993). Remobilization, syn-tectonic processes and massive sulphide deposits. Ore Geology Reviews, 8, 39–64.

Martin, R. L., & Parsons, I. (1997). Dislocation formation and albitization in K-feldspars from the Shap granite. American Mineralogist, 82, 557–570.

McCormick, K. A., & McDonald, A. M. (1999). Chlorine-bearing amphiboles from the Fraser mine, Sudbury, Ontario, Canada: Description and crystal chemistry. The Canadian Mineralogist, 37(6), 1385–1403.

Meldrum, A., Abdel-Rahman, A.-F. M., Martin, R. F., & Wodicka, N. (1997). The nature, age and petrogenesis of the Cartier Batholite, northern flank of the Sudbury Structure, Ontario, Canada. Precambrian Research, 82, 265–285.

Messerschmidt, U., & Bartsch, M. (2003). Generation of dislocations during plastic deformation. Materials Chemistry and Physics, 81, 518–523. https://doi.org/10.1016/S0254-0584(03)00064-6

Mohammad, Y. O., & Maekawa, H. (2008). Origin of titanite in metarodingite from the Zagros Thrust Zone, Iraq. American Mineralogist, 93, 1133–1141. https://doi.org/10.2138/am.2008.2580

Molnar, F., Watkinson, D. H., & Jones, P. C. (2001). Multiple Hydrothermal Processes in Footwall Units of the North Range, Sudbury Igneous Complex, Canada, and Implications for the Genesis of Vein-Type Cu-Ni-PGE Deposits. Economic Geology, 96, 1645–1670.

Morad, S., El-Ghali, M. A. K., Caja, M. A., Sirat, M., Al-Ramadan, K., & Mansurbeg, H. (2009). Hydrothermal alteration of plagioclase in granitic rocks from Proterozoic basement of SE Sweden. Geological Journal, 45(1), 105–116.

Morales, L. F. G., Mainprice, D., Lloyd, G. E., Law, R. D., & Euge, P. (2011). Crystal fabric development and slip systems in a quartz mylonite : an approach via transmission electron microscopy and viscoplastic self-consistent modelling. Deformation Mechanisms, Rheology and Tectonics: Microstructures, Mechanics and Anisotropy. Geological Society, London, Special Publications, 360, 151–174.

Morrison, G.G., Jago, B.C., Little, T.L., (1994). Footwall mineralization of the Sudbury Igneous Complex. In: Lightfoot, P.C., Naldrett, A.J. (Eds.), Proceedings of the Sudbury-Noril'sk Symposium, Ontario Geological Survey Special Volume 5, pp. 57–64.

Muir, T.L., (1984). The Sudbury Structure, considerations and models for an endogenic origin. In: Pye, E.G., Naldrett, A.J., Giblin, P.E. (Eds.), The Geology and Ore Deposits of the Sudbury Structure. Ontario Geological Survey Special Volume 1, pp. 449–489.

Mukai, H., Austrheim, H., Putnis, C. V., & Putnis, A. (2014). Textural evolution of plagioclase feldspar across a shear zone: Implications for deformation mechanism and rock strength. *Journal of Petrology*, *55*(8), 1457–1477. https://doi.org/10.1093/petrology/egu030

Norberg, N., Neusser, G., Wirth, R., & Harlov, D. (2011). Microstructural evolution during experimental albitization of K-rich K-feldspar. Contributions to Mineralogy and Petrology, 162, 531–546. https://doi.org/10.1007/s00410-011-0610-y

O'Callaghan, J. W., Linnen, R. L., & Lightfoot, P. C. (2017). Mineralogical and geochemical characteristics of Sudbury Breccia adjacent to footwall Cu-Ni-PGE sulfide veins and structures in the Creighton and Coleman deposits. The Canadian Mineralogist, 55, 909–943. https://doi.org/10.3749/canmin.1600058

Ostermann, M., Deutsch, A., Therriault, A., Grieve, R.A.F., (1996a). The Sudbury impact structure: geochemistry of the drill cores 70011 and 52848. Meteor. Planet. Sci. 31A, 102.

Ostermann, M., Schaerer, U., Deutsch, A., (1996b). Impact melt dikes in the Sudbury multi-ring basin (Canada), implications from uranium-lead geochronology on the Foy offset dike. Meteoritics 31 (4), 494–501.

Park, Y., Ree, J., & Kim, S. (2001). Lattice preferred orientation in deformed-then-annealed material : observations from experimental and natural polycrystalline aggregates, 127–135. https://doi.org/10.1007/s005310000163

Parsons, I., & Martin, R. L. (2009). Mutual replacement reactions in K-feldspars II: Trace element partitioning and geothermometry. Contributions to Mineralogy and Petrology, 157, 641–661. https://doi.org/10.1007/s00410-008-0358-1

Pattison, D. R. M., & Harte, B. (1997). The geology and evolution of the Ballachulish Igneous Complex and Aureole. Scottish Journal of Geology, 33(1), 1–29. https://doi.org/10.1144/sjg33010001

Pearce, M. A., & Wheeler, J. (2014). Microstructural and Metamorphic Constraints on the Thermal Evolution of the Southern Region of the Lewisian Gneiss Complex, NW Scotland. Journal of Petrology, 55(10), 2043–2066. https://doi.org/10.1093/petrology/egu049

Péntek, A., Molnár, F., Tuba, G., Watkinson, D. H., & Jones, P. C. (2013). The Significance of Partial Melting Processes in Hydrothermal Low Sulfide Cu-Ni-PGE Mineralization Within the Footwall of the Sudbury Igneous Complex, Ontario, Canada. Economic Geology, 108, 59–78.

Péntek, A., Molnár, F., Watkinson, D. H., & Jones, P. C. (2008). Footwall-type Cu-Ni-PGE mineralization in the Broken Hammer area, wisner township, north range, Sudbury structure. Economic Geology, 103(5), 1005–1028. https://doi.org/10.2113/gsecongeo.103.5.1005

Péntek, A., Molnár, F., Watkinson, D. H., Jones, P. C., & Mogessie, A. (2011). Partial melting and melt segregation in footwall units within the contact aureole of the Sudbury Igneous Complex (North and East Ranges, Sudbury structure), with implications for their relationship to footwall Cu – Ni – PGE mineralization. International Geology Review, 53(2), 291–325. https://doi.org/10.1080/00206810903101313

Plümper, O., & Putnis, A. (2009). The Complex Hydrothermal History of Granitic Rocks: Multiple Feldspar Replacement Reactions under Subsolidus Conditions. Journal of Petrology, 50(5), 967–987. https://doi.org/10.1093/petrology/egp028

Prevec, S. A., & Cawthorn, R. G. (2002). Thermal evolution and interaction between impact melt sheet and footwall: A genetic model for the contact sublayer of the Sudbury Igneous Complex, Canada. Journal of Geophysical Research, 107, 1–14.

Putnis, A. (2002). Mineral replacement reactions: from macroscopic observations to microscopic mechanisms. Mineralogical Magazine, 66(5), 689–708. https://doi.org/10.1180/0026461026650056

Putnis, A., & Putnis, C. V. (2007). The mechanism of reequilibration of solids in the presence of a fluid phase. Journal of Solid State Chemistry, 180, 1783–1786. https://doi.org/10.1016/j.jssc.2007.03.023

Rosenberg, C. L., & Riller, U. (2000). Partial-melt topology in statically and dynamically recrystallized granite. Geology, 28(1), 7–10. https://doi.org/10.1130/0091-7613(2000)28<7

Roussel, D.H., Gibson, H.L., Jonasson, I.R., (1997). The tectonic, magmatic and mineralization history of the Sudbury structure. Explor. Mining Geol. 6, 1–22.

Roussel, D.H., Meyer, W., Prevec, S.A., (2002). Bedrock geology and mineral deposits. The Physical Environment of the City of Greater Sudbury, Ontario Geological Survey, Special Volume 6, pp. 21–55.

Roussel, D.H., Fedorowich, J.S., Dressler, B.O., (2003). Sudbury Breccia (Canada): a product of the 1850 Ma Sudbury Event and host to footwall Cu-Ni-PGE deposits. Earth Sci. Rev. 60, 147–174.

Ruiz-Agudo, E., Putnis, C. V., & Putnis, A. (2014). Coupled dissolution and precipitation at mineral-fluid interfaces. Chemical Geology, 383, 132–146. https://doi.org/10.1016/j.chemgeo.2014.06.007

Santimano, T., Riller, U., (2012). Revisiting thrusting, reverse faulting and transpression in the southern Sudbury Basin, Ontario. Precambrian Res. 200–203, 74–81.

Sawyer, E. W. (1999). Criteria for the recognition of partial melting. Physic, 24(3).

Shanks, W.S., Schwerdtner, W.M., (1991a). Crude quantitative estimates of the original northwest-southeast dimension of the Sudbury Structure, south central Canadian Shield. Can. J. Earth Sci. 28, 1677–1686.

Shanks, W.S., Schwerdtner, W.M., (1991b). Structural analysis of the central and southwestern Sudbury Structure, Southern Province, Canadian Shield. Can. J. Earth Sci. 28 (3), 411–430.

Shaocheng, J., & Mainprice, D. (1990). Recrystallization and fabric development in plagioclase. Journal of Geology, 98, 65–79.

Shau, Y.-H., Yang, H.-Y., & Peacor, D. R. (1991). On oriented titanite and rutile inclusions in sagenitic biotite. American Mineralogist, 76, 1205–1217.

Shutong, X., & Shouyuan, J. (1991). Biotite percussion figures in naturally deformed mylonites. Tectonophysics, 190, 373–380.

Starkey, J. (1959). Chess-board albite from New Brunswick, Canada. Geological Magazine, 96(2), 141–145.

Smith, J. V., & Brown, W. L. (1988). *Feldspar Minerals, Volume 1* (2nd Revise). Springer-Verlag Berlin Heidelberg.

Stipp, M., Stünitz, H., Heilbronner, R., & Schmid, S. M. (2002). Dynamic recrystallization of quartz: correlation between natural and experimental conditions. https://doi.org/10.1144/GSL.SP.2001.200.01.11

Stöffler, D., & Langenhorst, F. (1994). Shock Metamorphism of quartz in nature and experiment: I. Basic observation and theory. Meteoritics, 29, 155–181. https://doi.org/10.1111/j.1945-5100.1994.tb00670.x

Stünitz, H., Fitz Gerald, J. D., & Tullis, J. (2003). Dislocation generation, slip systems, and dynamic recrystallization in experimentally deformed plagioclase single crystals. Tectonophysics, 372(3–4), 215–233. https://doi.org/10.1016/S0040-1951(03)00241-5

Therriault, A. M., Fowler, A. D., & Grieve, R. A. F. (2002). The Sudbury Igneous Complex: A Differentiated Impact Melt Sheet, 97, 1521–1540.

Trepmann, C. A., & Stöckhert, B. (2003). Quartz microstructures developed during non-steady state plastic flow at rapidly decaying stress and strain rate. Journal of Structural Geology, 25(12), 2035–2051. https://doi.org/10.1016/S0191-8141(03)00073-7

Tuba, G., Molnár, F., Ames, D. E., Péntek, A., Watkinson, D. H., & Jones, P. C. (2014). Multi-stage hydrothermal processes involved in "low-sulfide" Cu(-Ni)-PGE mineralization in the footwall of the Sudbury Igneous Complex (Canada): Amy Lake PGE zone, East Range. Mineralium Deposita, 49(1), 7–47. https://doi.org/10.1007/s00126-013-0468-1

Tuba, G., & Ames, D. E. (2015). Trace element signature of hydrothermal alteration assemblages (epidote, allanite, actinolite, titanite) in the footwall of the Sudbury Igneous Complex: A laser ablation ICP-MS trace element vectoring and fertility study. *Geological Survey of Canada: Open File 7757*. https://doi.org/10.4095/297051

Tullis, J., & Yund, R. A. (1989). Hydrolytic weakening of quartz aggregates: the effects of water and pressure on recovery. *Geophysical Research Letters*, *16*(11), 1343–1346.

Turner, F. J. (1951). Observations on twinning of plagioclase in metamorphic rocks. American Mineralogist, 36, 581–589.

Veblen, D. R., & Ferry, J. M. (1983). A TEM study of the biotite-chlorite reaction and comparison with petrologic observations. American Mineralogist, 68, 1160–1168.

Vernon, R. H. (1968). Microstructures of high-grade metamorphic rocks at Broken Hill, Australia. Journal of Petrology, 9(1), 1–22.

Vernon, R. H. (1965). Plagioclase twins in some mafic gneisses from Broken Hill, Australia. Mineralogical Magazine, 35(271), 488–507.

Vernon, R. H. (1975). Deformation and Recrystallization of a Plagioclase Grain. The American Mineralogist, 60, 884–888.

Vernon, R. H. (2004). A Practical Guide to Rock Microstructure. Cambridge University Press.

Vernooij, M. G. C., & Langenhorst, F. (2005). Experimental reproduction of tectonic deformation lamellae in quartz and comparison to shock-induced planar deformation features. Meteoritics & Planetary Science, 40(9/10), 1353–1361.

Walker, F. D. L., Lee, M. R., & Parsons, I. (1995). Micropores and Micropermeable Texture in K-feldspars: Geochemical and Geophysical Implications. *Mineralogical Magazine*, *59*(396), 505–534. https://doi.org/10.1180/minmag.1995.059.396.12

Xirouchakis, D., Lindsley, D. H., & Frost, B. R. (2001). Assemblages with Titanite, Ca-Mg-Fe olivine and pyroxenes, Fe-Mg-Ti oxides, and quartz: Part II. Application. American Mineralogist, 86(2), 254–264.

Xirouchakis, D., & Lindsley, D. H. (1998). Equilibria among titanite, hedenbergite, fayalite, quartz, ilmenite, and magnetite: Experiments and internally consistent thermodynamic data for titanite. American Mineralogist, 83, 712–725. https://doi.org/10.2138/am-1998-7-804

Yuguchi, T., Sasao, E., Ishibashi, M., & Nishiyama, T. (2015). Hydrothermal chloritization processes from biotite in the Toki granite, Central Japan: Temporal variations of the compositions of hydrothermal fluids associated with chloritization. American Mineralogist, 100, 1134–1152.

Zieg, M. J., & Marsh, B. D. (2005). The Sudbury Igneous Complex: Viscous emulsion differentiation of a superheated impact melt sheet. GSA Bulletin, 117(11/12), 1427–1450. https://doi.org/10.1130/B25579.1

Zolnai, A.l., Price, R.A., Helmstaedt, H., (1984). Regional cross section of the Southern Province

adjacent to Lake Huron, Ontario: implications for the tectonic significance of the Murray Fault Zone. Can. J. Earth Sci. 21, 447–456.

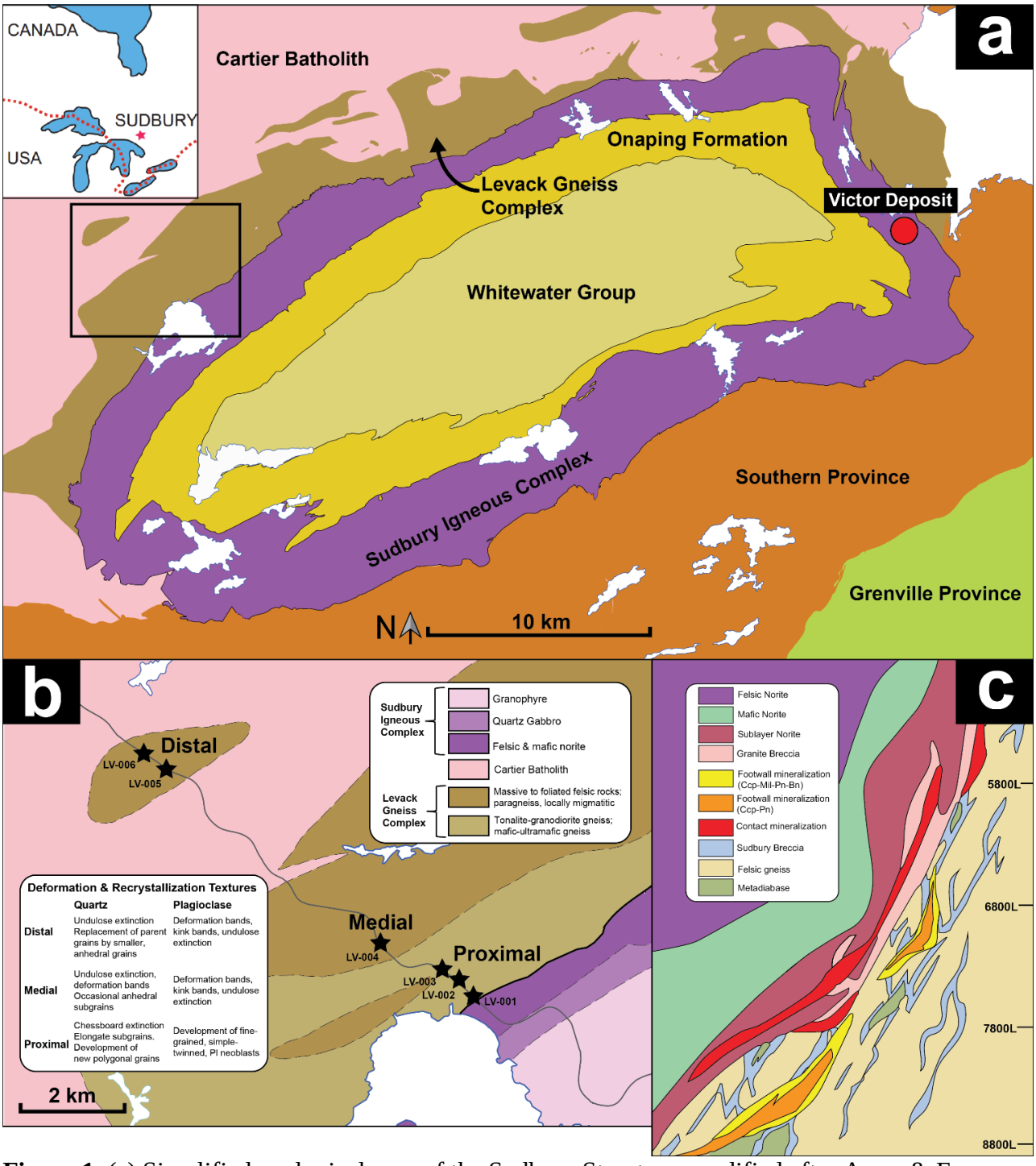

Figure 1. (a) Simplified geological map of the Sudbury Structure, modified after Ames & Farrow (2007). The Highway 144 traverse is located in the black box along the SIC North Range, and the Victor deposit is located by the red circle along the SIC East Range. (b) Highway 144 sampling traverse, with stars marking approximate sample locations. Key deformation and recovery textures in

quartz and plagioclase are summarized. (c) Geological model for the Victor mineral system, looking North (modified after Lightfoot 2017).

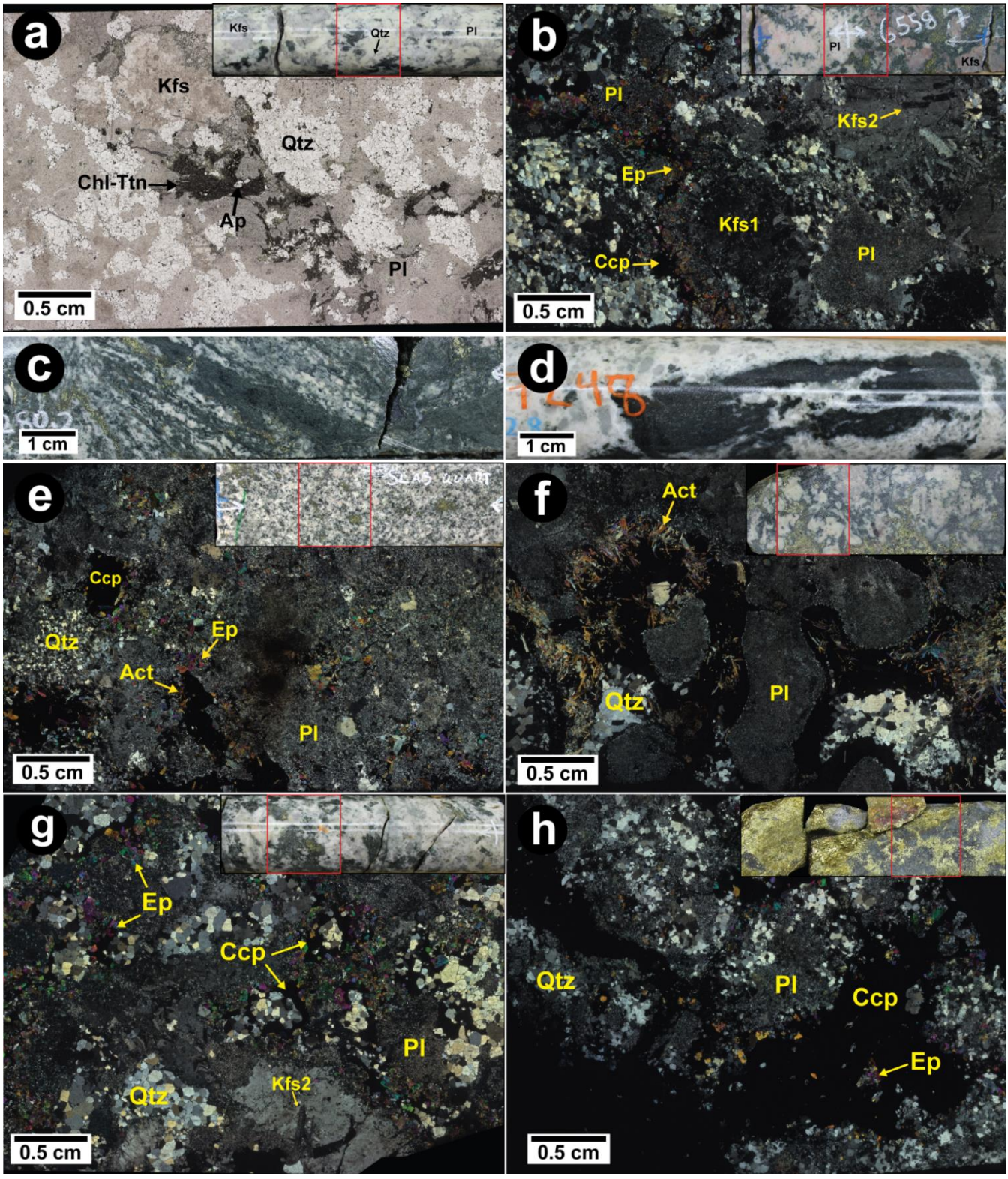
a
Kfs
Qtz
Pl
Kfs
Qtz
Chl-Ttn
Ap
Pl
0.5 cm
b
Pl
Kfs2
Ep
Kfs1
Ccp
Pl
0.5 cm
c
1 cm
d
1 cm
e
Ccp
Qtz
Ep
Act
Pl
0.5 cm
f
Act
Qtz
Pl
0.5 cm
g
Ep
Ccp
Pl
Qtz
Kfs2
0.5 cm
h
Qtz
Pl
Ccp
Ep
0.5 cm

Figure 2. Thin section scans and photographs of drill core showing key macro-textural features from mineralized and un-mineralized rocks in the Victor footwall deposit. **(a)** Massive granitoid with a clotted texture. **(b)** Massive monzogranite with chalcopyrite (Ccp) veinlets lined by epidote-group minerals (Ep). **(c)** Banded tonalite gneiss with Ccp + millerite (Mlr) veinlets. **(d)** Rafts of mafic rock in a massive tonalite. **(e)** Massive, fine-grained quartz-diorite with Ccp disseminations lined by euhedral actinolite. **(f)** Tonalite with veinlets of Ccp + pyrrhotite + Mlr lined by euhedral, acicular, comb-textured actinolite. **(g)** Massive granodiorite with disseminated Ccp wrapping granoblastic polygonal quartz aggregates. **(h)** Massive Ccp vein cross-cutting massive tonalite with dark 'clotted' texture in hand sample. Note the dark green, strongly saussuritized plagioclase. Abbreviations: Act – actinolite-tremolite; Ap – apatite; Ccp - chalcopyrite; Chl – chlorite; Ep – epidote-group mineral; Kfs – K-feldspar; Pl - plagioclase; Qtz – quartz; Ttn – titanite.

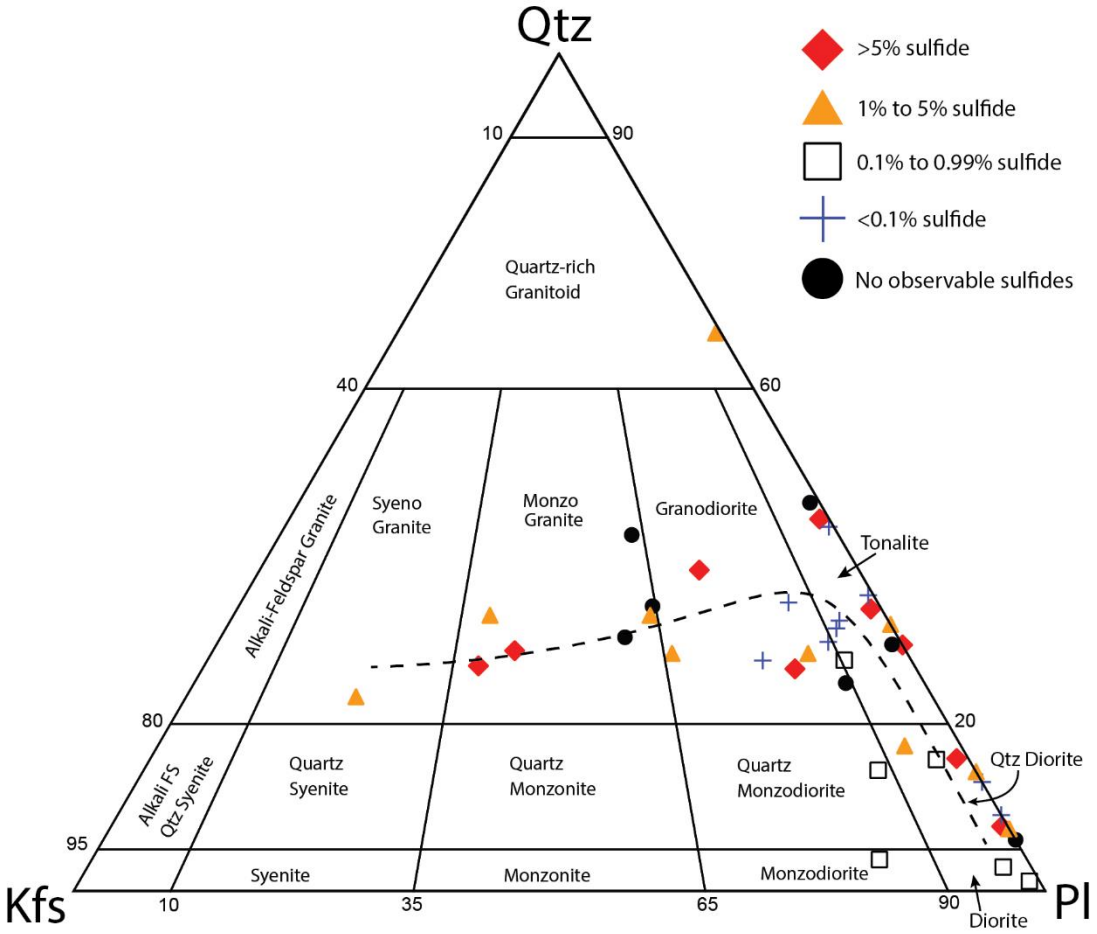

Figure 3. QAP ternary plot of sampled rocks from the Victor footwall, grouped based on total modal sulfide.

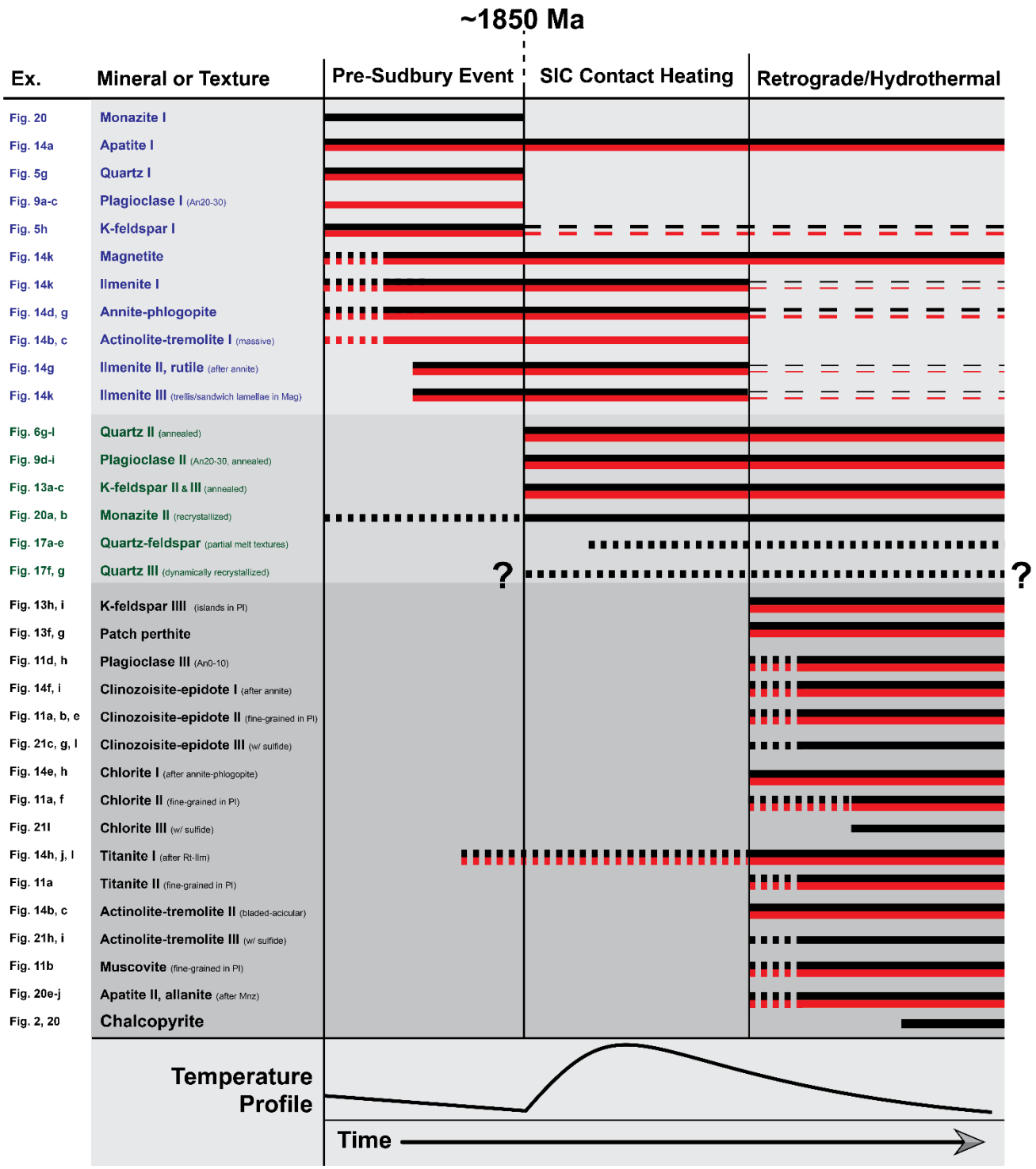

Figure 4. Mineral paragenesis for North Range (red) and Victor (black) footwall rocks. Relative timing of mineral phases was determined from textural evidence. Short, thick dashes represent an

uncertainty in the relative introduction of a particular phase, while longer, thin dashes represent a decrease in the occurrence of a phase. A representative temperature profile shows the thermal evolution of the footwall rocks.

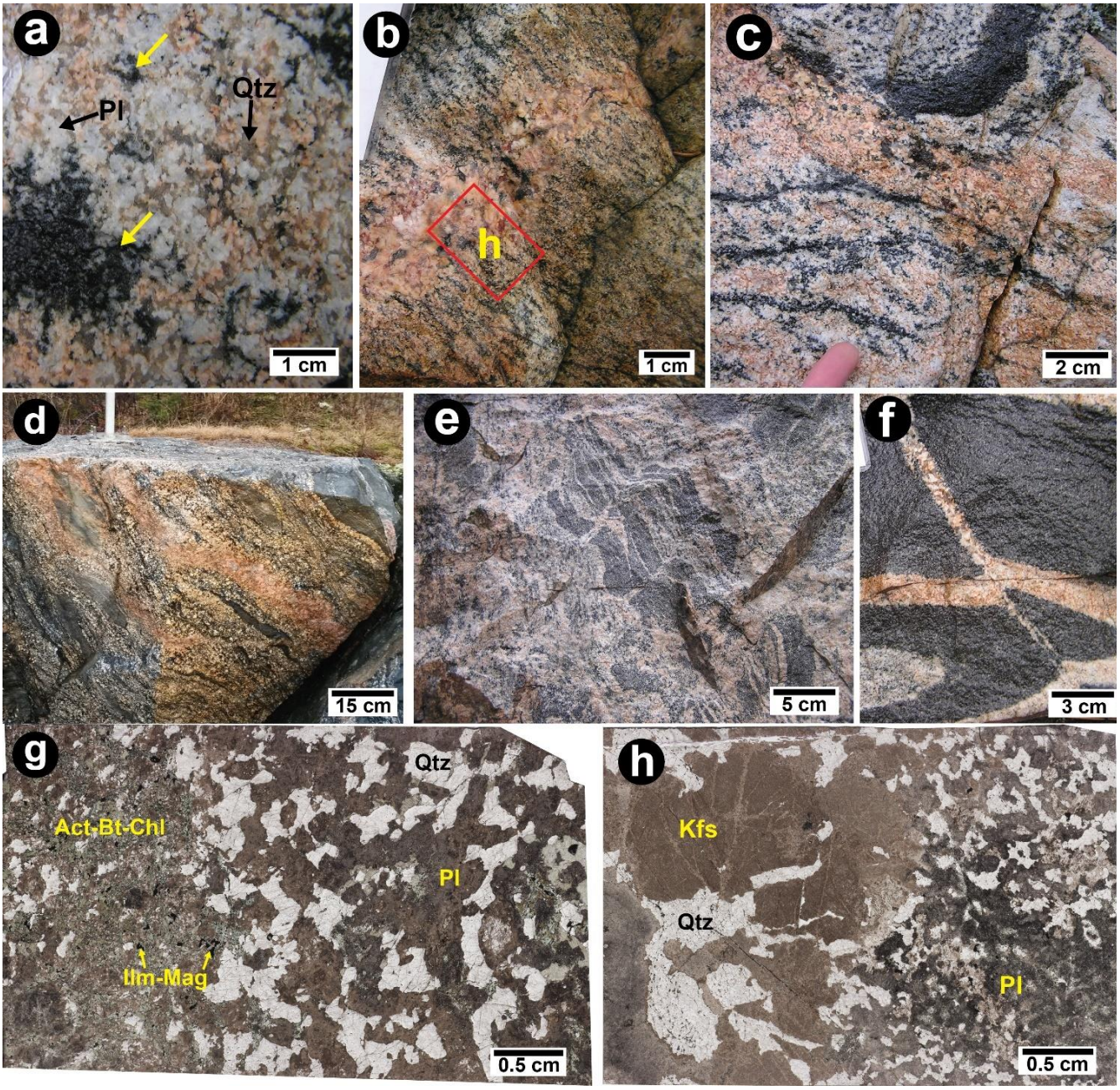

Figure 5. Photographs and thin-section scans (h, i) in plane-polarized light showing key macro-textural features of quartzo-feldspathic rocks of the Levack Gneiss Complex, North Range. **(a)** Medium- to coarse-grained, sub-equant to stubby prismatic plagioclase with interstitial anhedral quartz and clotted mafic domains (yellow arrows). **(b)** Gneissic foliation is cross-cut by a coarser-grained leucocratic (Qtz + Kfs) dykelet. **(c)** Felsic gneiss with a foliated (bottom) and massive (top)

fabric. **(d)** Plagioclase-porphyroblastic layers alternating with boudinaged rafts of mafic rock. **(e)** Rafts of mafic rock in a quartz-plagioclase-biotite gneiss. **(f)** Felsic dykes composed of a quartz-feldspar intergrowth, cross-cutting a medium-grained gabbroic rock. **(g, h)** Domains of medium- to coarse-grained quartz and feldspar intergrowths in contact with domains of finer-grained quartz and feldspar. Note the variable cuspate-lobate-straight grain boundaries of parent quartz. Abbreviations: Act – actinolite-tremolite; Bt – biotite-group mineral; Chl – chlorite-group mineral; Ilm – ilmenite; Kfs – K-feldspar; Mag – magnetite; Pl – plagioclase; Qtz – quartz.

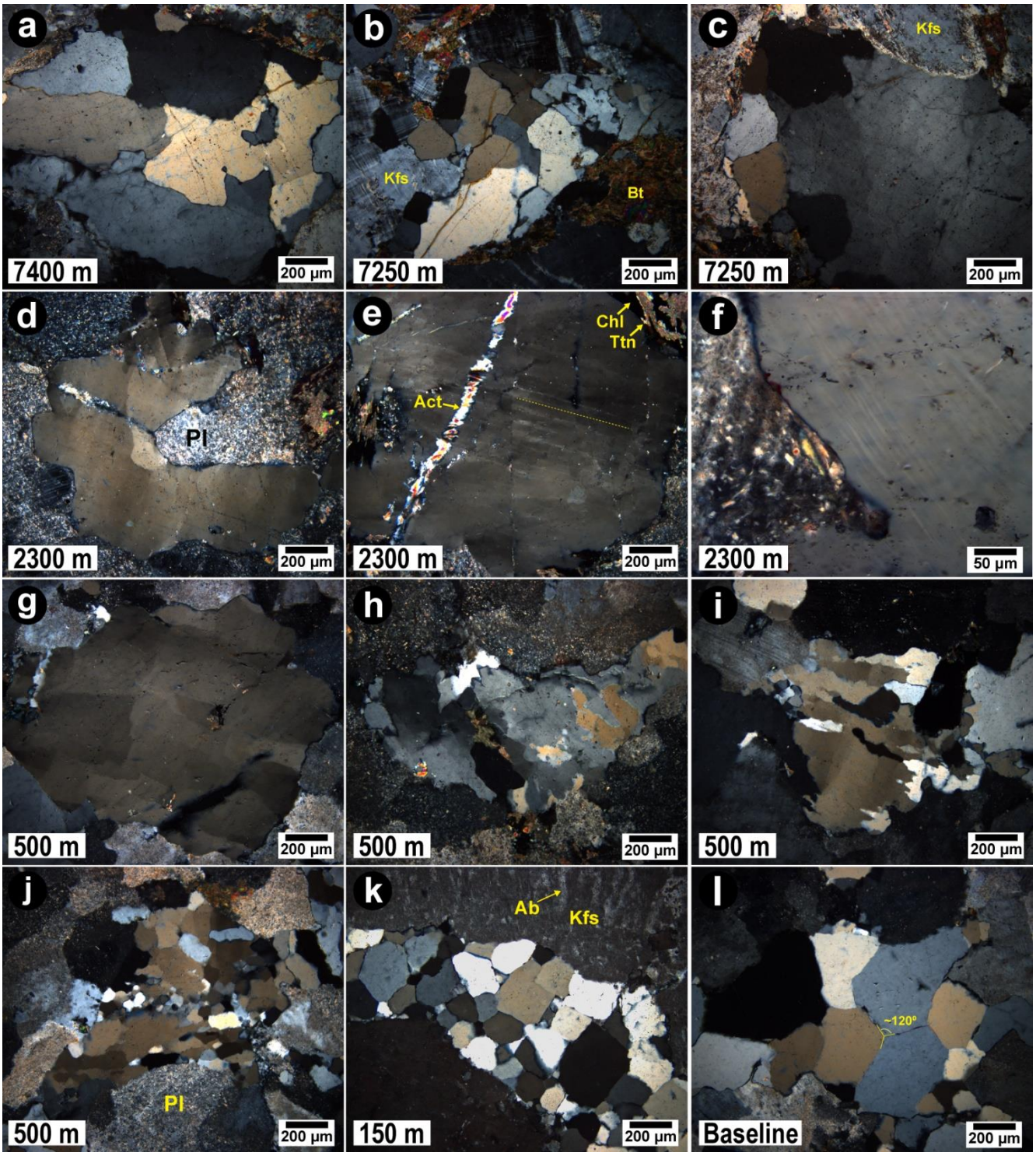

Figure 6. Examples in cross-polarized light (XPL) of deformational and recovery textures in quartz from North Range footwall rocks, with approximate horizontal distances from a baseline sample closest to the inferred SIC footwall contact. **(a, b, c)** Aggregates of recrystallized quartz grains with

variable interlobate to straight boundaries in distal rocks (7400 m, 7250 m). **(d)** Undulose extinction (2300 m). **(e, f)** Deformation lamellae (2300 m). **(g)** Weakly developed chessboard-type subgrains (500 m). **(h)** Poorly developed anhedral subgrains & grains in strained, primary quartz. **(i)** Elongate anhedral subgrains & grains orthogonal to 'ribbons' of extinction (500 m) **(j)** Fine-grained anhedral and polygonal grains (500 m). **(k, l)** Strain-free, granoblastic polygonal quartz. Note the new grains have coarsened closer to the contact (150 m to baseline). Abbreviations: Ab – albite; Act – actinolite-tremolite; Bt – biotite-group mineral; Chl – chlorite-group mineral; Kfs – K-feldspar; Pl – plagioclase; Ttn – titanite.

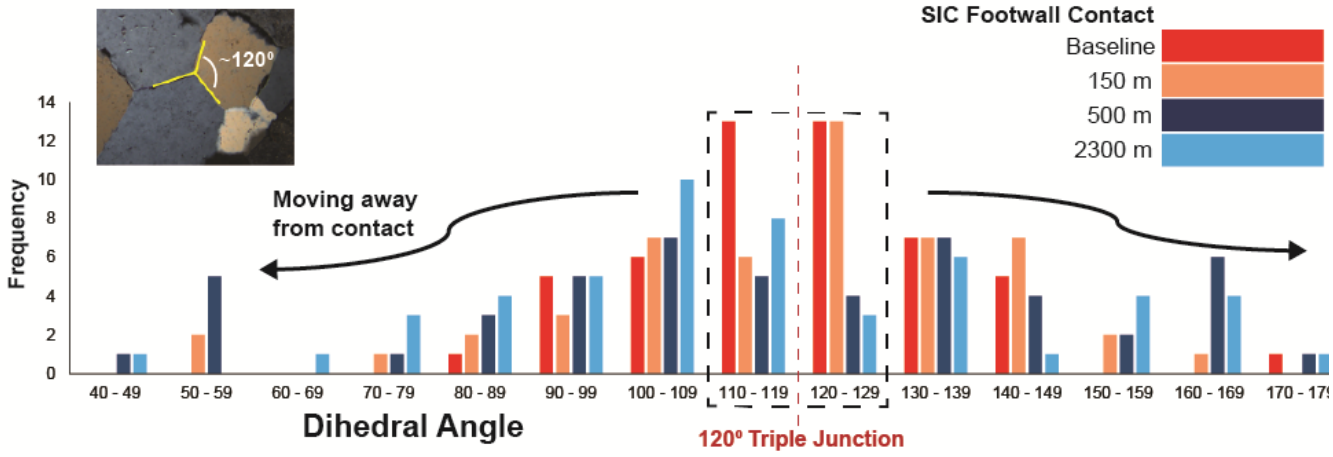

Figure 7. Frequency diagram for measured dihedral angles in quartz (see inset image) from North Range footwall rocks arranged with respect to distance from the basal contact with the SIC.

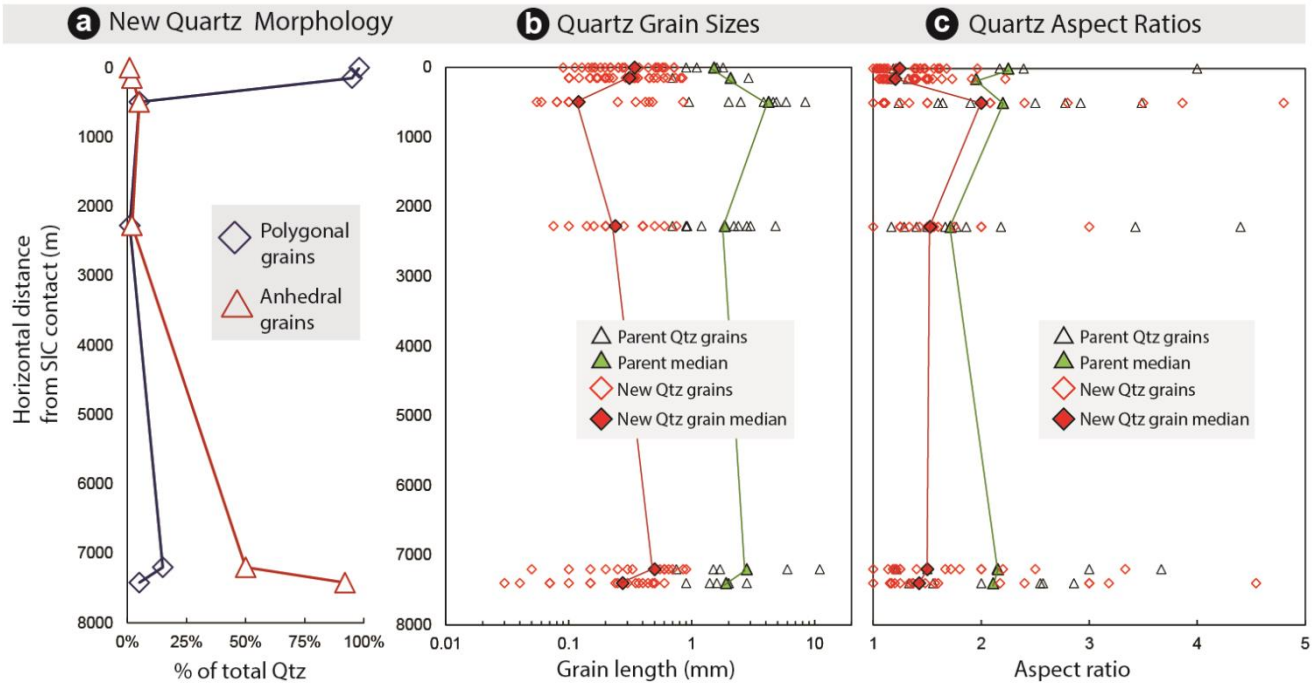

Figure 8. Plots of distance from basal SIC contact showing textural changes of quartz. **(a)** Percentage of total parent quartz that is composed of polygonal and anhedral grains. **(b)** Change in grain sizes (measured parallel to long axis) of parent quartz and new quartz grains. **(c) C**hange in aspect ratios of parent quartz grains and new quartz grains.

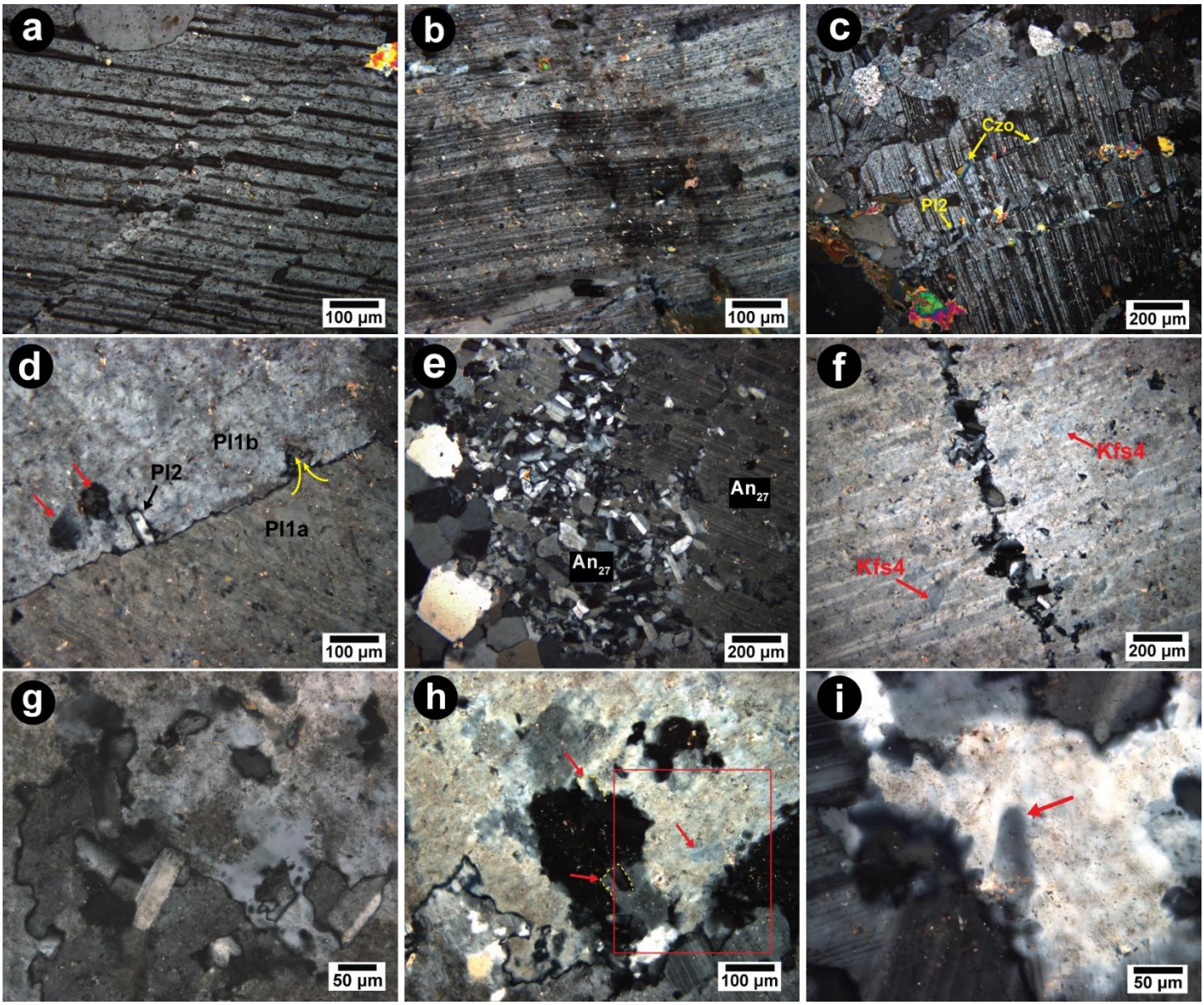

Figure 9. Photomicrographs in cross-polarized light (XPL) of deformational, recrystallization and recovery textures in plagioclase (Pl) from North Range footwall rocks. **(a)** Micro-offsets. **(b)** Band of extinction. **(c)** Development of clinozoisite and fine-grained Pl2 neoblasts along kink bands. **(d)** Intra-grain bulge recrystallized as a prismatic Carlsbad-twinned Pl2 neoblast. Red arrows indicate local patches of extinction in Pl1b. **(e)** Development of log-jam-texture in Pl2 (An~$_{27}$) along a quartz-Pl1 (An~$_{27}$) interface. **(f)** Development of Pl2 neoblasts along a linear feature in coarse-grained precursor Pl1. Note patchy anhedral K-feldspar 'islands' sub-parallel to albite twinning in Pl1. **(g, h)** Grain boundary mobility and bulging recrystallization in Pl, showing

various stages of neoblast development (red arrows). **(i)** Inset from (h), rotated ~90º clockwise, showing a poorly developed Pl neoblast and multiple intra-grain bulges projecting to the right. Abbreviations: Czo – clinozoisite-epidote; Kfs – K-feldspar; Pl – plagioclase.

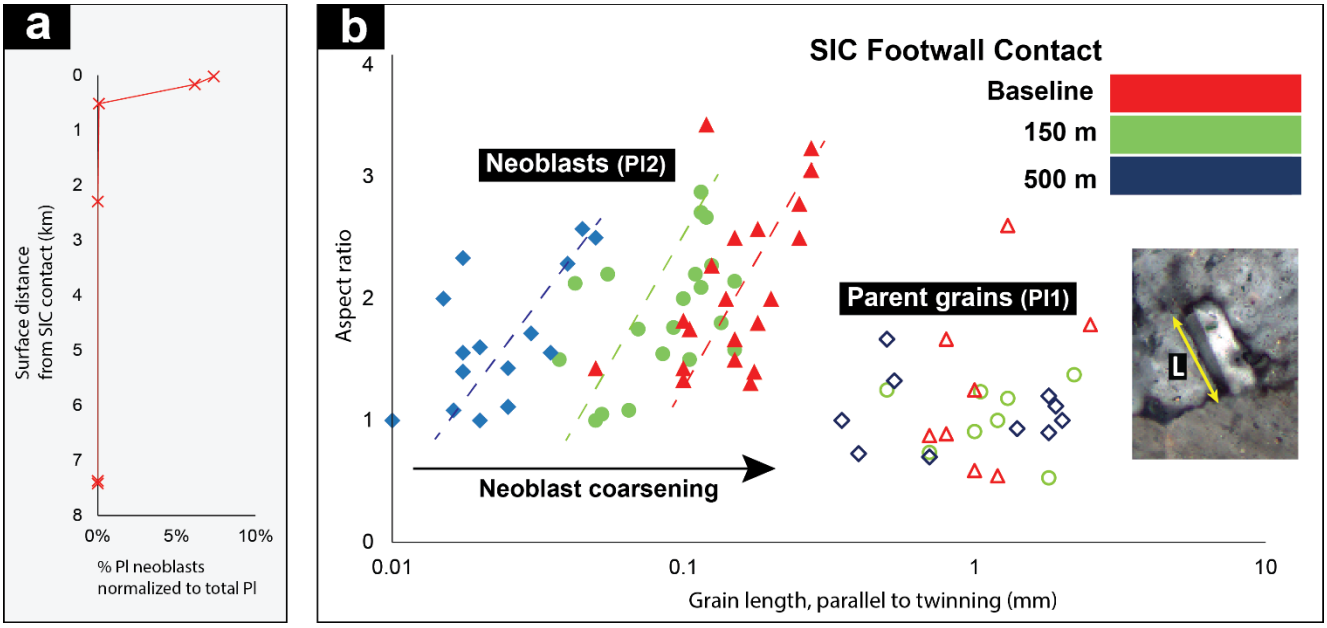

Figure 10. (a) Plot of distance from inferred SIC footwall contact showing onset of neoblast development in plagioclase (Pl). **(b)** Plot of length (see inset image) versus aspect ratio of Pl2 neoblasts with Carlsbad twinning as a function of distance from the inferred SIC footwall contact. Coarser-grained parent Pl1 grains are plotted for comparison.

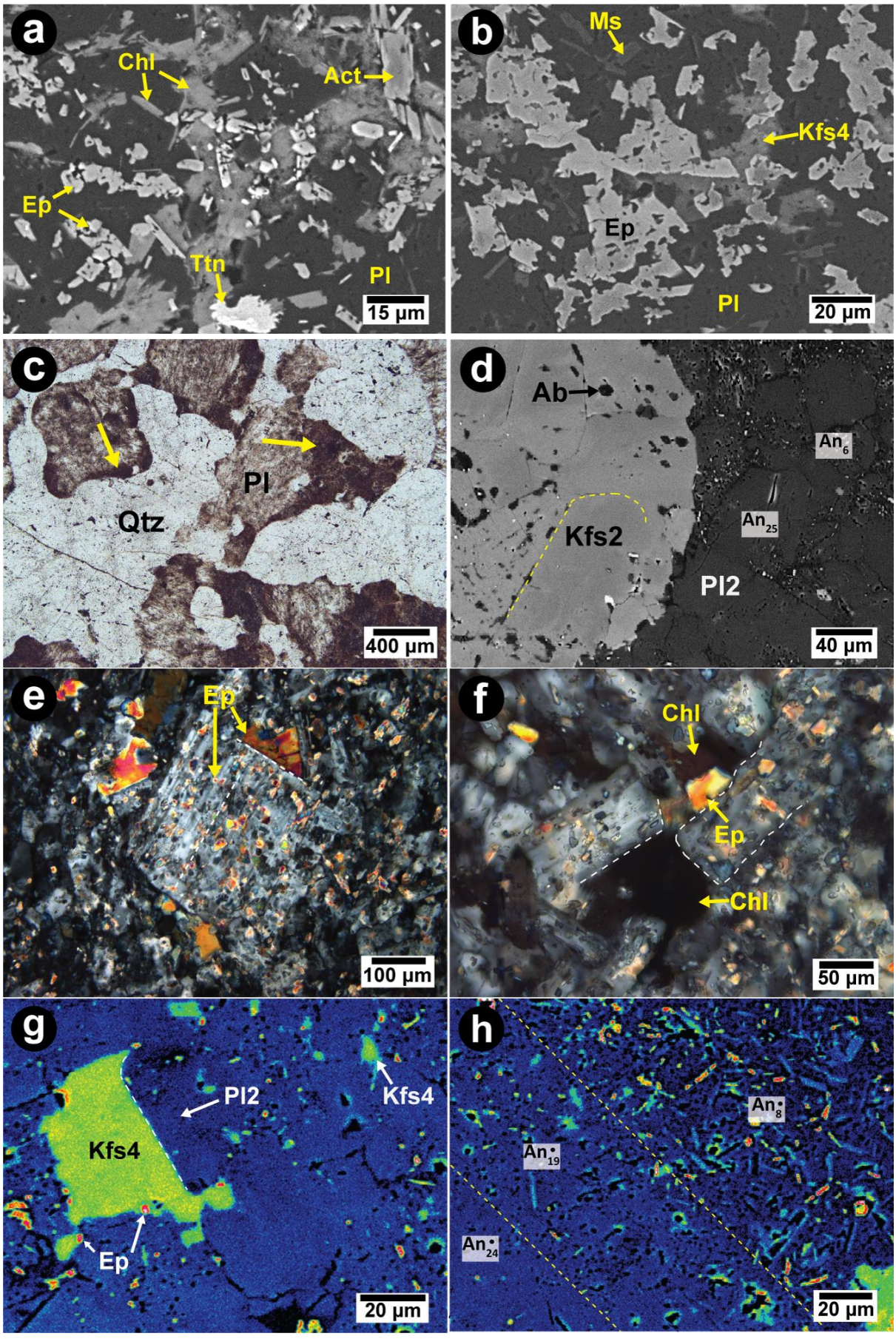
a
Chl
Act
Ep
Ttn
Pl
15 µm
b
Ms
Kfs4
Ep
Pl
20 µm
c
Pl
Qtz
400 µm
d
Ab
An6
An25
Kfs2
Pl2
40 µm
e
Ep
100 µm
f
Chl
Ep
Chl
50 µm
g
Pl2
Kfs4
Kfs4
Ep
20 µm
h
An8
An19
An24
20 µm

Figure 11. Photomicrographs of fine-grained secondary mineralogy in North and East range footwall rocks, taken in SEM-BSE mode (a, b, d, g, h), plane light (c), and cross-polarized light (e, f). **(a)** Fine-grained clinozoisite-epidote, chlorite, actinolite-tremolite and titanite in porous albite. **(b)** Fine-grained clinozoisite-epidote, K-feldspar (Kfs) and muscovite in porous albite. **(c)** Dusty areas (yellow arrows) with fine-grained secondary minerals in plagioclase (Pl) along quartz-Pl interfaces. **(d)** Pl (An_{25}) replaced by albite along neoblast boundaries (right), and blebby albite in Kfs neoblasts (see yellow outline). **(e, f)** Log-jam-textured Pl2 with fine-grained, interstitial epidote- and chlorite-group minerals. **(g)** Fine-grained Kfs4 interstitial to a prismatic, euhedral Pl2 neoblast (false-coloured BSE image). **(h)** Replacement of Pl ($An_{\sim 24}$) by albite with corresponding development of porosity and secondary minerals (false-coloured BSE image). Abbreviations: Ab – albite; Act – actinolite-tremolite; Chl – chlorite-group mineral; Ep – epidote-group mineral; Kfs – K-feldspar; Ms – muscovite; Pl – plagioclase; Qtz – quartz; Ttn – titanite.

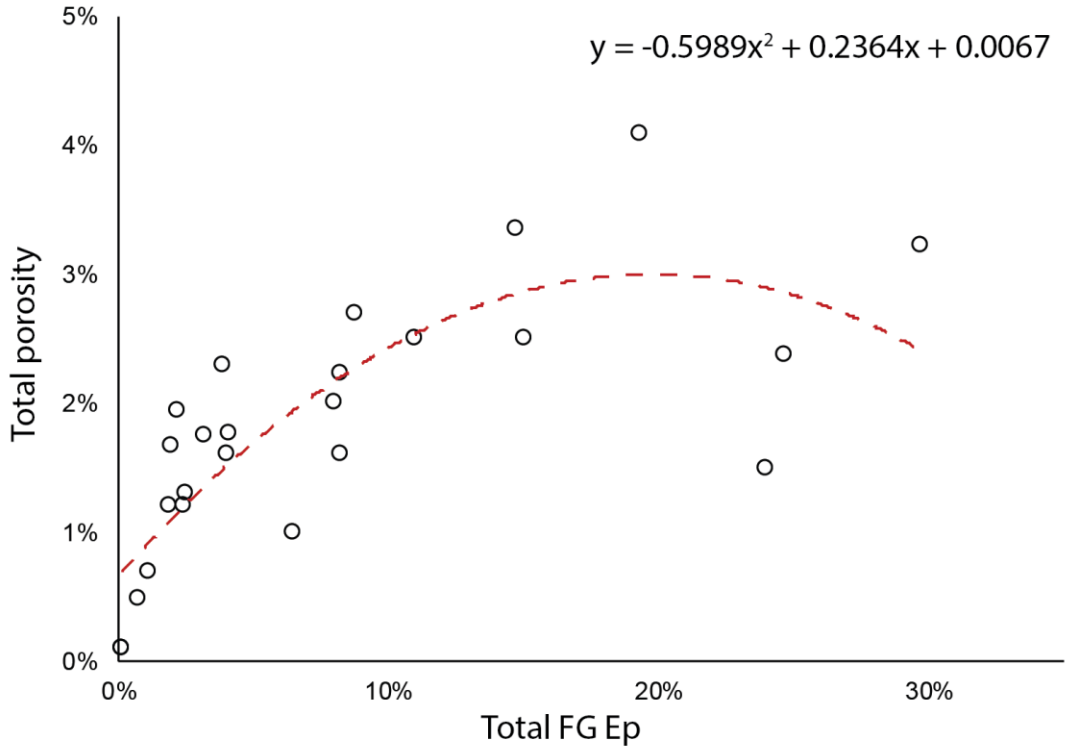

Figure 12. Plot of total fine-grained epidote-group minerals in plagioclase versus total porosity in plagioclase, measured from back-scattered electron images, with the corresponding polynomial regression. Abbreviations: FG Ep – fine-grained epidote-group minerals

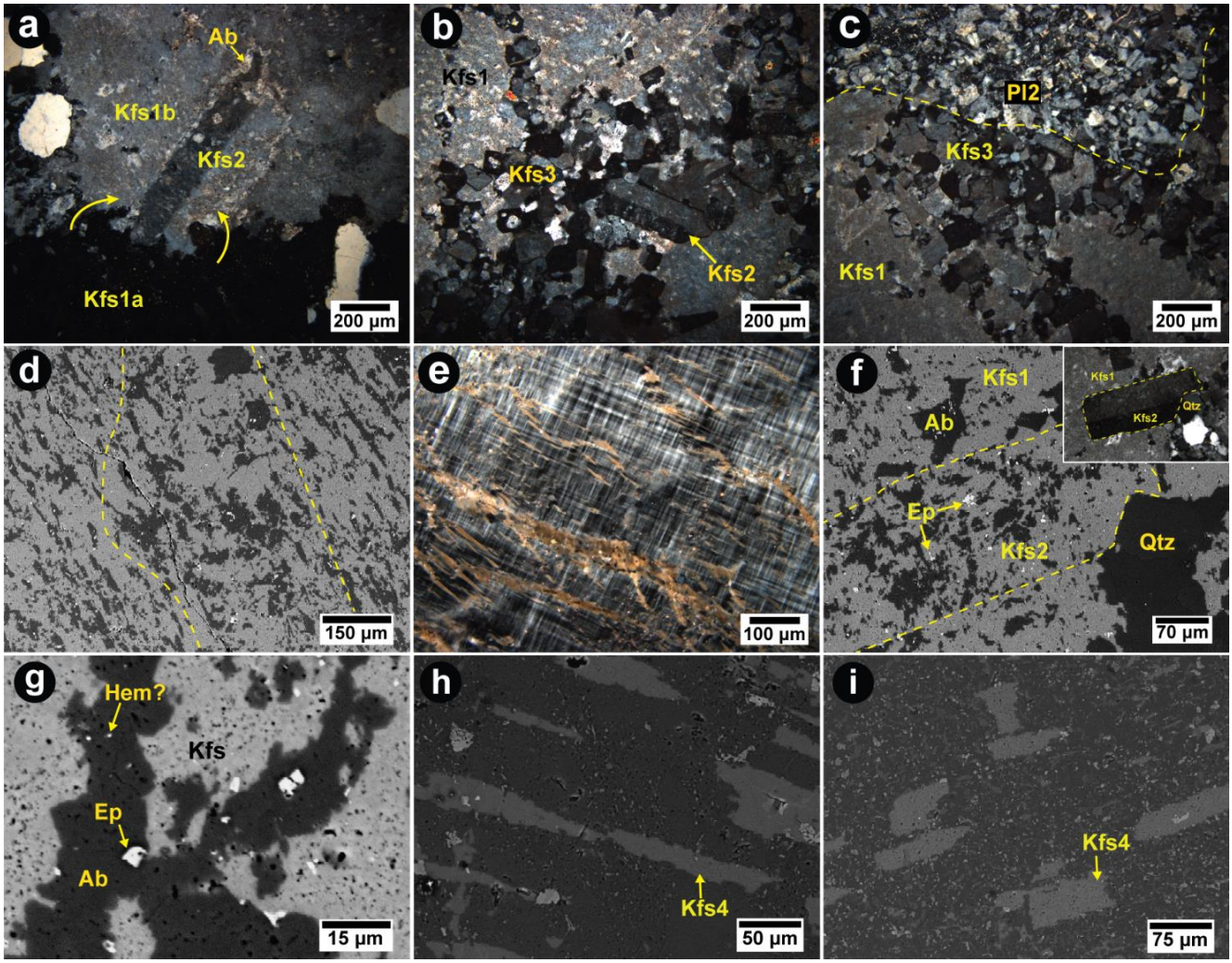

Figure 13. Photomicrographs of K-feldspar (Kfs) textures from North Range footwall rocks taken in cross-polarized light (a, b, c, e) and SEM-BSE mode (d, f, g, h, i). **(a)** Prismatic, perthitic, Carlsbad-twinned Kfs2 neoblast. Note the intra-grain bulges of Kfs1a projecting into Kfs1b, and patchy albite tracing the contour of the Kfs2 neoblast. **(b)** Development of Kfs2 and Kfs3 neoblasts. **(c)** Development of fine-grained Kfs3 and plagioclase neoblasts along a Kfs-plagioclase interface. **(d)** Lamellar patch perthite (outside dotted lines) and blebby patch perthite (inside dotted lines) in Kfs. **(e)** Flame perthite in tartan-twinned Kfs1. **(f)** Development of patch perthite in a coarse-grained Kfs1 and a prismatic Kfs2 neoblast (see inset). **(g)** Patch perthite with fine-grained clinozoisite and abundant micropores. **(h, i)** Weakly-porous (h) and porous (i) islands of Kfs4 in plagioclase.

Abbreviations: Ab – albite; Czo – clinozoisite; Hem – hematite; Kfs – K-feldspar; Pl – plagioclase; Qtz – quartz.

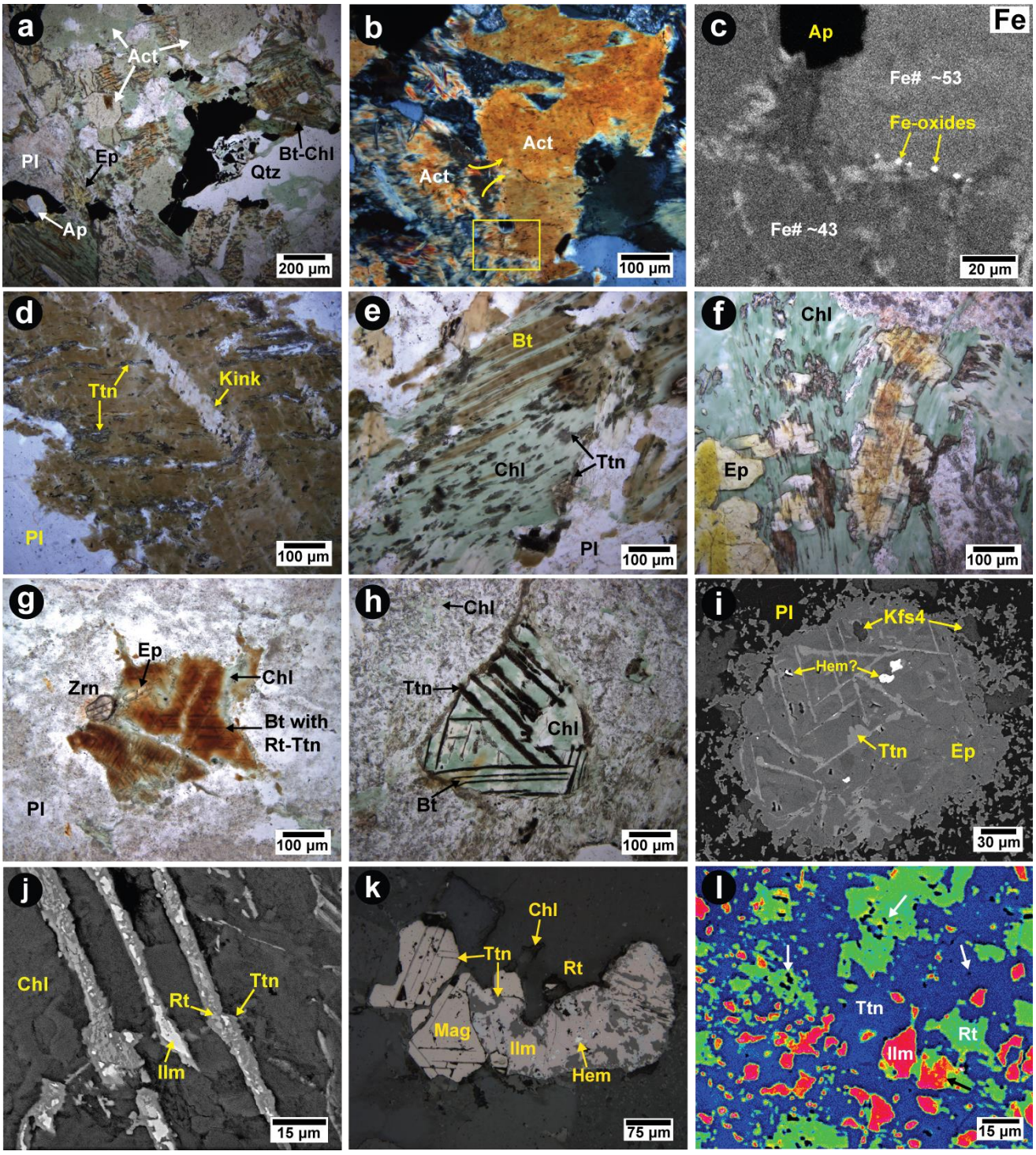

Figure 14. Photomicrographs of accessory minerals from North Range footwall rocks taken in plane light (a, d, e, f, g, h), cross-polarized light (b), reflected light (k), and SEM-BSE mode (i, j, l). **(a)** Minerals of the major mafic domain. **(b)** Interface between massive and acicular tremolite-actinolite

crystals **(c)** Fe X-ray map of the yellow box from (b). Note the fine grained Fe-oxides along the contact. **(d)** Titanite within the (001) plane of a kinked annite-phlogopite. **(e)** Partially chloritized annite-phlogopite. **(f)** Chlorite intergrown with clinozoisite-epidote and titanite. **(g)** Rutile and titanite needles in partially chloritized sagenitic annite-phlogopite; image down the *c*-axis. **(h)** Sagenitic texture in chlorite. Note the coarsened titanite lamellae. **(i)** Sagenitic texture in clinozoisite-epidote. **(j)** Sagenitic lamellae in chlorite; ilmenite (silver) and rutile (medium grey) are replaced by titanite (dark grey). **(k)** Trellis-textured magnetite intergrown with ilmenite. **(l)** Replacement of ilmenite by rutile (black arrow) and titanite. Note the development of microporosity (white arrows) (false-coloured BSE image). Abbreviations: Act – actinolite-tremolite; Ap – apatite; Bt – biotite-group mineral; Chl – chlorite; Ep – epidote-group mineral; Ilm – ilmenite; Kfs – K-feldspar; Mag – magnetite; Pl – plagioclase; Qtz – quartz; Rt – rutile; Ttn – titanite; Zrn – zircon.

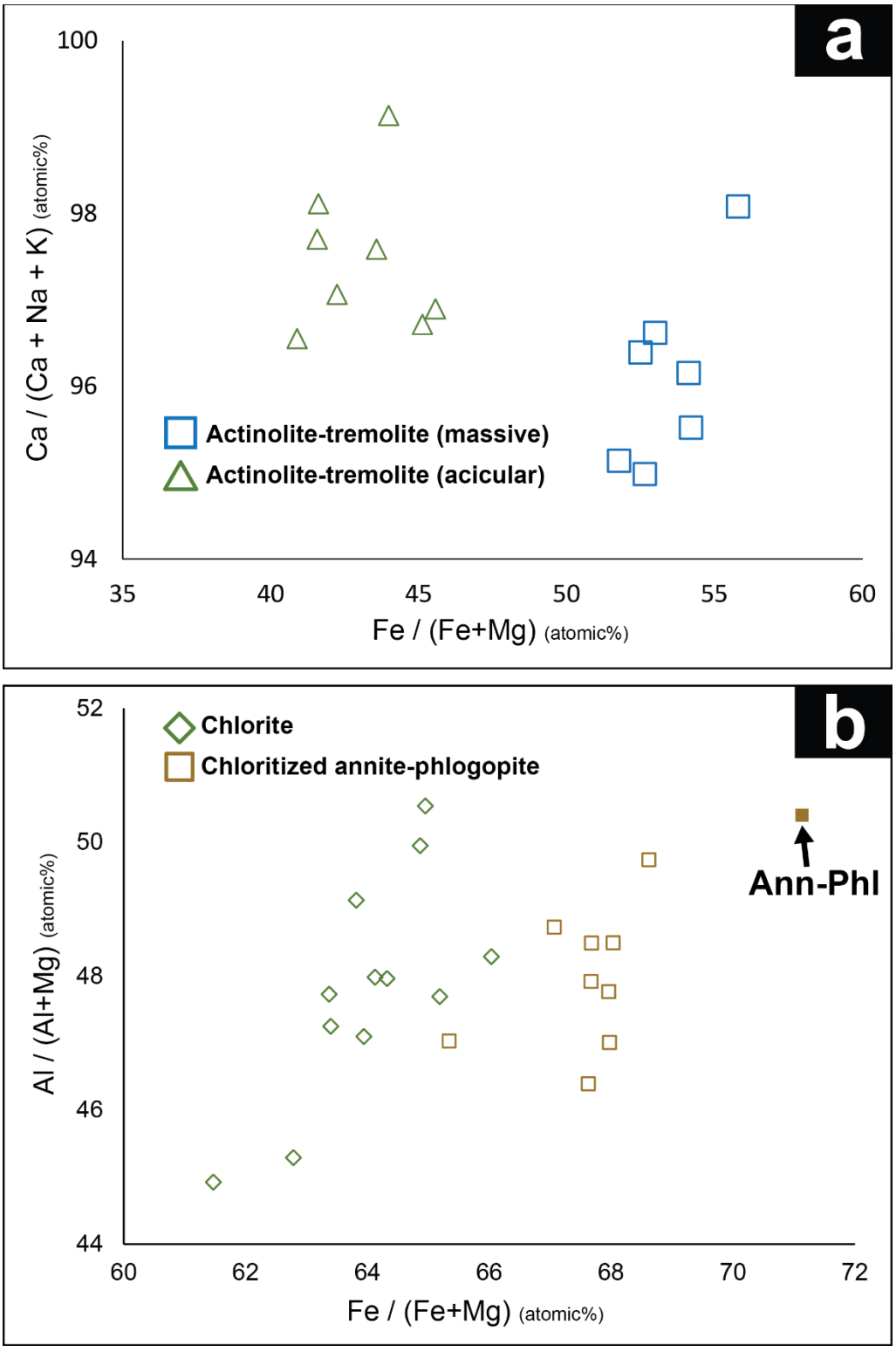

Figure 15. Semi-quantitative SEM-EDS mineral analyses (atomic %) from North Range footwall rocks. **(a)** Plot showing difference in chemistry of coexisting massive and acicular-textured actinolite-

tremolite**. (b)** Plot showing change in annite-phlogopite (Ann-Phl) chemistry along a long traverse as it is replaced by chlorite.

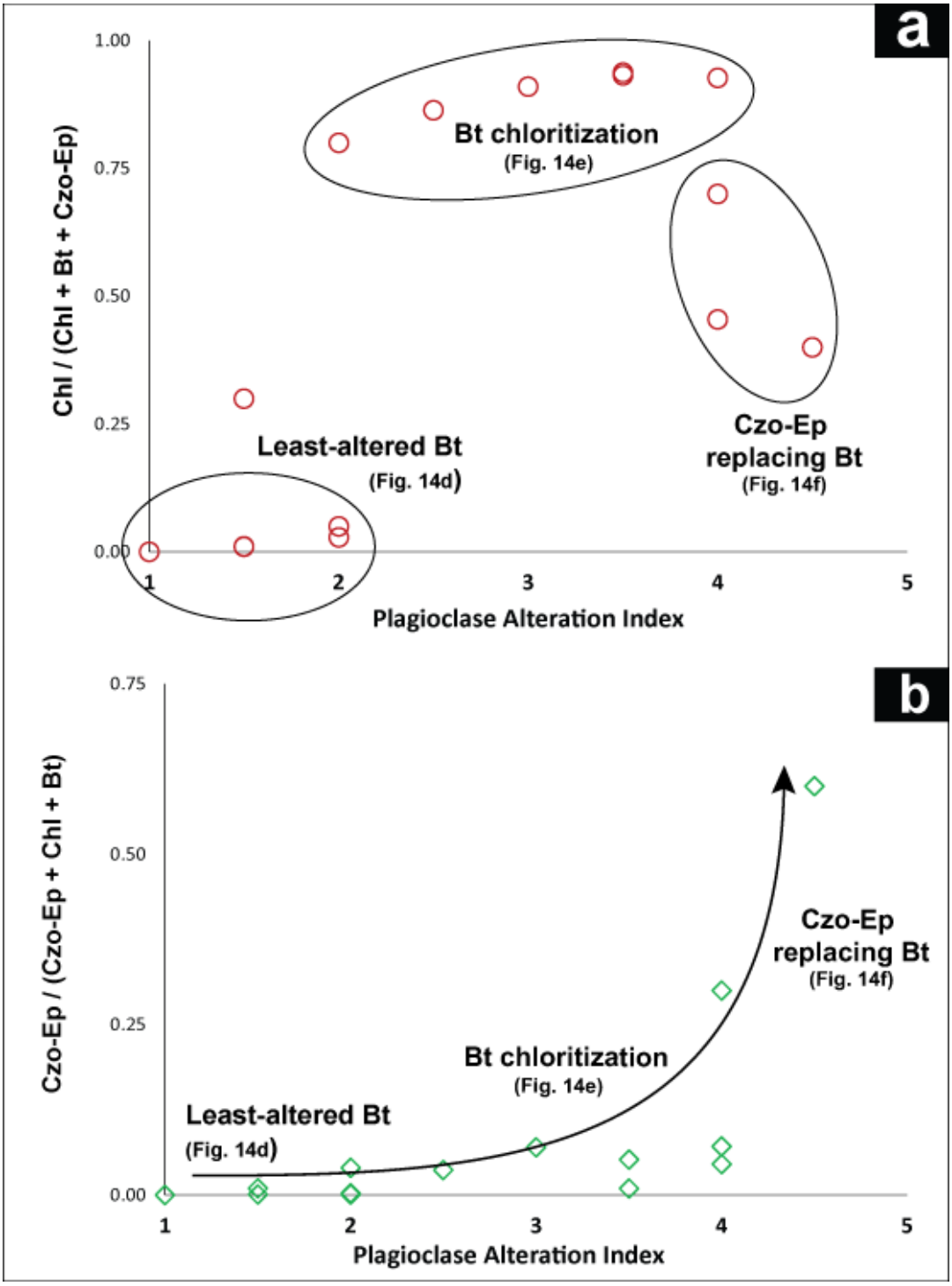

Figure 16. (a, b) Plots of the plagioclase alteration index (development of secondary features – *e.g.* porosity, fine-grained clinozoisite-epidote) versus degree of biotite replacement by chlorite + clinozoisite-epidote. Abbreviations: Bt – biotite-group mineral; Chl – chlorite-group mineral; Czo-Ep – clinozoisite-epidote.

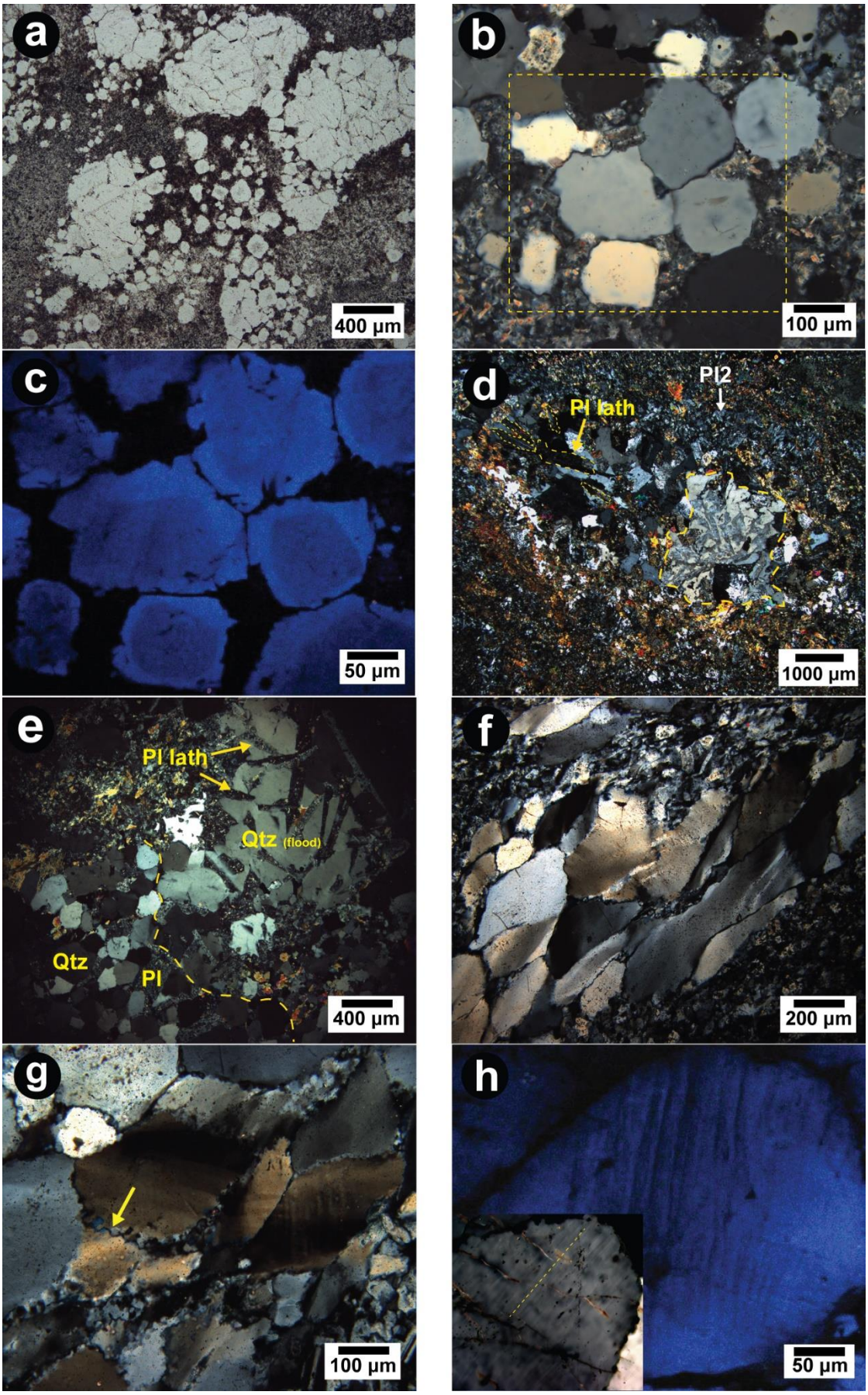
a
400 µm
b
100 µm
c
50 µm
d
Pl2
Pl lath
1000 µm
e
Pl lath
Qtz (flood)
Qtz
Pl
400 µm
f
200 µm
g
100 µm
h
50 µm

Figure 17. Examples in plane-polarized light (a), cross-polarized light (b, d, e, f, g,), and cathodoluminescence (c, h) of quartz (Qtz) textures from Victor footwall rocks. **(a)** Fine-grained, equant Qtz adjacent granoblastic polygonal Qtz aggregates. **(b, c)** Equant to sub-equant quartz with interstitial plagioclase (Pl). Yellow dotted box is area from (c). **(d)** Intergrowths of Qtz + K-feldspar (inside yellow dashed line) and Qtz + lath Pl. **(e)** Euhedral Pl lath chadacrysts with oikocrystic 'flood' Qtz (upper right), grading into subhedral Qtz with interstitial Pl (lower left). **(f)** Deformed and flattened Qtz grains, parallel to ribbons of extinction oriented NE-SW. **(g)** Deformation bands and new bulges/subgrains (yellow arrow) overprinting granoblastic Qtz, producing a core-and-mantle structure. **(h)** Possible deformation bands in a Qtz grain. Inset image (cross-polarized light, rotated ~40º clockwise) shows lamellae oriented NE-SW.

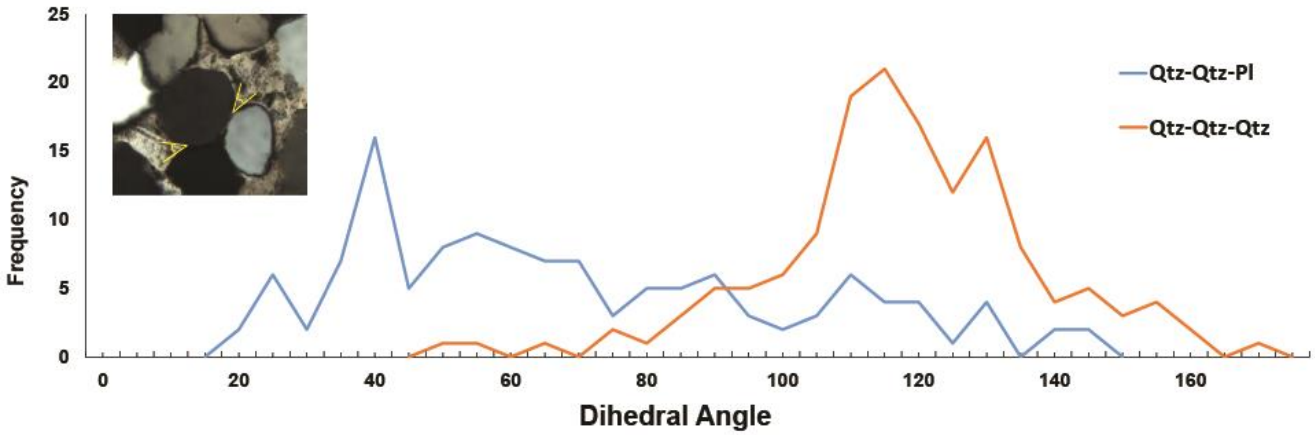

Figure 18. Frequency diagram of quartz-quartz-plagioclase dihedral angles (see inset image) compared with quartz dihedral angles from coexisting granoblastic polygonal quartz aggregates (see Fig. 17a for an example).

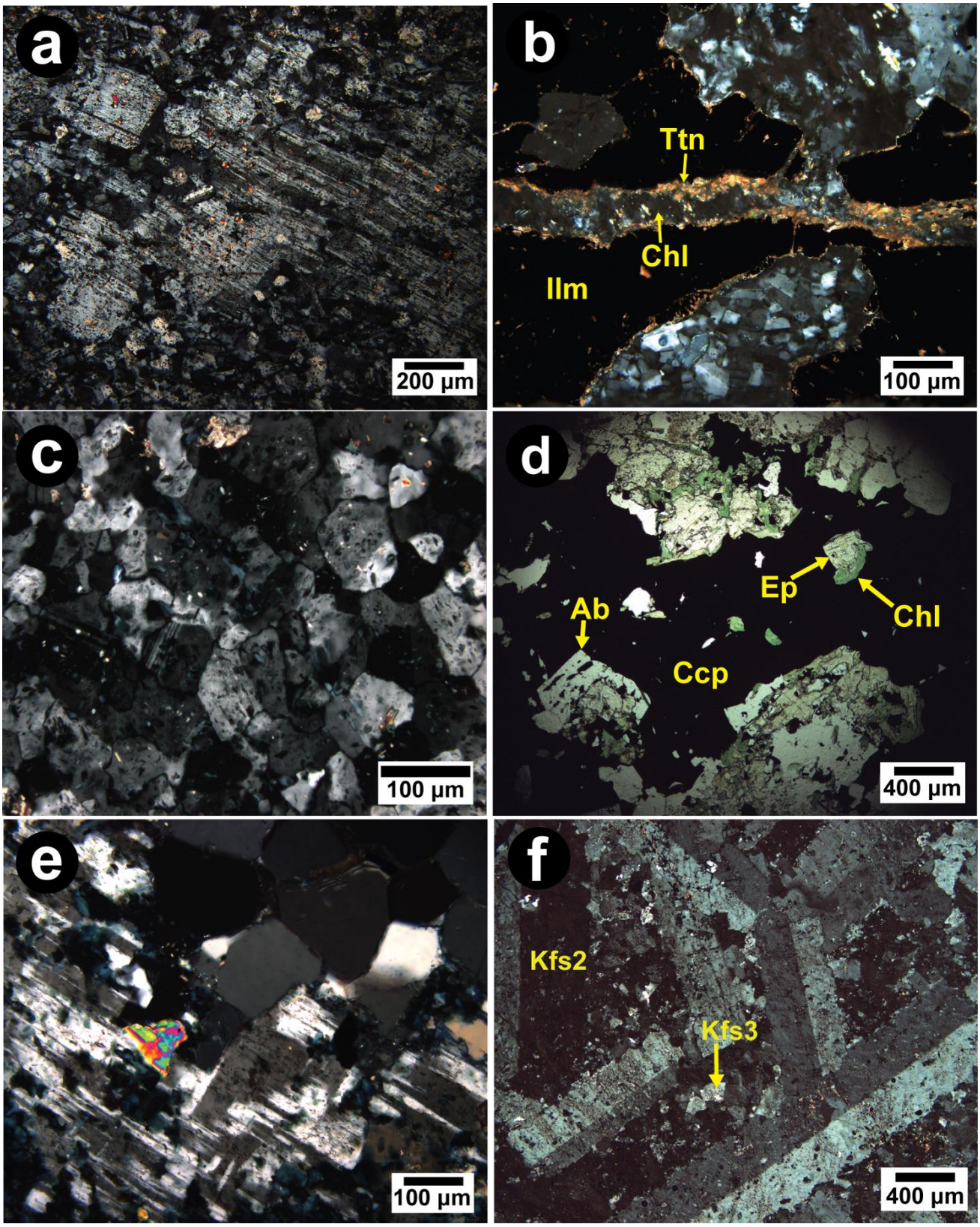
a
200 µm
b
Ttn
Chl
Ilm
100 µm
c
100 µm
d
Ab
Ep
Chl
Ccp
400 µm
e
100 µm
f
Kfs2
Kfs3
400 µm

Figure 19. Examples in cross-polarized light (a, b, c, e, f), and plane-polarized light (d) of plagioclase (Pl) and K-feldspar (Kfs) textures from Victor footwall rocks. **(a)** Remnant Pl1 with deformed polysynthetic twins, replaced by fine-grained Pl2 neoblasts. **(b)** Mosaic of fine-grained Pl2 neoblasts that mimic contour of original Pl1 grain. **(c)** Close-up of granoblastic Pl2 aggregate. **(d)** Development of euhedral albite and epidote-group minerals along the margins of a chalcopyrite-filled cavity. **(e)** Chessboard-style albite. **(f)** Aggregate of prismatic, Carlsbad-twinned Kfs2 neoblasts. Abbreviations: Ccp – chalcopyrite; Chl – chlorite-group mineral; Ep – epidote-group mineral; Ilm – ilmenite; Ttn - titanite

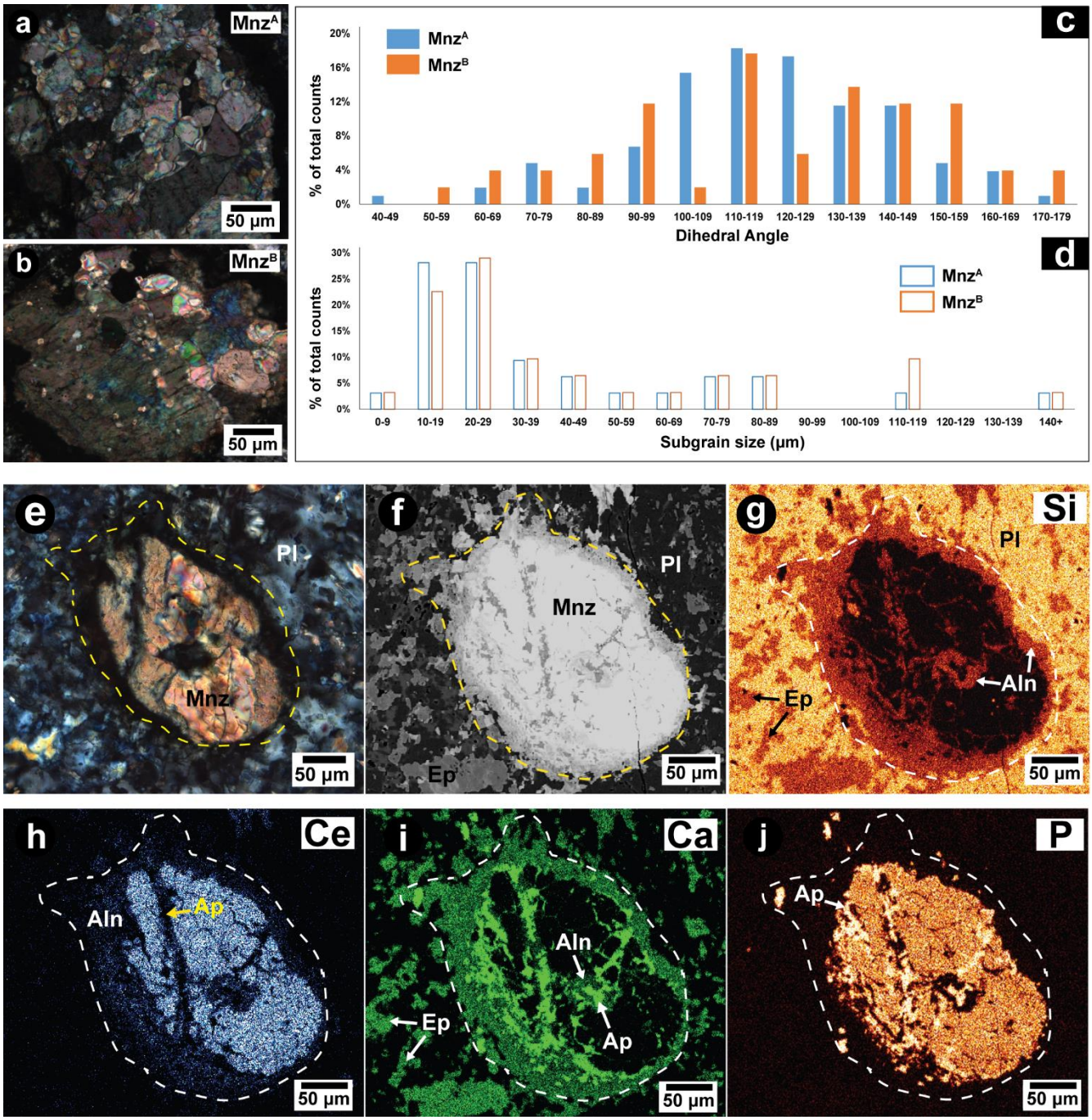

Figure 20. Development of neoblasts and secondary minerals in monazite (Mnz) from Victor footwall rocks. **(a)** MnzA. **(b)** MnzB. **(c)** Frequency diagram of dihedral angles in MnzA and MnzB. **(d)** Frequency diagram of neoblast sizes in MnzA and MnzB. **(e)** Recrystallized Mnz exhibiting neoblast development (XPL). **(f)** BSE image of Mnz grain from (e). **(g, h, i, j)** X-ray maps of Si, Ce, Ca and P

for grain in (e, f). Abbreviations: Aln – allanite; Ap – apatite; Ep – epidote-group mineral; Mnz – monazite; Pl – plagioclase (An_{0-10})

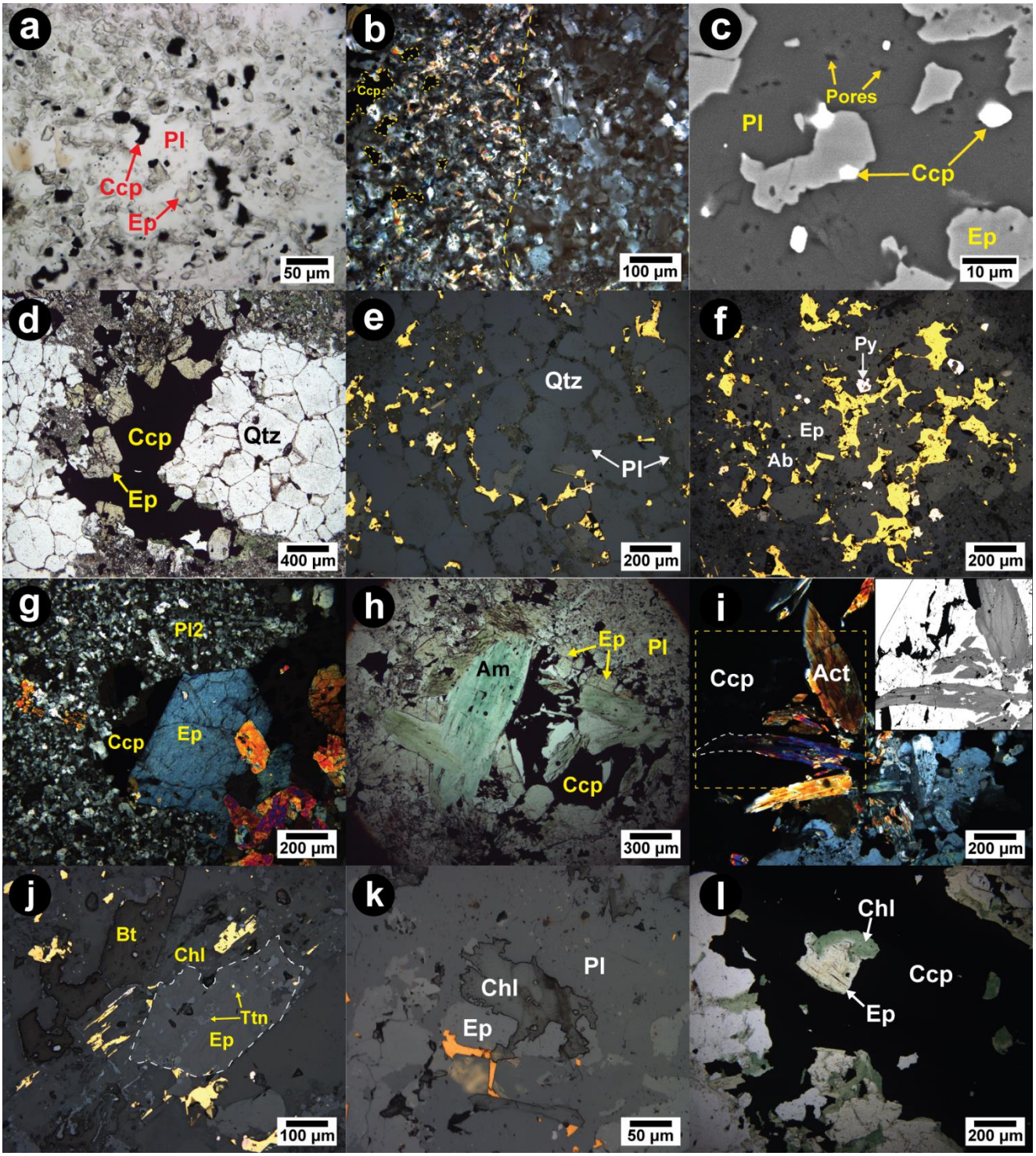

Figure 21. Development of textures in chalcopyrite (Ccp) mineralized samples seen in plane-polarized light (a, d, h, l), cross-polarized light (b, g, i), SEM-BSE mode (c, i), and reflective light (e, f, j, k). **(a, b, c)** Disseminated Ccp and Ep in plagioclase (Pl). Note Ccp abundance coincides with an

increase in density of fine-grained alteration minerals (b). **(d)** Ccp in contact with granoblastic polygonal quartz and Ep. **(e)** Ccp and Pl seams interstitial to sub-equant quartz grains. (f) Ccp interstitial to subhedral Ep and albite. (g, h, i) Euhedral Ep and Act with Ccp filling voids in Pl. Note the comb-textured Act crystal in (i) is extinct where bent (white dashed outline). Also note the zonation due to variations in Fe and Mg (inset image). (j) Ccp and pyrrhotite developed along the (001) of Chl. (k, l) Ep crystals in contact with Ccp, overgrown and/or replaced by anhedral Chl. Abbreviations: Ab – albite; Act – actinolite-tremolite; Am – amphibole; Bt – biotite-group mineral; Chl – chlorite-group mineral; Ep – epidote-group mineral; Ttn – titanite; Py – pyrite; Qtz – quartz.

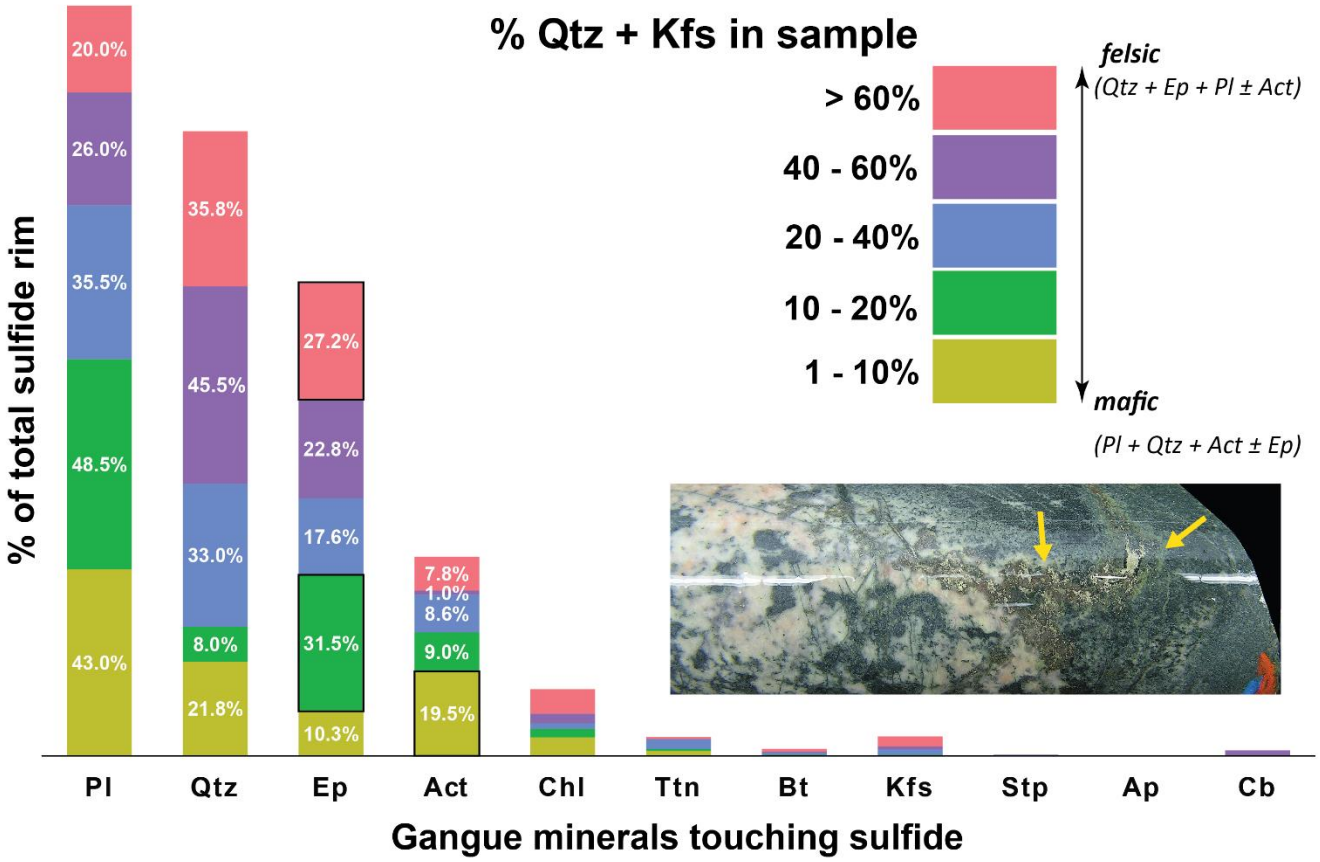

Figure 22. Histogram showing association of chalcopyrite (Ccp) with silicate phases for 5 different bulk rock compositions (*i.e.* felsic to mafic). Note the strong association between Ccp and Pl + Qtz. Abbreviations: Ap – apatite; Act – actinolite-tremolite; Bt – biotite-group mineral; Cb – carbonate-mineral; Chl – chlorite-group mineral; Ep – epidote-group mineral; Kfs – K-feldspar; Ttn – titanite; Py – pyrite; Pl – plagioclase; Qtz – quartz; Stp - stilpnomelane

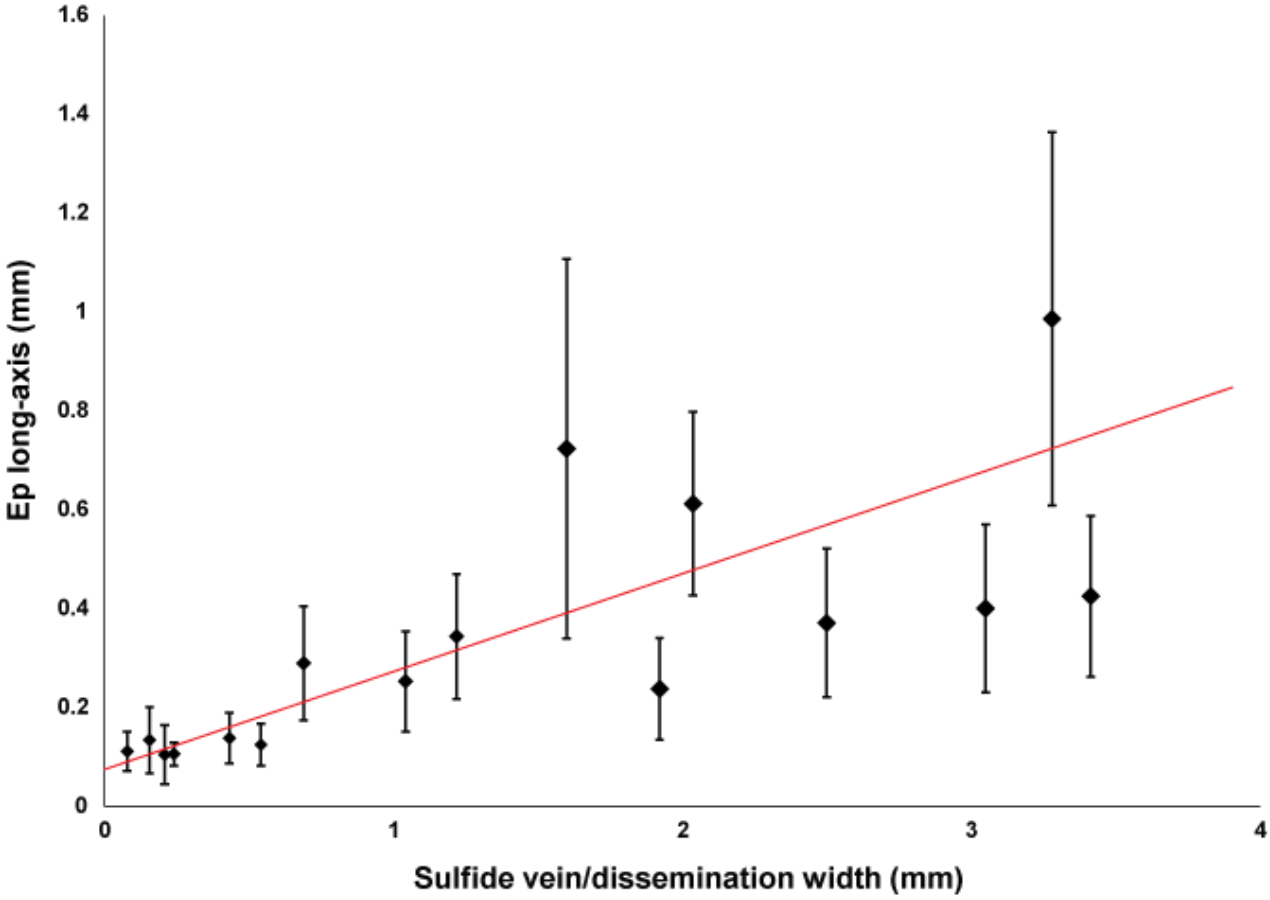

Figure 23. Binary plot showing the relationship between the size of specific chalcopyrite veins and disseminations (taken as its average measured width) and the grain size of clinozoisite-epidote (Ep)

crystals along their margins (see Fig. 20d, g). Note the strong variation in Ep grain sizes (measured along the long-axis) for a given Ccp occurrence.

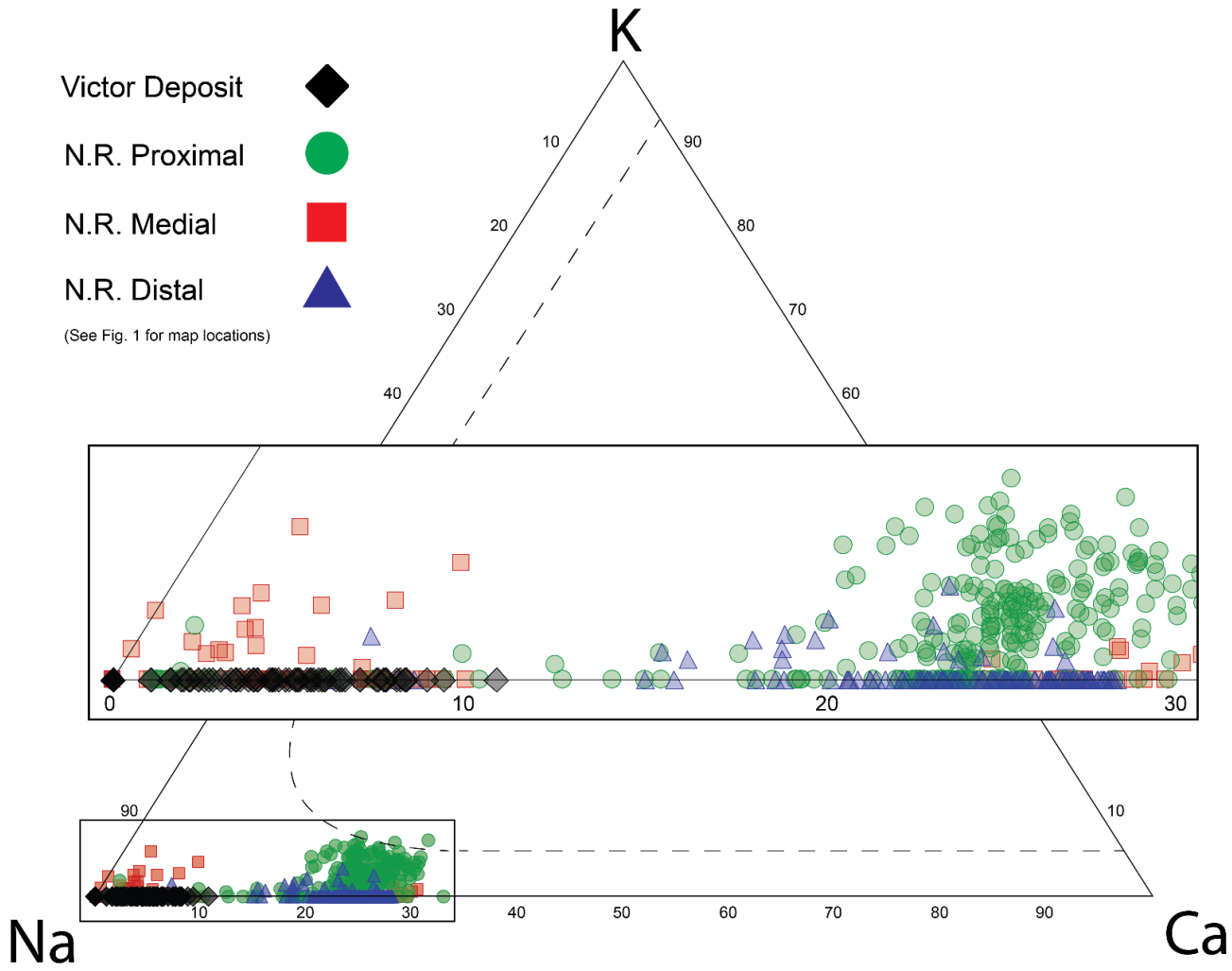

Figure 24. Ternary plagioclase chemistry (semi-quantitative) for samples from the Victor deposit and the North Range (N.R.) transect. See Fig. 1 for map locations.

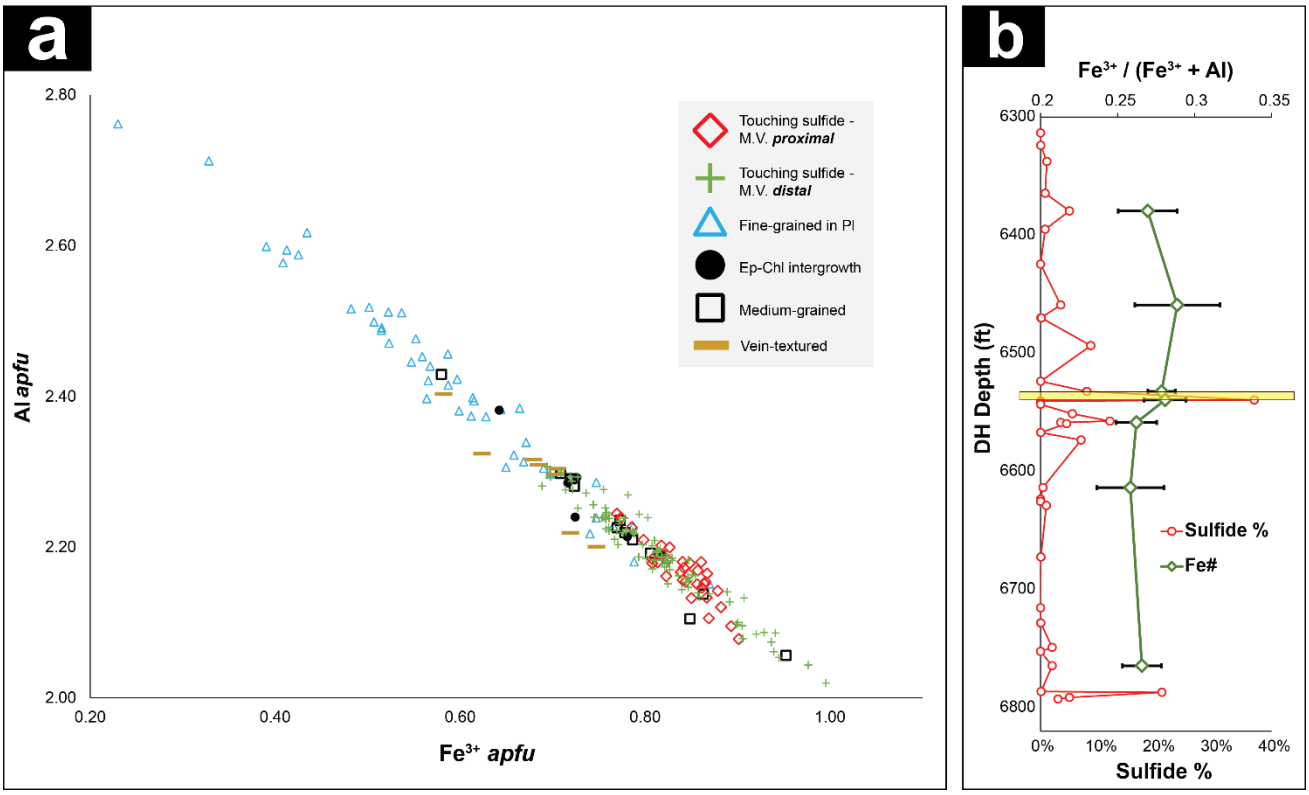

Figure 25. Mineral chemistry for clinozoisite-epidote (Czo-Ep) in samples from the Victor footwall deposit. **(a)** Plot of Fe^{3+} (*apfu*) against Al (*apfu*) for Czo-Ep, which is subdivided into textural populations. Massive vein-style chalcopyrite is referred to as M.V. **(b)** Downhole plot of *Fe#* ($Fe^{3+}/(Fe^{3+} + Al)$) for Czo-Ep that is in contact with chalcopyrite, which is compared with the estimated modal chalcopyrite in the sample. Note that the yellow bar represents the downhole location of a massive chalcopyrite vein (Fig. 2h).

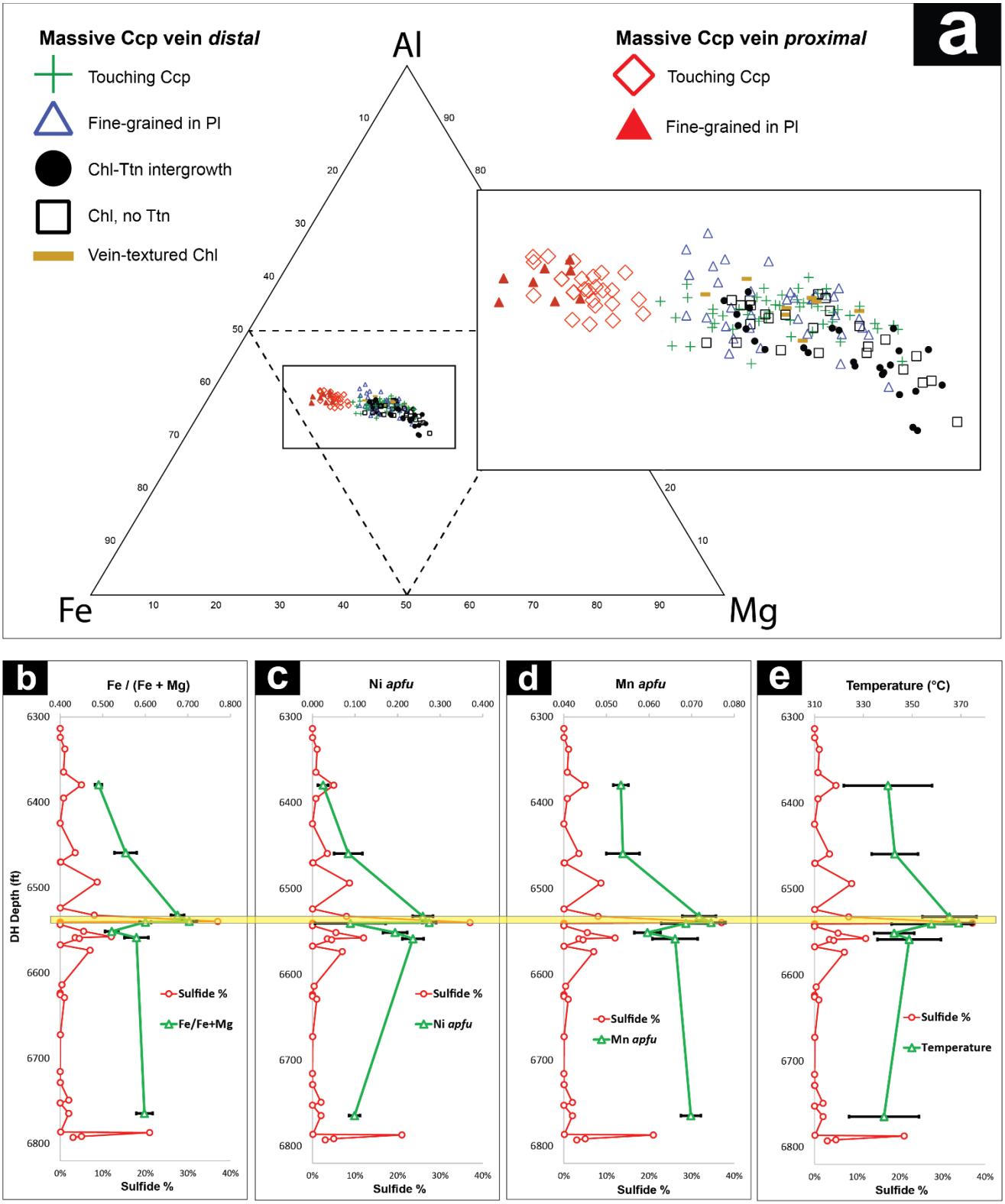

Figure 26. Mineral chemistry for chlorite in samples from the Victor footwall deposit. **(a)** Ternary plot of Al-Fe-Mg for chlorite, which is subdivided based on textural populations. **(b, c, d)** Downhole

plots of *Fe#* (Fe/(Fe + Mg)), Ni (*apfu*), and Mn (*apfu*) for chlorite that is in contact with chalcopyrite, compared with estimated total chalcopyrite in each sample. **(e)** Downhole plot of chlorite crystallization temperature, based on the method developed by Cathelineau (1988). Note that the yellow bar represents the downhole location of a massive chalcopyrite vein (Fig. 2h).